Theses and Dissertations

2013

Characterization of Encapsulated Phase Change Materials for Thermal Energy Storage

Weihuan Zhao
Lehigh University

Follow this and additional works at: http://preserve.lehigh.edu/etd

Recommended Citation

Characterization of Encapsulated Phase Change Materials for Thermal Energy Storage

by

Weihuan Zhao

Presented to the Graduate and Research Committee
of Lehigh University
in Candidacy for the Degree of
Doctor of Philosophy

in

Mechanical Engineering

Lehigh University

(January 2013)

Approved and recommended for acceptance as a dissertation in partial fulfillment of the requirements for the degree of Doctor of Philosophy.

_____

Date

_____
Dr. Alparslan Oztekin, Dissertation Advisor

_____

Accepted Date

Committee Members:

_____
Dr. Sudhakar Neti, Committee Chair

_____
Dr. Wojciech Z. Misiolek, Committee Chair

_____
Dr. Kemal Tuzla, Committee Member

_____
Dr. John C. Chen, Committee Member

Acknowledgments

I would like to express my greatest appreciation to my dissertation advisors, Dr. Alparslan Oztekin and Dr. Sudhakar Neti. They always answered my questions patiently and guided me in the right directions during this research work. I appreciate all the help my Ph.D. committee members, Dr. Kemal Tuzla, Dr. John C. Chen and Dr. Wojciech Z. Misiolek, gave me. I am also grateful for the work done by other graduate students, Ying Zheng, James J. Blaney, Joseph C. Sabol, Ali F. Elmozughi, etc., in the solar energy storage group. In addition, I would like to thank my parents and all my friends who have always been supportive and given me encouragement.

TABLE OF CONTENTS

LIST OF TABLES

LIST OF FIGURES

ABSTRACT

Solar energy is receiving a lot of attentions at present since it is a kind of clean, renewable and sustainable energy. A major limitation however is that it is available for only about 2,000 hours a year in many places. One way to improve this situation is to use thermal energy storage (TES) system for the off hours. A novel method to store solar energy for large scale energy usage is using high melting temperature encapsulated phase change materials (EPCMs). The present work is a study of thermal energy storage systems with phase change materials (PCMs). It is hoped that this work is to help understand the storage capability and heat transfer processes in the EPCM capsules in order to help design large EPCM based thermoclines. A calorimeter system was built to test the energy stored in EPCM capsules and examine the storage capabilities and potential for storage deterioration in EPCM capsules to determine the types of EPCMs suitable for TES. To accomplish this, the heat transfer performances of the EPCMs are studied in detail. Factors which could affect the heat transfer performance including the properties of materials, the sizes of capsules, the types of heat transfer fluids, the gravity effect of solid PCM, the buoyancy-driven convection in the molten PCM, void space inside the capsule are given attention. Understanding these characteristics for heat transfer process could help build the EPCM based thermoclines to make energy storage economical for solar energy and other applications.

CHAPTER 1
INTRODUCTION

1.1 Motivation

Solar energy is one of the most attractive energy sources in the world. As a kind of clean, renewable energy, it is receiving a lot of attention due to the finite nature of fossil fuels and the pollution they cause. There are two popular approaches to use solar energy for electricity generation. One is direct conversion of solar radiation into electric energy using photovoltaic cells (PV cells); the other is conversion of solar radiation into thermal energy for electric power generation in concentrating solar power (CSP) plants. The latter approach lends itself to large-scale applications eventually at competitive costs.

However, there is limitation for solar energy usage; it is restricted by the availability of solar radiation. Even in locations with favorable solar incidence, the diurnal solar radiation provides only 6-8 hours of high radiant incidence per day. Thus, the solar power plants could suffer low capacity factors. Therefore, solar energy is not widely used for electricity generation at present. According to U.S. Energy Information Administration 2012 annual energy outlook, the supplies for U.S. electricity generation were 70% fossil fuels, 20% nuclear, and only 10% renewable energy in 2010 [1]. Nevertheless, because of the severe pollution problems on earth, electricity mix will gradually shift to lower-carbon options, which is expected to be led by the exponentially growth of renewable energy including solar energy in the future [1].

One way to improve upon the shortage of solar energy usage is to use thermal energy storage (TES). TES system can store part of the solar energy captured during times of high incidence of solar radiation to use for power generation during cloudy or night periods, and help manage the matching of load-generation patterns to improve the plant overall capacity factor.

1.2 Background and Survey of Literature

Thermal energy storage can be classified on the basis of storage mechanism: sensible heat storage, latent heat storage, and thermo-chemical heat storage. For sensible heat storage, the heat storage capacity depends on the mass of the media, its heat capacity and the temperature rise. Therefore, sensible heat storage can only store relatively small quantities of thermal energy with larger volume requirements of materials and larger temperature difference of heat transfer fluid (HTF) between storing and retrieval energy process. Compared to sensible heat storage, latent heat storage and thermo-chemical heat storage can store larger quantities of thermal energy with smaller temperature difference.

For the thermo-chemical heat storage, a reversible gas-solid chemical reaction under the addition of heat is potential to store thermal energy. An ideal reaction scheme is that a solid compound is charged with heat and dissociates to two components, a solid component and a gaseous component, for heating process. And the stored heat can be released when the two components are brought together to react back to one solid compound during discharging process. In order to obtain a high energy density, condenser is needed to condense the gaseous component to reduce the volume of the product in the reaction, which makes the storage system much more complex. Therefore,

although thermo-chemical heat storage can store high quantities of thermal energy, it still has a lot of uncertainties in its application. Its development is still at an early stage.

The latent heat storage can store the latent heat in a constant phase transition temperature besides the sensible heat in two phases. The latent heat storage has a higher storage density compared to the sensible heat storage. Therefore, latent heat storage can greatly minimize the volume of the materials and thus reduce the size of the storage system. Moreover, the temperature change of the system can be smaller for the same energy requirement, which may greatly increase thermal efficiency of the overall system.

Thermal energy storage systems usually use one tank or two tank systems for heat storage in CSP plants [2]. A two-tank system uses one tank for high temperature heat transfer fluid directly from the solar receiver and the other tank for low temperature heat transfer fluid from the steam generator [2]. One-tank thermocline based systems eliminates the second tank and reduces the volume of the system. However, it is more difficult to separate low temperature HTF from high temperature HTF in one-tank system and thus more difficult to operate. Cascaded latent heat storage has also been proposed for TES in CSP plant [3]. Several PCMs with different melting points are to be used in the thermocline. The PCM with the material of highest melting point is located at the top of the storage system and material of lowest melting point at the bottom of the storage system. With variable HTF temperature in the thermocline, such a thermocline could meet the melting points of the different levels of PCMs. Additionally, such a thermocline

with several PCMs (or an infinite number of PCMs) could lend itself to near isothermal heat transfer enabling a high exergy system.

Storage of thermal energy using latent heat is potentially an attractive method to store solar thermal energy since it could enable near isothermal and high exergy storage conditions. Thus, the current work focus is on the latent heat storage using phase change materials (PCMs) for large scale generation of electrical power.

Numerous phase change materials, which can be used for low temperature (below 120 $^{\circ}$C) thermal energy storage, such as for space heating, etc., have been studied in the past decades. They can be categorized into two classes: organic and inorganic salt hydrates [4-13].

Organic phase change materials have poorer heat transfer properties, such as lower density, and are more expensive than inorganic salts in general. However, organic materials usually do not suffer segregation and subcooling problems during thermal cycling, which can be a severe problem for some salt hydrates. Organic materials include paraffin waxes, fatty acids, and sugar alcohols [7]. They have been used in many developmental studies recently. Paraffin waxes have been commercially used for active forced hot-air systems [12].

Salt hydrate phase change materials that have been studied include $CaCl_2 \cdot 6H_2O$, $MgCl_2 \cdot 6H_2O$, $Na_2SO_4 \cdot 10H_2O$, etc. They offer a range of operating temperatures, melting

points ranging from 7 to 117 °C [12]. Salt hydrates have high latent heats of fusion; better heat transfer properties compared to organic materials, and are relatively cheap. However, some of them suffer from segregation and sub-cooling problems.

Many salt hydrates do not solidify right away when the temperature of the materials is at or below the melting temperature. This phenomenon is called subcooling. During subcooling, the phase change materials are in a metastable state, which implies not being in thermodynamic equilibrium. To reduce or suppress subcooling, nucleating agents are added to the phase change materials [7].

The effects of segregation, also called semi-congruent or incongruent melting, are a potential problem with phase change materials consisting of multiple components [7]. A typical example is salt hydrate consisting of two components, salt and water. During the melting process, some salt hydrates undergo a peritectic reaction generating two phases, aqueous salt solution and a solid lower hydrate or a solid anhydrous salt. Thus, segregation occurs because solid hydrates or anhydrous salts are denser than liquids, which leads to the lower hydrate difficult to recombine with water in the solidification process. It thus can result in irreversible processes thus reducing the latent heat storage capability of PCMs. To overcome the segregation problem, gelling additive are used with the phase change material [7]. Additionally, encapsulation methods can also be used to reduce such separation problems. More studies are needed on these stability problems for salt hydrate PCMs.

While low temperature phase change materials have been widely studied extensively, there is a significant need for high temperature phase change materials, whose melting points are above 200 $^{\circ}$C, for large scale thermal energy storage for electricity generation (100 MW$_e$ plants for 6 to 24 hours). High temperature PCMs will enable the generation of high enthalpy steam for better Rankine cycle performance. A few research groups are studying the viability of PCMs for thermal energy storage [2,3,14,15]. Current work concentrates on high temperature phase change materials for thermal energy storage (TES).

Table 1.1 Phase change materials with melting points from 300 $^{\circ}$C to 800 $^{\circ}$C [14-23].

Phase Change Materials Composition (mole%)	Melting Points ($^{\circ}$C)	Heat of Fusion (kJ/kg)
NaNO$_3$	308	173
KNO$_3$	337	100
Zinc	420	113
NaCl/MgCl$_2$ (57/43)	444 [*]	292 [*]
NaCl/CaCl$_2$ (48/52)	500	278
CaCl$_2$/NaCl (52.1/47.9)	504	278
BaCl$_2$/MgCl$_2$ (42.9/57.1)	559	---
BaCl$_2$/CaCl$_2$ (35.9/64.1)	608	---
CaCl$_2$/MgCl$_2$ (47.4/52.6)	617	---
BaCl$_2$/NaCl (39.9/60.1)	651	---
Aluminum	660	397.3
NaCl/KCl (50/50)	685	---
NaF/KF (40/60)	710	403.3
MgCl$_2$	714	454
KCl	770	356.3
CaCl$_2$	782	255.7
NaCl	800	430 [*]

[*] Measured or calibrated in Lehigh University

There are many potential high melting temperature PCMs which can be used for TES. Table 1.1 shows different types of PCMs with melting points from 300 $^{\circ}$C to 800 $^{\circ}$C. They have relatively large latent heat of fusion and thus can store huge amount of solar energy for a given mass of storage material. Nevertheless, some salt PCMs can be

corrosive or have other problems during heating/cooling thermal cycles. Therefore, detailed studies are required for these materials before they can be useful to industry.

1.3 Encapsulated Phase Change Materials

Encapsulated phase change materials (EPCMs) are of interest since encapsulating can increase the heat transfer surfaces, avoiding the large thermal resistances related to heat conduction in PCM for tank storage systems. Thus, encapsulating can help to shorten the heat transfer times for PCM [24,25], especially for those materials with low thermal conductivities. Furthermore, some phase change materials, such as salt hydrates or some eutectic salts, suffer sub-cooling and segregation problems during thermal cycling [7,26]. And encapsulation could help to mitigate such problems. Moreover, encapsulation can also protect the PCM from exposure and potential corrosion with heat transfer fluid. Nevertheless, encapsulation materials can raise other problems, such as compatibility with encapsulation material, machinability for encapsulating materials, etc.

Besides, encapsulation should stand the stresses in the material and allow for volume change of the PCM during melting-solidification cycling. Stress analysis for various EPCM shapes has been conducted by James J. Blaney [27,28], a master student graduated from Mechanical Engineering Department in Lehigh University, for the EPCM capsules as it was experiencing the volume change due to phase change and thermal expansion. Blaney et al. concluded that it is essential to leave sufficient void in the EPCM to minimize the pressure inside and to maintain structural integrity of the EPCM. These

studies also showed that encapsulation material has to be sufficiently thick to prevent the deformation of the capsule caused by the stress exerted on the shell.

Using encapsulated phase change materials to store solar energy at high temperatures (above 300 $^{\circ}$C) is expected to be a novel thermal storage technology for solar power generation. There have been numerous reports documenting modeling of solidification or melting process of single and multi-component materials [29-36]. Li et al. [29,30] used front-tracking method to solve the solidification problem; Davis, S.H. [31], Coriell et al., 1985 [32] studied the solidification process in a binary liquid; Glicksman et al. [33], Coriell et al., 1984 [34], Murray et al. [35], Fang et al. [36] considered the convection at crystal-melt interfaces. Nevertheless, not too many of these have studied high temperature encapsulated phase change materials. Thus the focus of present work dealing with the modeling as well as the experiments of high temperature EPCMs is expected to be timely.

1.4 Objectives

The present work focuses on high melting temperature encapsulated phase change materials for TES for CSP plants. As part of this effort, a unique calorimeter system was built in Lehigh University in order to determine the enthalpy changes and enthalpy of fusion for phase change materials over the temperature range of interest. The calorimeter system was also used to test whether or not there is deterioration of storage capability of EPCMs after multiple thermal cycles or after long-term exposure at high temperatures

(above the melting points of PCMs) to determine the types of EPCMs suitable for thermal energy storage.

Fundamental heat transfer analysis was also conducted to investigate high temperature energy storage using EPCMs in order to help the design of EPCM based thermoclines. One-dimensional as well as two-dimensional heat transfer analysis was studied for EPCM capsule model. Numerical computer codes developed as part of this work were used to analyze the heat transfer performance of EPCM considering various factors, including the gravity effect of solid PCM, the buoyancy-driven convection in molten PCM and the volume expansion during phase change. All these factors will be discussed in detail in the following chapters.

Several kinds of PCMs were considered for the experiments and simulations, including metal like zinc and aluminum; salts like $NaNO_3$, $NaCl$-$MgCl_2$ eutectic (57% mole fraction $NaCl$ and 43% mole fraction $MgCl_2$), $MgCl_2$, and $NaCl$. Stainless steel or carbon steel was selected as the encapsulation shell with around 1.5875 mm (1/16 inch) thickness. After considering various shapes and machinability by the students from Material Science & Engineering Department in Lehigh University, cylindrical shaped EPCM capsules were proposed to be used for TES.

CHAPTER 2
EPCMs FOR TES – CHARACTERIZATION BY CALORIMETRY

2.1 Motivation

In order to examine the storage capabilities of EPCM capsules, an immersion calorimeter system was built to determine the enthalpy changes and enthalpy of fusion for phase change materials over the temperature range of interest. Calorimetry was also used to examine whether or not the high melting temperature PCMs behaved as desired, storing thermal energy in a thermal cycle with complete phase change and no energy losses with repeated thermal cycles. The calorimeter system was used to investigate any potential deterioration in storage capacity of EPCMs over multiple thermal cycles, and test the storage performances of EPCMs after long-term (hundreds of hours) exposure to high temperatures environments.

2.2 Calorimeter Design and Operation

The calorimeter was initially designed, fabricated and tested by another doctoral research assistant in Lehigh's Department of Chemical Engineering, Ms. Ying Zheng. During the current work, various modifications in the hardware and operational procedure were incorporated to improve performance.

The primary component of the calorimeter system is an insulated stainless steel vessel containing a known amount of silicone oil fluid, as shown in Figure 2.1, from the paper by Zheng et al [37]. The selected silicone oil (Dynalene 600) has a high flash point (315 $^\circ$C in open atmosphere) and low vapor pressure, which could help to avoid bubble

nucleation and evaporation when contacted by high temperature EPCM samples. In order to handle the sizes of the EPCM samples used in the present work, approximately 4.5 kg of the silicone oil is required. This amount of silicone oil fluid is selected to optimize accuracy of experimental measurements. A larger mass of silicone oil would reduce temperature rise of the calorimeter when heated sample is immersed into the calorimeter system, which would make the accuracy of temperature measurement worse. Smaller mass of silicone oil would increase the effect of heat loss to ambient air. Either of these could have reduced accuracy of the calorimeter measurements.

The vessel containing silicone oil is made of thin stainless steel insulated with an external layer of polymer foam. Two concentric guard cylinders are placed outside the vessel to further reduce the heat losses to the surroundings as well as minimize the temperature measurement noise of the two thermistors during the experiment. Moreover, since thermal conductivity of silicone oil is relatively low, an electric power mixer is used for stirring the fluid in the vessel to achieve uniform temperature in the calorimeter system during experiment. A stainless steel wire is welded on the top of the test sample to suspend the EPCM capsule in the silicone oil during tests. Thermistors in the silicone oil fluid and between the vessel and external guard cylinders accurately monitor calorimeter system and ambient air temperatures, respectively, as sketched in Figure 2.1. All measurements are recorded as functions of time by a data acquisition system (DAS) into a computer.
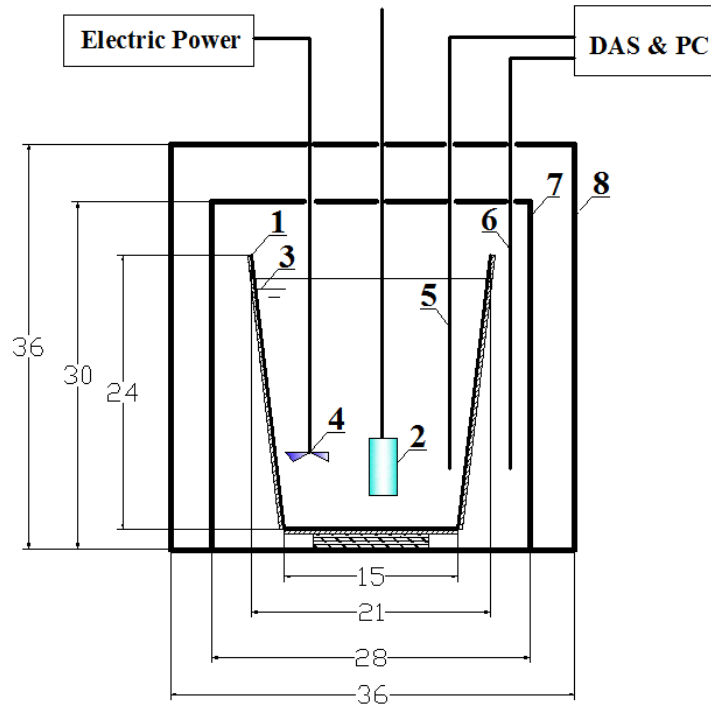
All units are in centimeter.

1- Stainless steel container with foam insulation   5- Thermistor in calorimeter
2- EPCM sample   6- Thermistor for ambient air
3- Silicone oil (fluid)   7- Guard cylinder #1
4- Stirrer   8- Guard cylinder #2

Figure 2.1. Schematic of calorimeter [37]

In each experiment, the test encapsulated phase change material sample would be thermally charged by heating to a selected high temperature in an external furnace. To achieve a uniform temperature through the sample, it is enclosed in insulation material for medium operation temperature in the furnace (from 200 $^{\circ}$C to 550 $^{\circ}$C), or put in a metal chamber for high operation temperature in the furnace (above 550 $^{\circ}$C). Three thermocouples are placed around the circumference of the sample to measure its temperatures, and an average reading of the three thermocouples is taken to represent the temperature of sample. Meanwhile, the calorimeter (vessel, stirrer, silicone oil fluid, and guard cylinders) would be maintained at the laboratory room temperature. When steady state conditions are achieved for both the calorimeter and test sample, the sample would

be thermally discharged by rapid immersion in the silicone oil fluid in the calorimeter. Temperature of the fluid is recorded as heat transfer occurred between the sample and the calorimeter, providing the data needed to determine energy stored in the sample through the discharging process in the calorimeter.
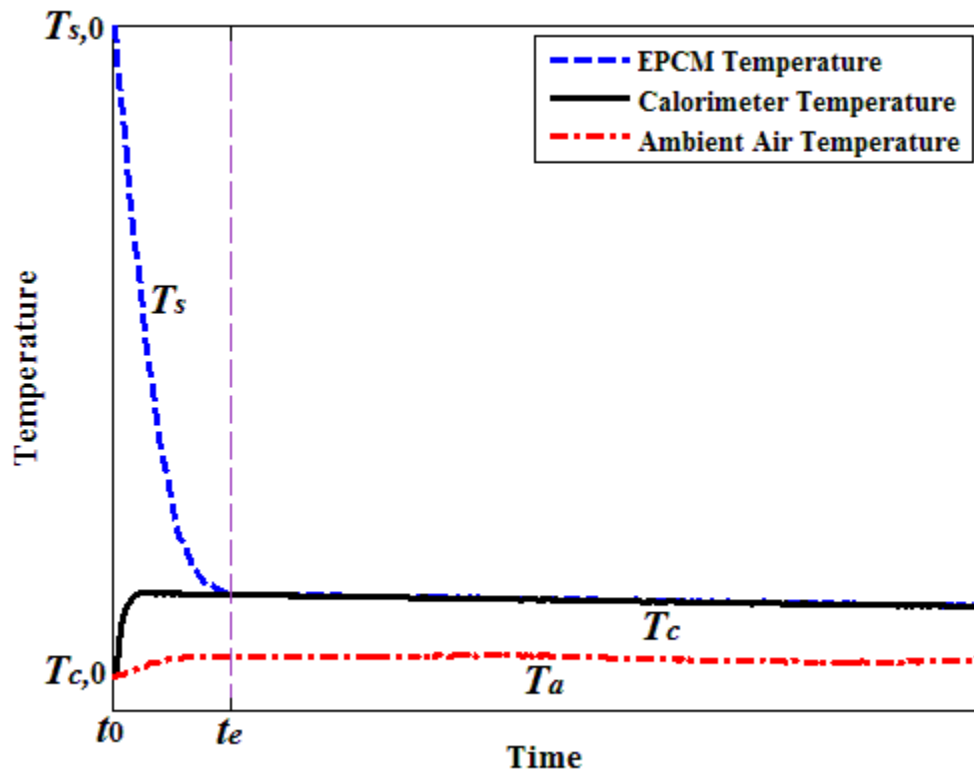
Figure 2.2. Example of temperature transients in calorimetric experiments [37]

Figure 2.2 shows a typical record of the transient energy transfer process between sample and calorimeter, where

T_s = sample temperature

T_c = temperature of the oil-filled calorimeter

T_a = outside air temperature between vessel and guard cylinders

At time t_0, the preheated sample is rapidly immersed into the silicone oil fluid and starts to cool, transferring its thermal energy to the calorimeter system. As the sample

14

temperature, T_s, decreases, the calorimeter temperature, T_c, rises, until the two temperatures equilibrate at time t_e. This equilibration time, t_e, varies significantly with thermal diffusivity of the PCM and capsule size. For each capsule sample, the magnitude of t_e was obtained by numerical analyses of the transient heat transfer process within the capsule, including effect of phase change. In the experiments, analysis is taken for the data at times greater than t_e to avoid errors from non-equilibration. At times greater than t_e, the combined temperature of sample and fluid declines slowly because of the heat loss from the calorimeter to its surroundings. The calorimeter temperatures recorded after the equilibration time provides the information to calculate the total energy transferred to the calorimeter system from the preheated sample. Therefore, it is possible to determine the thermal energy stored in the sample, Q_{EPCM_Exp}, at preheat temperature $T_{s,0}$. The following equations are used to calculate the energy stored in the EPCM capsule.

$$Q_{EPCM\_Exp} = Q_c - Q_{loss} \tag{2.1}$$

$$Q_c = m_c c_{p,c}(T_c - T_{c,0}) \tag{2.2}$$

$$Q_{net} = \left[\Sigma_{Calo.+EPCM} \, mc_p \frac{dT_c}{dt} \right]_{[after \, t_e]} = -hA(T_c - T_a) + \dot{Q}_{mixer} \tag{2.3}$$

$$Q_{loss} = \int_{t_0}^{t} Q_{net} dt = \int_{t_0}^{t} \left[-hA(T_c - T_a) + \dot{Q}_{mixer} \right] dt \tag{2.4}$$

$$Q_{EPCM\_Theo} = Q_{cap} + Q_{PCM} \tag{2.5}$$

$$Q_{cap} = m_{cap} \int_{T_c}^{T_{s,0}} c_{p,cap} \, dT \tag{2.6}$$

$$Q_{PCM} = m_{PCM} c_{p,PCM}^l (T_{s,0} - T_m) + m_{PCM} L + m_{PCM} c_{p,PCM}^s (T_m - T_c) \tag{2.7}$$

In order to use equations (2.1)-(2.7), it is necessary to know values for the net heat loss to surroundings, Q_{loss}, and the effective heat capacity of the calorimeter (including vessel, silicone oil fluid, etc.), $c_{p,c}$.

The net heat loss from calorimeter to surroundings, Q_{loss}, has to be determined individually for each test, since its value varied with operating temperature, ambient air conditions, and power input to stirrer. In a given experiment, the transient temperatures are recorded as illustrated in Figure 2.2. After equilibration of sample temperature and calorimeter temperature (after time t_e), the calorimeter temperature slowly decreases because of the net heat loss to the surroundings. The heat loss rate, measured from the transient temperature data after time t_e, provides the information needed to determine the two coefficients hA and $\dot{Q}_{mixer}$ in equation (2.3). Knowing these coefficients, cumulative heat loss from the calorimeter, Q_{loss}, could be calculated by integrating $\dot{Q}_{net}$ from initial immersion time of the sample to any subsequent time t, as indicated by equation (2.4).

Calibration for the heat capacity of the calorimeter (including vessel, silicone oil, etc.) was accomplished by using standard samples with known properties. Two such samples were fabricated using solid stainless steel 304, with different masses and dimensions, as listed in Table 2.1. The thermal properties of stainless steel 304, are listed in Table 2.2. Since the heat capacity varies with temperature, the thermal energy stored in a stainless steel sample is obtained by integration the heat capacity over the temperature range.

Table 2.1. Standard samples.

	Material of Sample	Mass of Sample (g)	Size
Stainless Steel Sample A	Stainless Steel 304	834.3	38.1 mm Diameter × 101.6 mm Height
Stainless Steel Sample B	Stainless Steel 304	185.1	25.3 mm Diameter × 46.4 mm Height

Table 2.2. Thermal properties of stainless steel 304 [19].

	Melting Point ($^\circ$C)	Heat Capacity (J/kg K)						
		300 K	400 K	600 K	800 K	1000 K	1200 K	1500 K
Stainless Steel 304	1397	477	515	557	582	611	640	682

By preheating these samples of different masses to various temperatures, it was possible to obtain calibration of the heat capacity of the calorimeter over a range of calorimeter temperatures, as graphed in Figure 2.3. The result is well represented by the following dimensional equation, in the temperature operation range of 25-60 $^\circ$C.

$$c_{p,c} = 2.05 \times T_c + 1.39 \times 10^3 \tag{2.8}$$

where $c_{p,c}$ is the effective heat capacity of calorimeter (vessel, silicone oil fluid, etc.) in J/kg·K and T_c is its temperature in $^\circ$C.
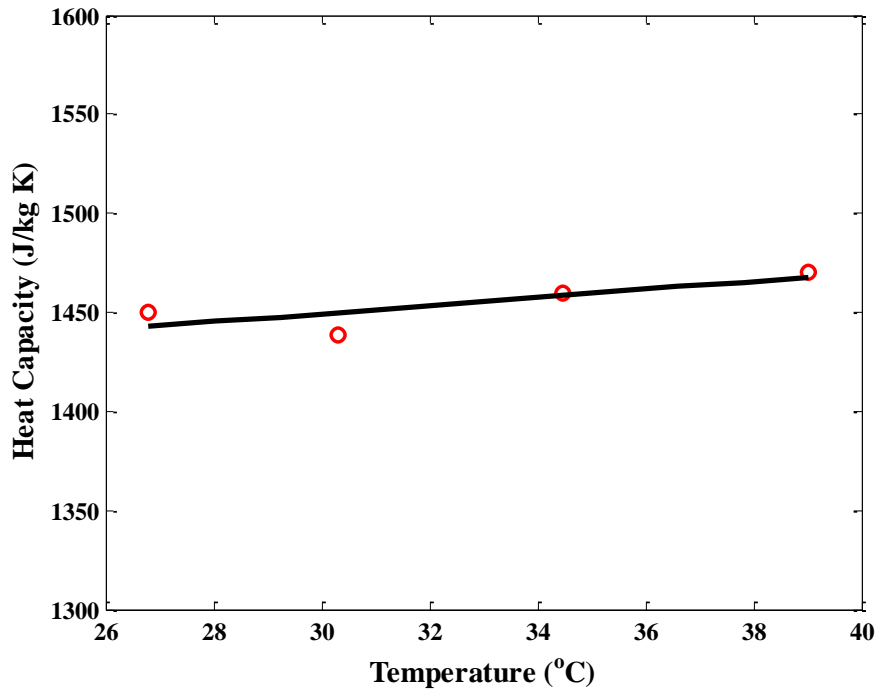
Figure 2.3. Calibrated heat capacity of calorimeter system

After the calibrations for the heat capacities of calorimeter system, $c_{p,c}$, the same procedure was used to obtain experimental measurements of thermal energy storage in the EPCM samples, Q_{EPCM_Exp}, in the following tests.

An analysis of measurement uncertainty in this calorimetric procedure was conducted, indicating a maximum uncertainty of 1.6% in final value of stored energy, Q_{EPCM_Exp}. The following part will discuss about the calibration of the calorimeter system. The calibration will include both measurement uncertainty and operation uncertainty during the experiments.

2.3 Calibration of Calorimeter System

Before testing the encapsulated phase change materials, it is necessary to verify validity of the calorimetric measurements and data analysis by testing standard samples for which energy storage could be calculated directly from their known thermal properties, enabling direct verification of energy balance. Four standard samples were fabricated, two of solid stainless steel and two of encapsulated zinc. The steel samples stored only sensible heat (without phase change), while the zinc samples stored both sensible heat and latent heat of fusion. The published properties of stainless steel are given in Table 2.2 above; properties of zinc are given in Table 2.3.

Table 2.3. Thermal properties of zinc [19-21].

	Melting Point (°C)	Heat Capacity in Solid State (J/kg·K)				Heat Capacity in Liquid State (J/kg·K)	Latent Heat (kJ/kg)
		300 K	400 K	600 K	693 K		
Zinc	420	389	405	441	473	505	113

The sample temperatures were measured by embedded or three externally mounted thermocouples. The thermocouples provided direct measurement of initial sample temperatures at start of immersion into the calorimeter, $T_{s,0}$, for determination of enthalpy change during the tests. Figure 2.4 shows a representative record of such a run [37]. When the heated sample is immersed into calorimeter system, the sample temperature drops quickly while the calorimeter temperature rises rapidly, as represented in Figure 2.4.
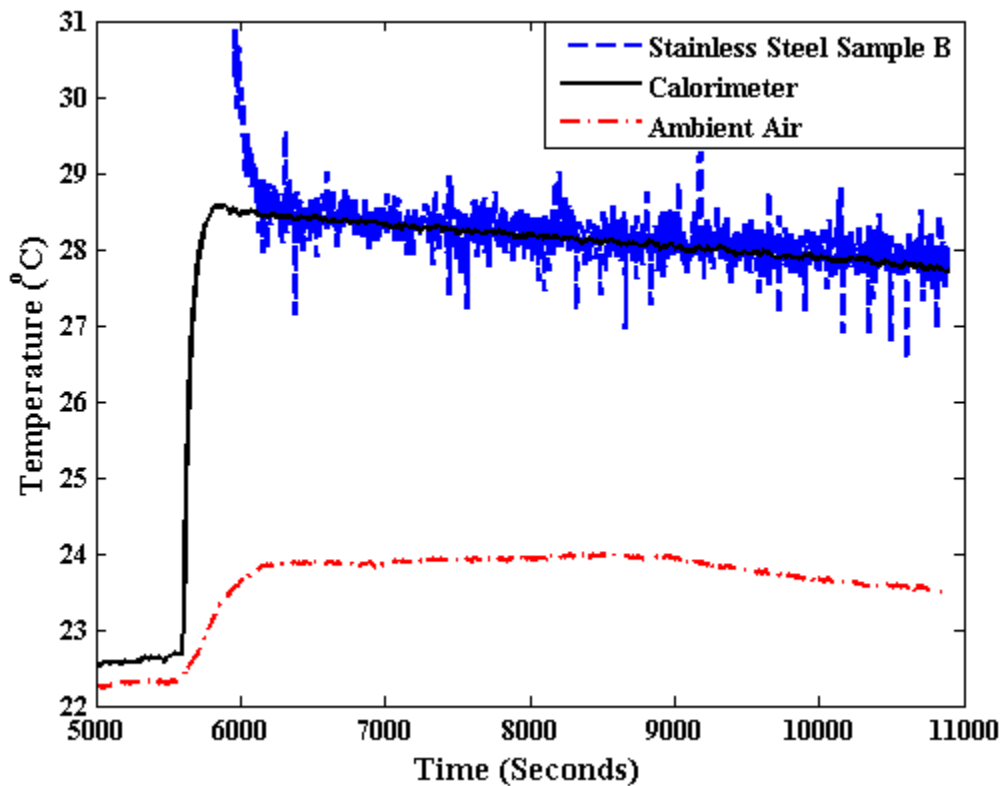
Figure 2.4. Example of transient temperatures from verification test [37]

The sample and calorimeter temperatures equilibrate after a certain time during the cooling process as desired, providing the information needed to determine the energy stored in the sample capsule from equations (2.1)-(2.7), as experimentally measured in the calorimeter run, Q_{EPCM_Exp}, compared with a theoretical value, Q_{EPCM_Theo}.

Results of this comparison can be expressed as percentage discrepancy between experimental and theoretical values of stored energy, expressed as:

$$Discrepency \ \% \equiv \frac{Q_{EPCM\_Theo} - Q_{EPCM\_Exp}}{Q_{EPCM\_Theo}} \times 100 \hspace{2cm} (2.9)$$

Results of these verification tests for energy balance, with four different samples, at initial temperatures varying from 250 $^{\circ}$C to 490 $^{\circ}$C, are tabulated in Table 2.4. For both sensible heat storage (with stainless steel) and phase change storage (with zinc), it is noticed that energy balances were satisfied within $\pm 1.5\%$ discrepancy. Thus, the accuracy of the calorimeter experiment is expected within $\pm 2.0\%$.

Table 2.4. Verification tests.

Sample (Initial Temperature)	Measured Energy Stored Q_{EPCM_Exp}(kJ)	Using Three Thermocouples around Sample		Using Internal Thermocouple	
		Theoretical Energy Stored Q_{EPCM_Theo}(kJ)	Discrepancy	Theoretical Energy Stored Q_{EPCM_Theo}(kJ)	Discrepancy
Stainless Steel Sample B Test 1 (490 $^{\circ}$C)	45.2	---	---	45.8	1.4 %
Stainless Steel Sample B Test 2 (250 $^{\circ}$C)	21.5	---	---	21.6	0.5 %
Stainless Steel Sample C Test 1 (280 $^{\circ}$C)	60.7	59.9	-1.3 %	60.6	-0.2 %
Zinc Sample A Test 1 (480 $^{\circ}$C)	45.9	46.2	0.6 %	---	---
Zinc Sample B Test 1 (490 $^{\circ}$C)	47.3	47.0	-0.8 %	---	---

2.4 Performance of EPCMs

Several types of PCMs have been tested, including metal materials (zinc, aluminum), inorganic salts ($NaNO_3$, $NaCl$, $MgCl_2$), and eutectic salts ($NaCl$-$MgCl_2$ eutectic).

2.4.1 Metal Materials

Zinc and aluminum (metal materials) are selected as PCMs, encapsulated by stainless steel shell. Thermal properties of both materials are well known. The properties of zinc are shown in Table 2.3 above. Thermal properties of aluminum are illustrated in Table 2.5.

Table 2.5. Thermal properties of aluminum [19,23].

	Melting Point ($^\circ$C)	Heat Capacity in Solid State (J/kg·K)				Heat Capacity in Liquid State (J/kg·K)	Latent Heat (kJ/kg)
		300 K	500 K	700 K	900 K		
Aluminum	660	903	1001	1086	1226	1177	397.3

Three zinc EPCMs and one aluminum EPCM were fabricated for the calorimeter experiments. Table 2.6 gives details of these samples, listing the phase change material, the encapsulation material, the capsule dimensions, and the mass of PCM in each sample.

Table 2.6. Metal based EPCM capsules.

	Encapsulation	Size	Mass of PCM (g)
Zinc EPCM 1	Stainless Steel 304	25.4 mm Diameter × 50.8 mm Height	103.7
Zinc EPCM 2	Stainless Steel 304	25.4 mm Diameter × 50.8 mm Height	97.7
Zinc EPCM 3	Stainless Steel 304	25.4 mm Diameter × 50.8 mm Height	96.6
Aluminum EPCM 1	Stainless Steel 304	25.4 mm Diameter × 50.8 mm Height	42.4

A typical example of temperature records obtained from one calorimeter experiment for zinc EPCM is displayed in Figures 2.5 and 2.6. Figure 2.5 displays the temperature history for the entire 1.65×10^4 seconds (around 4.6 hours) of the experiment, including the preheating charging period when the sample temperature was raised from room temperature to around 450 $^\circ$C. At time of approximately 8.5×10^3 seconds, the heated sample was immersed into the calorimeter fluid and began to thermally discharge,

equilibrating with the calorimeter temperature. Figure 2.6 shows an expanded trace of the equilibration process. These measurements of transient temperatures provided the requisite data for calculating energy stored in the EPCM capsule as it cooled from its charged temperature (450 $^{\circ}$C) to the discharged temperature (around 29 $^{\circ}$C), utilizing equations (2.1)-(2.7) as described above. Data of this nature occurs for each experiment for all the EPCM capsules.
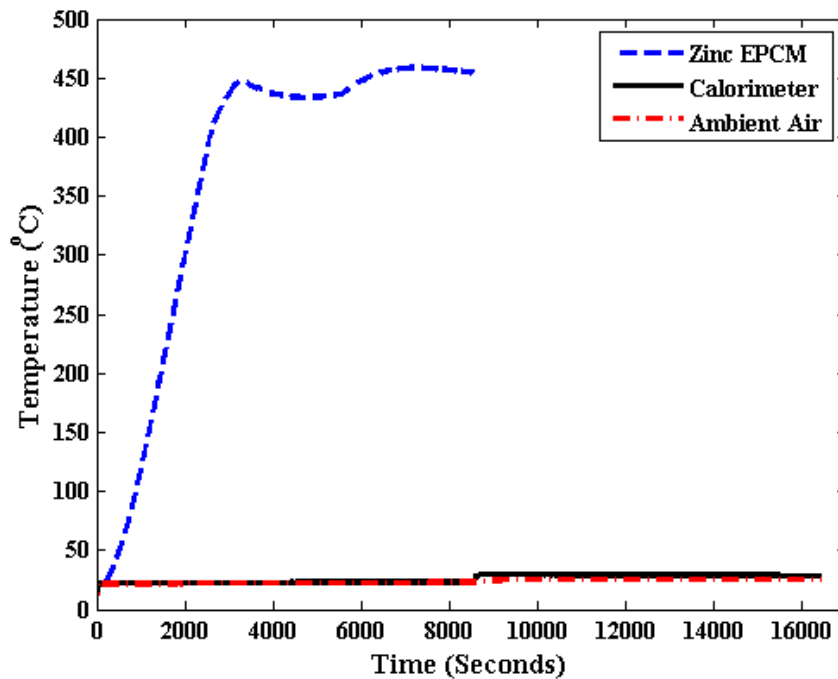
Figure 2.5. Example of temperature history for encapsulated phase change material in calorimeter experiment
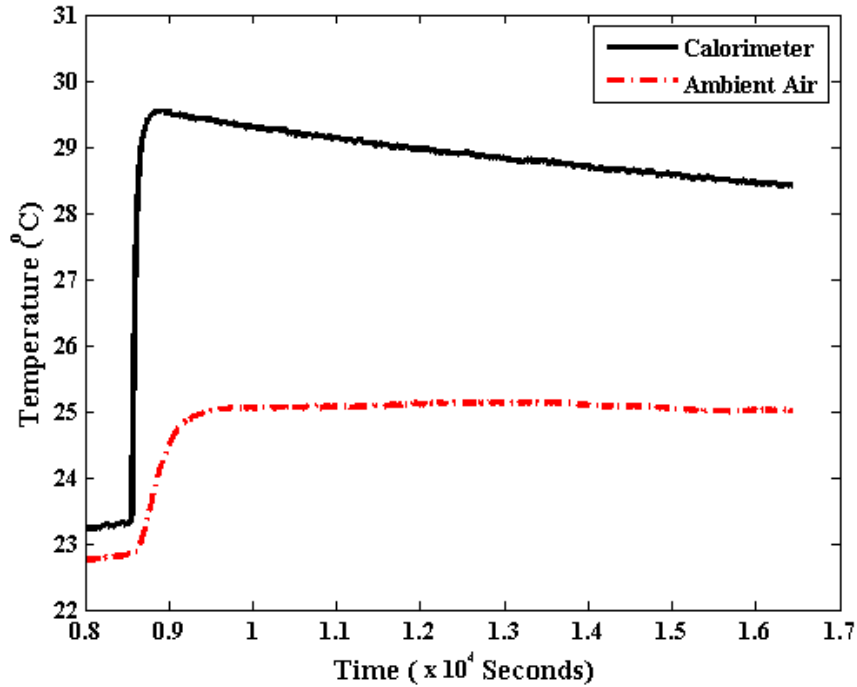
Figure 2.6. Expanded trace of temperature transient for ECPM during equilibration period in calorimeter experiment

Table 2.7 illustrates the thermal storage capability of zinc EPCM capsule after multiple charging/discharging cycles. Measured energy from EPCM is the total energy stored in the sample during heating process calculated through the calorimeter system. Anticipated energy is the theoretical energy stored in EPCM capsule calculated based on the properties of the materials. According to the experimental results, the measured total energy stored in the capsule decreases with thermal cycles. After about seven thermal cycles of heating/cooling process, the energy stored in the capsule is dropped approximately 12%.

The liquid state zinc interacts with stainless steel shell, forming an intermetallic compound between zinc and stainless steel during heating/cooling thermal cycles. The undesired alloy formed between metal materials would reduce the latent heat storage

capability of zinc. Therefore, the energy stored in the zinc EPCM diminishes with melting-freezing cycles.

Table 2.7. Energy stored in zinc-stainless steel EPCM (NO PAINT IN THE CAPSULE) in multiple thermal cycles.

Sample Cycling Number	Charged Temp. ($^{\circ}$C)	Discharged Temp. ($^{\circ}$C)	Anticipated Energy from Zinc EPCM (kJ)	Measured Energy from Zinc EPCM (kJ)	Ratio of Measured & Anticipated Energy from Zinc EPCM (%)
Zinc EPCM 1 Thermal Cycling 1	455	27	46.8	47.4	101.3
Zinc EPCM 1 Thermal Cycling 2	455	27	46.7	45.8	97.9
Zinc EPCM 1 Thermal Cycling 3	460	27	46.9	44.3	94.5
Zinc EPCM 1 Thermal Cycling 4	460	27	46.6	43.3	92.9
Zinc EPCM 1 Thermal Cycling 5	465	26	47.2	43.0	91.2
Zinc EPCM 1 Thermal Cycling 6	475	26.5	48.1	42.9	89.2
Zinc EPCM 1 Thermal Cycling 7	485	27.5	48.9	42.9	87.7

In order to reduce the deterioration of storage capability of zinc capsule, a type of less reactive material was used to paint inside the encapsulation shell to prevent the intermetallic compound formed between zinc and stainless steel. Tables 2.8 and 2.9 illustrate the energy stored in zinc capsule (with paint inside capsule) in multiple thermal cycles and after long-term exposure at high temperature. The paint material inside stainless steel shell can mitigate the problem a little, but the total energy still drops after hours of heating process. Sample was heated up to 450 $^{\circ}$C and held at this temperature for six hours, then cooled down, and heated up again to 450 $^{\circ}$C and held for six hours. Repeat this heating/cooling process six times, it got total 36 hours for heating process. The paint material inside the shell could not help to prevent the deterioration of storage capacity for EPCM after hours of heating/cooling process.

Table 2.8. Energy stored in zinc-stainless steel EPCM (PAINTED INSIDE CAPSULE) in multiple thermal cycles and after long-term exposure at high temperature.

Sample Cycling Number	Charged Temp. (°C)	Discharged Temp. (°C)	Anticipated Energy from Zinc EPCM (kJ)	Measured Energy from Zinc EPCM (kJ)	Ratio of Measured & Anticipated Energy from Zinc EPCM (%)
Zinc EPCM 2 Thermal Cycling 1	480	33.5	50.7	51.5	101.6
Zinc EPCM 2 Thermal Cycling 2	480	32.5	51.1	51.8	101.3
Zinc EPCM 2 Thermal Cycling 3	490	32	52.1	52.5	100.7
Zinc EPCM 2 Thermal Cycling 4	490	32	51.9	52.5	101.3
Zinc EPCM 2 After 36 hrs Heating Process at 450 °C	465	32	49.5	46.4	93.8
Zinc EPCM 2 After 36 hrs Heating Process at 450 °C	470	29	49.9	46.7	93.6
Zinc EPCM 2 After 36 hrs Heating Process at 450 °C	470	29.5	50.1	45.6	90.9

Table 2.9. Energy stored in zinc-stainless steel EPCM (PAINTED INSIDE CAPSULE) after long-term exposure at high temperature.

Sample Cycling Number	Charged Temp. (°C)	Discharged Temp. (°C)	Anticipated Energy from Zinc EPCM (kJ)	Measured Energy from Zinc EPCM (kJ)	Ratio of Measured & Anticipated Energy from Zinc EPCM (%)
Zinc EPCM 3 After 36 hrs Heating Process at 450 °C	450	29	48.2	47.7	99.0
Zinc EPCM 3 After 72 hrs Heating Process at 450 °C	445	30	47.3	44.5	94.0

Furthermore, aluminum EPCM capsule was also tested for its thermal performance, as illustrated in Table 2.10. It seems a little better than zinc capsule. There is no obvious thermal storage deterioration in aluminum capsule after several thermal cycles. Nevertheless, after 500 hours long-term exposure at 720 °C (aluminum melting point: 660 °C), the storage capability also decreases about 5%.

Based on the calorimetry tests for metal PCM capsules, metal based EPCMs are seen to have some problems with thermal energy storage because of the potential intermetallic compound formed between PCM and encapsulation material. The formed alloy between PCM and shell would reduce the latent heat storage of PCM. In order to use metals as PCMs in TES systems, less reactive encapsulation materials, such as ceramic, quartz, etc., should be used to encapsulate metal PCMs. Additional work is needed to draw definitive conclusions in this regard.

Table 2.10. Energy stored in aluminum EPCM in repeated thermal cycles and after long-term exposure at high temperature.

Sample Cycling Number	Charged Temp. ($^\circ$C)	Discharged Temp. ($^\circ$C)	Theoretical Energy from Aluminum EPCM (kJ)	Measured Energy from Aluminum EPCM (kJ)	Ratio of Measured & Theoretical Energy from Aluminum EPCM
Aluminum EPCM 1 Mini-Cycle 1	710	31.5	75.5	75.3	99.6 %
Aluminum EPCM 1 Mini-Cycle 2	710	31	75.3	74.1	98.4 %
Aluminum EPCM 1 Mini-Cycle 3	700	31.5	74.7	76.0	101.8 %
Aluminum EPCM 1 Mini-Cycle 4	720	30.5	76.1	74.6	98.0 %
Aluminum EPCM 1 Mini-Cycle 5	710	31	75.7	77.1	101.9 %
Aluminum EPCM 1 Mini-Cycle 6	710	32	75.5	76.0	100.7 %
After 500 hrs Heating Process at 720 $^\circ$C	704	31	74.9	72.4	96.6 %
After 500 hrs Heating Process at 720 $^\circ$C	715	33.5	75.9	72.1	95.1 %

2.4.2 Inorganic Salts

EPCMs with high melting temperature salts as PCMs were tested using immersion calorimetry experiments. $NaNO_3$, $NaCl$-$MgCl_2$ eutectic (57% mole fraction NaCl and

43% mole fraction MgCl$_2$), MgCl$_2$, and NaCl are selected as the PCMs. Specific enthalpies over the temperature ranges of interest for both solid and liquid phases, phase-transition temperatures, and latent heats of phase change are needed for the theoretical enthalpy changes. However, only some of these properties are available from literature.

Thermal properties of NaNO$_3$ as reported in the literature [14,17,18] have been used here; the melting temperature is reported to be 308 $^{\circ}$C [16]. Additionally, this salt is reported to have a solid-phase transition around 275 $^{\circ}$C [14,17,18]. For NaCl-MgCl$_2$ eutectic, the melting point was determined by differential scanning calorimeter (DSC) measurement to be 444 $^{\circ}$C (measured by Sabol, J.C. et al. of Material Science & Engineering Department in Lehigh University [38]). Melting point for MgCl$_2$ is 714 $^{\circ}$C [16] and the melting temperature of NaCl is 800 $^{\circ}$C [16]. Enthalpy values reported in the literature for NaNO$_3$ evidenced discrepancies [14,17,18]. No applicable enthalpy values were found in the literature for NaCl-MgCl$_2$ eutectic; the one reported value for latent heat is for a composition different than the eutectic composition [15]. There is also lack of enthalpy values for anhydrous MgCl$_2$ and NaCl from literature. Therefore, it is necessary to obtain some additional enthalpy data for these PCMs in the temperature ranges of interest.

Figure 2.7 shows enthalpy values of PCMs from calorimeter experiments. According to the calorimeter experiments, NaNO$_3$ experimental enthalpy values are close to the reference values. Compared the calibrated enthalpy values of these PCMs with the measured enthalpy values in multiple thermal cycles, it could test whether or not there is storage capacity deterioration in the EPCM capsule.

Enthalpy of NaNO₃
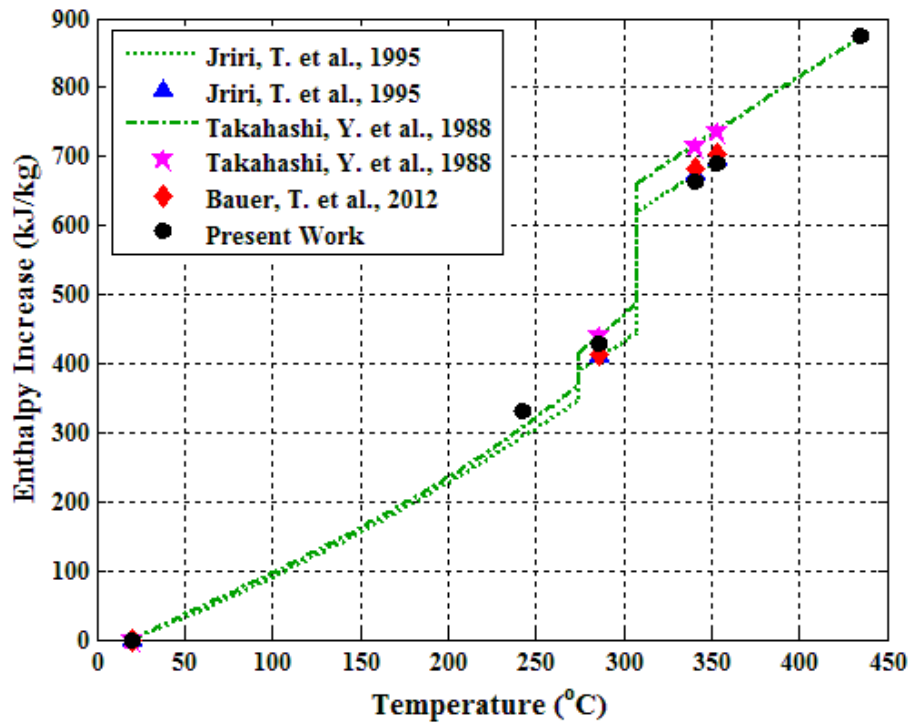
(a) Enthalpy changes of $NaNO_3$

Enthalpy of NaCl-MgCl₂ Eutectic
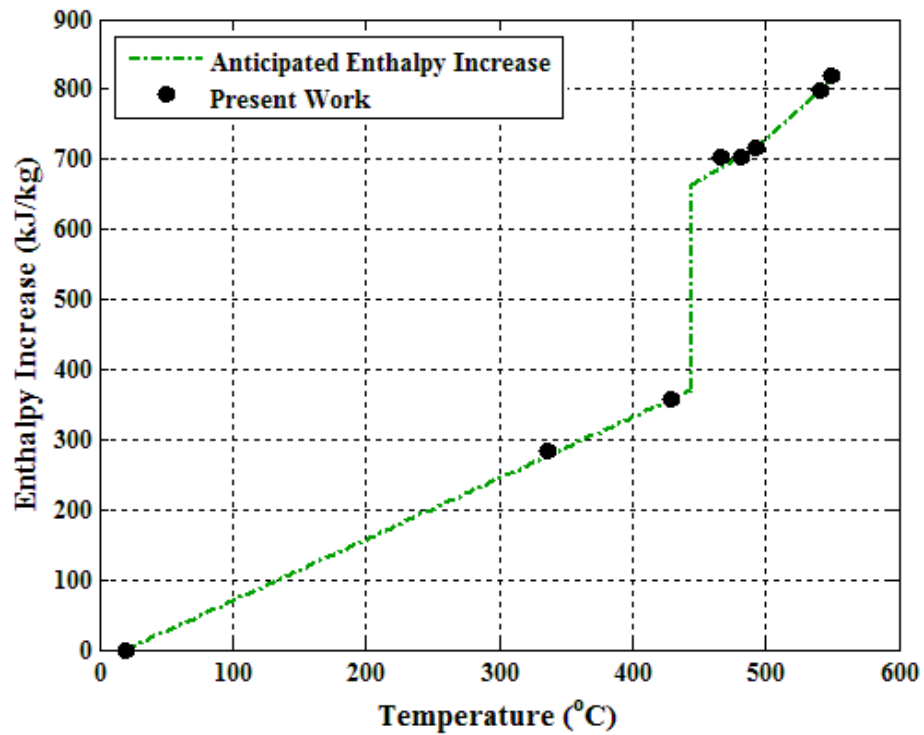
(b) Enthalpy changes of $NaCl$-$MgCl_2$ eutectic

28
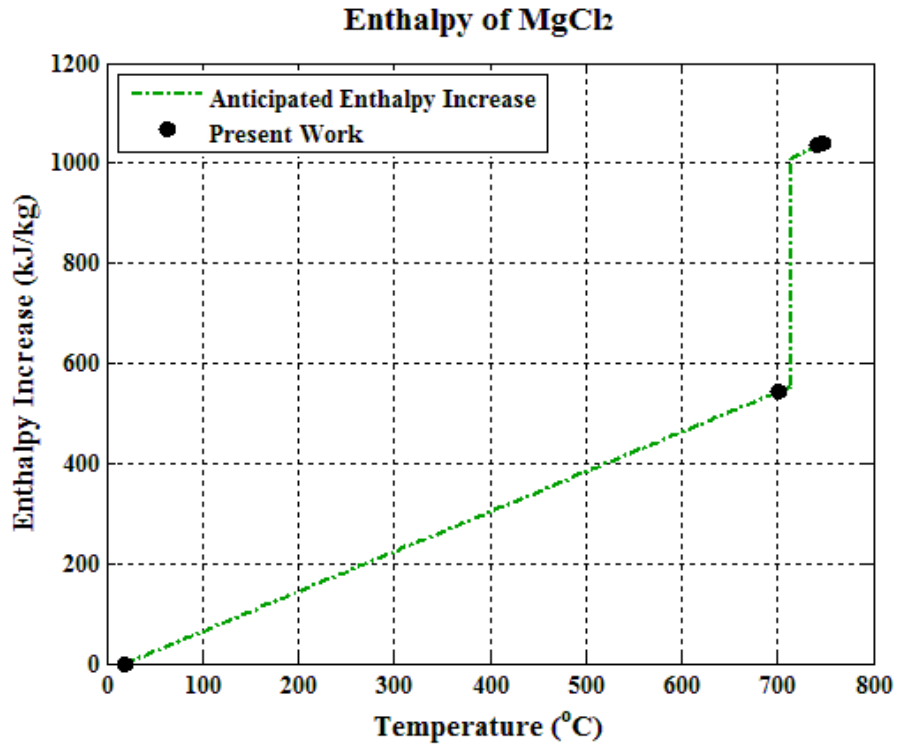
Enthalpy of MgCl₂

(c) Enthalpy changes of MgCl₂
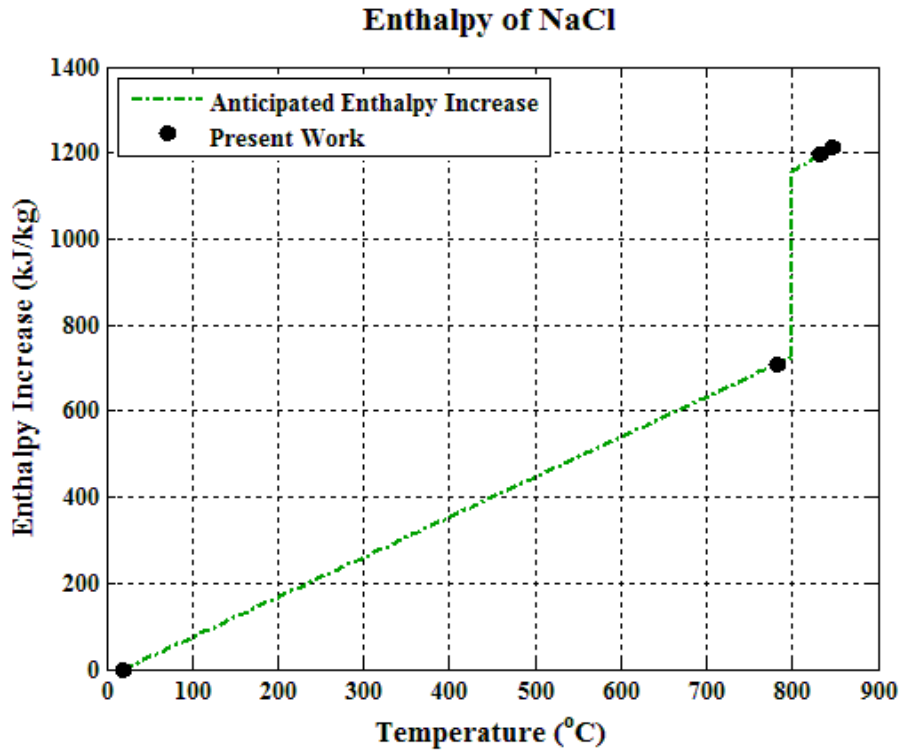
Enthalpy of NaCl

(d) Enthalpy changes of NaCl

Figure 2.7. Enthalpy changes in PCMs

There are twelve salt based EPCM capsules fabricated for calorimetry experiments. Table 2.11 gives details of these samples, listing the phase change material, the capsule material, the capsule dimensions, and the mass of PCM in each sample.

Table 2.11. Salt based EPCM capsules.

EPCM Samples	Encapsulation	Size	Mass of PCM (g)
$NaNO_3$ EPCM 1	Carbon Steel 1018	50.8 mm Diameter $\times$ 127 mm Height	269.6
$NaCl$-$MgCl_2$ Eutectic EPCM 1	Stainless Steel 304	25.4 mm Diameter $\times$ 50.8 mm Height	28.8
$NaCl$-$MgCl_2$ Eutectic EPCM 2	Stainless Steel 304	25.4 mm Diameter $\times$ 50.8 mm Height	23.9
$NaCl$-$MgCl_2$ Eutectic EPCM 3	Carbon Steel 1018	50.8 mm Diameter $\times$ 127 mm Height	284.6
$NaCl$-$MgCl_2$ Eutectic EPCM 4	Carbon Steel 1018	50.8 mm Diameter $\times$ 127 mm Height	282.5
$NaCl$-$MgCl_2$ Eutectic EPCM 5	Stainless Steel 304	25.4 mm Diameter $\times$ 50.8 mm Height	29.3
$NaCl$-$MgCl_2$ Eutectic EPCM 6	Stainless Steel 304	25.4 mm Diameter $\times$ 50.8 mm Height	29.6
$MgCl_2$ EPCM 1	Stainless Steel 304	25.4 mm Diameter $\times$ 50.8 mm Height	28.3
$MgCl_2$ EPCM 2	Stainless Steel 304	25.4 mm Diameter $\times$ 50.8 mm Height	26.1
$MgCl_2$ EPCM 3	Stainless Steel 304	25.4 mm Diameter $\times$ 50.8 mm Height	26.4
$NaCl$ EPCM 1	Stainless Steel 304	25.4 mm Diameter $\times$ 50.8 mm Height	27.0
$NaCl$ EPCM 1	Stainless Steel 304	25.4 mm Diameter $\times$ 50.8 mm Height	26.6

Table 2.12 displays the energy stored in salt based EPCM capsules at the initial thermal cycle. According to the calorimetry results, all of the four PCMs behaved as designed, storing thermal energy in a thermal cycle with completed phase change. Based on the theoretical amount of energy stored in a given thermal cycle as displayed in Figure 2.7, the actual amount of energy stored in the PCM calculated through each calorimeter experiment can be compared with it. It is noticed that in their first thermal cycles, the four PCM salts performed as designed with completed phase change. The agreement between theoretical and measured values is within 2%.

Table 2.12. Energy stored in EPCMs in initial thermal-cycle.

EPCM Samples	Charged Temp. ($^\circ$C)	Discharged Temp. ($^\circ$C)	Theoretical Stored Energy in EPCM Q_{EPCM_Theo}(kJ)	Measured Stored Energy in EPCM Q_{EPCM_Exp}(kJ)	Agreement – Ratio of Measured to Theoretical Energy stored (%)
NaNO$_3$ EPCM 1	350	47	237.4	236.7	99.7
NaCl-MgCl$_2$ Eutectic EPCM 1	490	29	41.6	41.8	100.5
NaCl-MgCl$_2$ Eutectic EPCM 2	490	28	38.6	39.1	101.3
NaCl-MgCl$_2$ Eutectic EPCM 3	490	50	264.0	262.7	99.5
NaCl-MgCl$_2$ Eutectic EPCM 4	490	51	264.5	269.5	101.9
MgCl$_2$ EPCM 1	745	33	58.2	58.5	100.4
MgCl$_2$ EPCM 2	745	33	56.1	56.0	99.9
MgCl$_2$ EPCM 3	745	33	56.2	56.6	100.8
NaCl EPCM 1	830	30	65.0	64.3	98.9
NaCl EPCM 2	850	30	65.9	66.3	100.5

Figures 2.8 and 2.9 represent the agreement between measured energy and theoretical energy stored in salt based EPCM capsules in multiple thermal cycles in order to examine whether or not the storage capacity of EPCMs would diminish. Such diminishment could imply undesirable changes in the salt medium, possibly due to chemical interaction with the capsule walls. The graphs do not show obvious diminishment of storage capacity of the four kinds of EPCMs after repeated thermal cycles. The agreements remains within 2% for all cycles and all kinds of salt based EPCM samples. Thus, within the test ranges, storage deterioration was not observed.
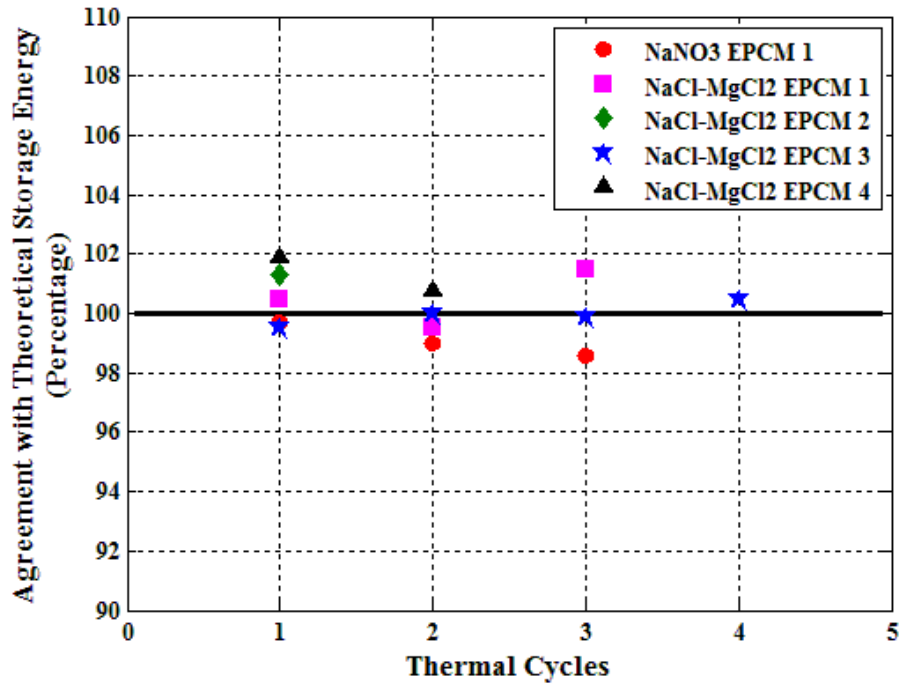
Figure 2.8. Storage performance of $NaNO_3$, $NaCl-MgCl_2$ eutectic ECPM samples over multiple thermal cycles
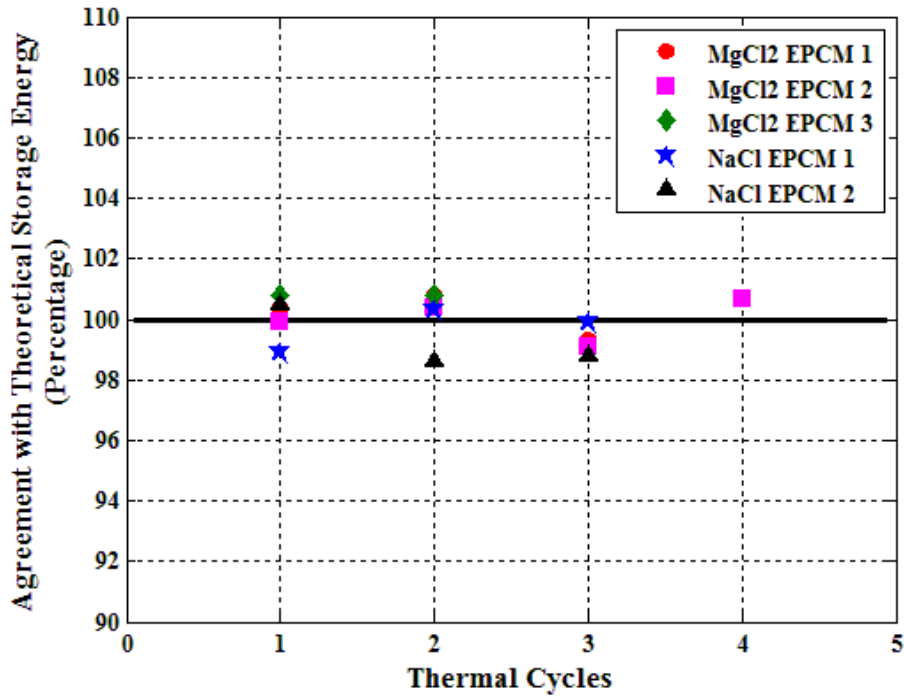
Figure 2.9. Storage performance of $MgCl_2$, NaCl ECPM samples over multiple thermal cycles

Furthermore, storage performance of ECPM after long-term exposure to high temperatures is examined. This was of particular interest for the NaCl-MgCl$_2$ eutectic salt and for exceedingly high melting temperature PCMs, MgCl$_2$ and NaCl, since their operating temperatures would exceed 400 $^\circ$C or much higher. Five of the NaCl-MgCl$_2$ eutectic samples of different dimensions with different encapsulation steels were subjected to long exposures at elevated temperatures. Three of these capsules were heated to 470 $^\circ$C (above the melting point of NaCl-MgCl$_2$ eutectic), held at that temperature for six hours, and then cooled down to 300 $^\circ$C (below the melting point) and held at 300 $^\circ$C for two hours – comprising one long-term thermal cycle. Repeating the cycle 50 times, accumulated 300 hours total exposure at 470 $^\circ$C. The other two NaCl-MgCl$_2$ eutectic samples were heated to 450 $^\circ$C and held at that temperature for 500 hours. MgCl$_2$ capsules were preheated to 750 $^\circ$C (above the melting point of MgCl$_2$) and held at that temperature for eight hours, and then cooled down to 500 $^\circ$C (below the melting point) and held at 500 $^\circ$C for two hours – comprising one long-term thermal cycle. Magnesium chloride EPCM 1, repeating the long-term cycle 14 times, was accumulated 112 hours total exposure at 750 $^\circ$C. MgCl$_2$ EPCM 2 experienced 320 hours exposure at 750 $^\circ$C by repeating the cycle 40 times, while MgCl$_2$ EPCM 3 had 480 hours exposure at 750 $^\circ$C by repeating the cycle 60 times. For NaCl EPCM 2, it was heated to 850 $^\circ$C (above the melting point of NaCl) and held at that temperature for 1000 hours.

After long-term exposure to high temperature environments (hundreds of hours of heating process above the melting points of the PCMs), these EPCM capsules were tested using the calorimeter to examine their storage performance, as illustrated in Table 2.13.

Based on the calorimetry results, it does not show discernible deterioration in storage capacity of salts based EPCMs. Therefore, salt phase change materials are capable for thermal energy storage.

Table 2.13. Energy stored in EPCMs in final thermal-cycle after long-term exposure at high temperatures.

EPCM Samples	Exposure	Theoretical Stored Energy in EPCM Q_{EPCM_Theo}(kJ)	Measured Stored Energy in EPCM Q_{EPCM_Exp}(kJ)	Agreement – Ratio of Measured & Theoretical Energy from EPCM (%)
NaCl-MgCl$_2$ Eutectic EPCM 1	300 hours at 470 °C	41.9	41.5	99.0
NaCl-MgCl$_2$ Eutectic EPCM 2	300 hours at 470 °C	38.7	38.4	99.2
NaCl-MgCl$_2$ Eutectic EPCM 3	300 hours at 470 °C	265.5	265.5	100.0
NaCl-MgCl$_2$ Eutectic EPCM 5	500 hours at 450 °C	38.7	39.4	101.8
NaCl-MgCl$_2$ Eutectic EPCM 6	500 hours at 450 °C	39.6	39.7	100.1
MgCl$_2$ EPCM 1	112 hours at 750 °C	58.7	59.1	100.6
MgCl$_2$ EPCM 2	320 hours at 750 °C	56.0	55.9	99.9
MgCl$_2$ EPCM 3	480 hours at 750 °C	56.7	57.1	100.7
NaCl EPCM 2	1,000 hours at 850 °C	66.0	67.3	102.0

2.5 Conclusions

Calorimeter experiments indicate that the storage capability of metal EPCM, e.g. in zinc-stainless steel EPCM, aluminum-stainless steel EPCM, decreases with thermal cycles or after long-term exposure to high temperatures. This is hypothesized to be because of inter-metallic diffusion between the metal PCM materials and the encapsulation metals during high temperature melting/solidification process. Thus it is conceivable that metal PCM materials encapsulated by certain materials are not suitable for TES; less reactive encapsulation materials, e.g. ceramic, quartz, etc., are used with these PCMs. This matter needs further study.

Salt EPCM capsules showed no discernible deterioration in storage capacity over multiple thermal cycles and even after long-term (hundreds of hours) exposure at high temperatures. Therefore, salts, such as $NaNO_3$, $NaCl$-$MgCl_2$ eutectic, $MgCl_2$ and $NaCl$, based EPCMs are good candidates for TES for temperatures above 300 $^{\circ}$C based on the current lab scale studies. Nevertheless, corrosion tests are needed to determine the longevity of these EPCMs before being applicable for CSP plants.

CHAPTER 3

ONE-DIMENSIONAL HEAT TRANSFER ANALYSIS

3.1 Motivation

Heat transfer modeling of the thermal diffusion for various Phase Change Materials (PCM) conditions is conducted as part of this work. Numerical simulations of the heat transfer could help us appreciate and understand the heat transfer process inside single EPCM capsule in order to assist with the design of EPCM based thermoclines. Initially, to simplify the simulation model, one-dimensional heat transfer analysis is considered here with the heat flux in radial direction of cylinder.

3.2 Mathematical Modeling

Numerical simulations are conducted here for capsules to simulate storage/retrieval of thermal energy into/from encapsulated phase change materials. $NaNO_3$, $NaCl\text{-}MgCl_2$ eutectic and $MgCl_2$ are considered for the simulations here. $NaNO_3$, $NaCl\text{-}MgCl_2$ eutectic, $MgCl_2$ in the core region have melting temperatures of 308 $^{\circ}$C, 444 $^{\circ}$C, 714 $^{\circ}$C, respectively. The latent heats of $NaNO_3$, $NaCl\text{-}MgCl_2$ eutectic and $MgCl_2$ are 162.5 kJ/kg, 292 kJ/kg and 454 kJ/kg, respectively, according to the enthalpy values measured by the calorimetry experiments and presented in Chapter 2. Stainless steel is applied as the encapsulation shell outside PCMs. The melting temperature of stainless steel shell is much higher than the operating temperature of the thermal storage unit.

The heat will be transferred from/to heat transfer fluid to/from phase change material through stainless steel encapsulation layer by conduction. When the melting temperature

36

of PCM is reached, the melting/freezing interface separating the solid PCM from liquid PCM will be formed.

In order to simplify the mathematical model, present heat transfer analysis considers uniform heat transfer coefficient around the capsule. Thus, in this simplified model that the heat flux is only in radial direction. The following assumptions are adopted for this model:

- PCM is a pure substance, no moisture or impurities so the sub-cooling effects are negligible.

- The convective heat transfer coefficient is uniform around the capsule so the diffusion is only in the radial direction.

- The capsule is incompressible.

- Physical properties are constant during each phase.

- The buoyancy-driven convection in the molten PCM is negligible.

- No volume change between solid state and liquid state PCM.

The geometry of the composite capsule is shown in Figure 3.1. R_1 is the outer radius of capsule, and R_2 is the radius of the phase change material. The liquid/solid interface is located at $r = s(t)$. The location of the interface is unknown and it has to be determined as a part of the solution. This is a moving boundary problem and is nonlinear in nature.
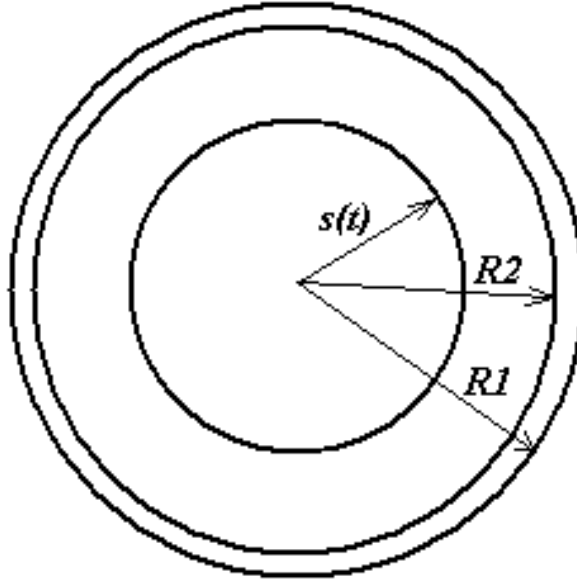
Figure 3.1. Schematic of the capsule

The equation governing the unsteady heat diffusion in each composite layer is of the form:

$$\rho_j c_j \frac{\partial T_j}{\partial t} = k_j \left[\frac{1}{r} \frac{\partial}{\partial r} \left(r \frac{\partial T_j}{\partial r} \right) \right] \tag{3.1}$$

where ρ_j is density; c_j is specific heat; k_j is thermal conductivity; T_j is temperature distribution in each layer; r is the radial distance; t is the time. Furthermore, the suffix j equals 1, 2, or 3 for the thin layered shell, liquid phase, or solid phase of the phase change material, respectively for the charging process.

The boundary conditions imposed on the temperature field in each layer for charging process are as follows:

$$-k_1 \frac{\partial T_1}{\partial r} = h(T_1 - T_f) \text{ , at } r = R_1 \tag{3.2}$$

$$-k_1 \frac{\partial T_1}{\partial r} = -k_2 \frac{\partial T_2}{\partial r} \text{ , and } T_1 = T_2, \text{ at } r = R_2 \tag{3.3}$$

$$-k_2 \frac{\partial T_2}{\partial r} = -k_3 \frac{\partial T_3}{\partial r} + L\rho_2 \frac{ds(t)}{dt} \text{ , } T_2 = T_3 = T_m, \text{ at } r = s(t) \tag{3.4}$$

38

$$\frac{\partial T_3}{\partial r} = 0, \text{ at } r = 0 \tag{3.5}$$

where h is the convective heat transfer coefficient; T_m is the melting temperature of the PCM; T_f is the temperature of heat transfer fluid; L is latent heat of the PCM; $s(t)$ is the location of the liquid/solid interface in PCM. Initially, $T(r, 0) = T_o$, which is constant.

The average convective heat transfer coefficient for cross flow around the circular cylinder could be determined by equation (3.6) [19].

$$Nu = \frac{hD}{k_f} = C Re_D^m Pr^{1/3} \tag{3.6}$$

where k_f is the thermal conductivity of heat transfer fluid; D is the diameter of the EPCM; Re_D is Reynolds number; Pr is Prandtl number; C and m are two constants.

The equations (3.1)-(3.5) can be non-dimensionalized by measuring radius in R_1, time in R_2^2/α_2, where $\alpha_2 = k_2/(\rho_2 c_2)$ is the thermal diffusivity of layer 2 (liquid phase of PCM). Temperature in each layer during charging process is normalized as $\theta_j = (T_j - T_o)/(T_f - T_o)$. The non-dimensional governing equation becomes:

$$\frac{\alpha_2 R_{12}^2}{\alpha_j} \cdot \frac{\partial \theta_j}{\partial \tau} = \frac{1}{R} \cdot \frac{\partial \theta_j}{\partial R} + \frac{\partial^2 \theta_j}{\partial R^2} \tag{3.7}$$

where $R_{12} = R_1/R_2$; $\alpha_j = k_j/(\rho_j c_j)$ thermal diffusivity of each layer; τ is dimensionless time (Fourier number); R is dimensionless radius. The boundary conditions become:

$$-\frac{\partial \theta_1}{\partial R} = H(\theta_1 - 1) \text{ , at } R = 1; \tag{3.8}$$

$$\frac{\partial \theta_1}{\partial R} = K_1 \frac{\partial \theta_2}{\partial R} \text{ , at } = R_2/R_1 ; \tag{3.9}$$

$$-\frac{\partial \theta_2}{\partial R} = -K_2 \frac{\partial \theta_3}{\partial R} + \lambda \cdot \frac{\partial R}{\partial \tau} \text{ , at } R = S(t); \tag{3.10}$$

$\frac{\partial \theta_3}{\partial R} = 0$, at $R = 0$ (θ is bounded at $R = 0$); (3.11)

where $H = hR_1/k_1$ is the dimensionless heat transfer coefficient; $K_1 = k_2/k_1$; $K_2 = k_3/k_2$; $\lambda = L\rho_2\alpha_2 R_{12}^2/[k_2(T_f - T_o)]$; $S(t) = s(t)/R_1$; R is dimensionless radius. For charging process, initially, $\theta_1(R,0) = \theta_3(R,0) = 0$.

The simulation for melting or solidification process first uses the boundary condition at the liquid/solid interface in the phase change material, equation (3.10), and as an initial condition uses the current location of the interface to determine next time step calculations. The interface location is used to determine the temperature profiles in the next time step through governing equation (3.7) and boundary condition equations (3.8), (3.9), and (3.11). Thus, it is possible to determine the temperature profiles and liquid/solid interface movement for all times by repeating this process.

Boundary condition at the liquid/solid interface (3.10) is solved by explicit method while the governing equation with the rest of the boundary conditions is solved by implicit method. There is limitation for length of time step when using explicit method. However, for such a calculation, since the values of latent heat and density for liquid state PCM in equation (3.10) are extremely large, the maximum allowable value of time step could be as large as 10^4 seconds. The actual dimensionless time step is limited by other criteria and is in the 0.1 to 1.0 range.

Spatial and temporal convergence tests were conducted using various numbers of grid spacing in radial direction and a range of time steps. The results of the convergence test

are displayed in Table 3.1 and Table 3.2. For a 75 mm diameter $NaNO_3$ EPCM capsule, using liquid Therminol/VP-1 as HTF, the melting times do not vary significantly when the number of nodal points in radial direction is more than 30. The changes in melting times become small when the dimensionless time step $\Delta\tau$ is less than 1.0, as illustrated in Table 3.2. The results of numerical simulations presented here are obtained using 55 nodal points in the radial direction and using 0.3 as a dimensionless time step.

Table 3.1. Times of melting process for spatial convergence.

Number of Nodal Points	$\Delta\tau = 0.3$
30	70.9 min
55	72.9 min
105	72.9 min

Table 3.2. Times of melting process for temporal convergence.

Number of Nodal Points	$\Delta\tau = 0.1$	$\Delta\tau = 0.3$	$\Delta\tau = 0.5$	$\Delta\tau = 1.0$
55	72.9 min	72.9 min	72.9 min	73.2 min

The physical properties of $NaNO_3$, $NaCl\text{-}MgCl_2$ eutectic and $MgCl_2$ are shown in Table 3.3. Since the properties do not vary significantly in the temperature range used for the current simulation, the physical properties for each phase are determined at the average value of temperature of each phase.

The thickness of the stainless steel shell is 1.5875 mm (1/16 inch). For various PCM encapsulations, the HTF temperature varies between 210 $^{\circ}$C and 410 $^{\circ}$C, 340 $^{\circ}$C and 540 $^{\circ}$C and between 300 $^{\circ}$C and 800 $^{\circ}$C for $NaNO_3$, $NaCl\text{-}MgCl_2$ eutectic and $MgCl_2$, respectively. Simulations are conducted by choosing both gas and liquid as HTFs. The outside HTF heat transfer coefficient for each fluid is calculated using equation (3.6). To calculate the convective heat transfer coefficient for HTF, physical properties of air are used for the case of gas as heat transfer fluid, while the properties of Therminol/VP-1 are

used for the calculation in the case of liquid HTF. The physical properties of air and Therminol/VP-1 are listed in Table 3.4.

Table 3.3. Physical properties of NaNO$_3$, NaCl-MgCl$_2$ eutectic and MgCl$_2$.

	Melting Points ($^\circ$C)	Density (kg/m^3)	Thermal Conductivity (W/m·K)	Specific Heat (J/kg·K)	Latent Heat (kJ/kg)
NaNO$_3$	308 [16]	2260 [14] (Solid)	0.5 [16] (Solid)	1600 [a] (Solid)	162.5 [a]
		1900 [39] (Liquid)	0.5 [16] (Liquid)	1650 [a] (Liquid)	
NaCl-MgCl$_2$ Eutectic	444 [38]	2072 [39,40] (Solid)	0.5 [41] (Solid)	874 [a] (Solid)	292 [a]
		1750 [39] (Liquid)	0.5 [41] (Liquid)	1100 [a] (Liquid)	
MgCl$_2$	714 [16]	2230 [16] (Solid)	0.6 [16] (Solid)	798 [a] (Solid)	454 [a] [16]
		1675 [16] (Liquid)	1.2 [16] (Liquid)	974 [a] [16] (Liquid)	

[a] Established by the calorimetry experiments at Lehigh University

Table 3.4. Physical properties of air [19] and liquid Therminol/VP-1 [42].

	Air (1 atm, 800 K)	Liquid Therminol/VP-1 (698 K)
Density (kg/m^3)	0.4	654
k (W/m·K)	0.06	0.07
c (J/kg·K)	1099	2760
Viscosity (N·s/m^2)	3.7×10^{-5}	1.3×10^{-4}
Prandtl number, Pr	0.7	5.3

3.3 Results and Discussion

Results of the computational procedures described above are enumerated and discussed here. The heat transfer into the EPCM is driven by the convective heat transfer coefficient based on the outside flow conditions and for the cross flow past the cylindrical EPCM are governed by the Reynolds number and position around the cylinder. For the two HTF used, the Reynolds numbers (*Re*) are as follows. For air, *Re* = 147 for 10 mm diameter capsule, 367 for 25 mm capsule, 734 for 50 mm capsule, 1,101 for 75 mm capsule and 1,468 for 100 mm capsule. For liquid Therminol/VP-1, *Re* = 4,881 for 10 mm capsule, 12,201 for 25 mm capsule, 24,403 for 50 mm capsule, 36,604 for 75 mm

capsule and 48,806 for 100 mm capsule. The heat transfer inside the EPCM based on the above Re and the dependent Nusselt numbers are described below.

Figures 3.2 and 3.3 depict the temperature profiles in a 75 mm diameter $NaNO_3$ capsule during charging process with air as HTF. Figure 3.2 shows the variation of temperature distributions at various times. Here, τ is dimensionless time or Fourier number.
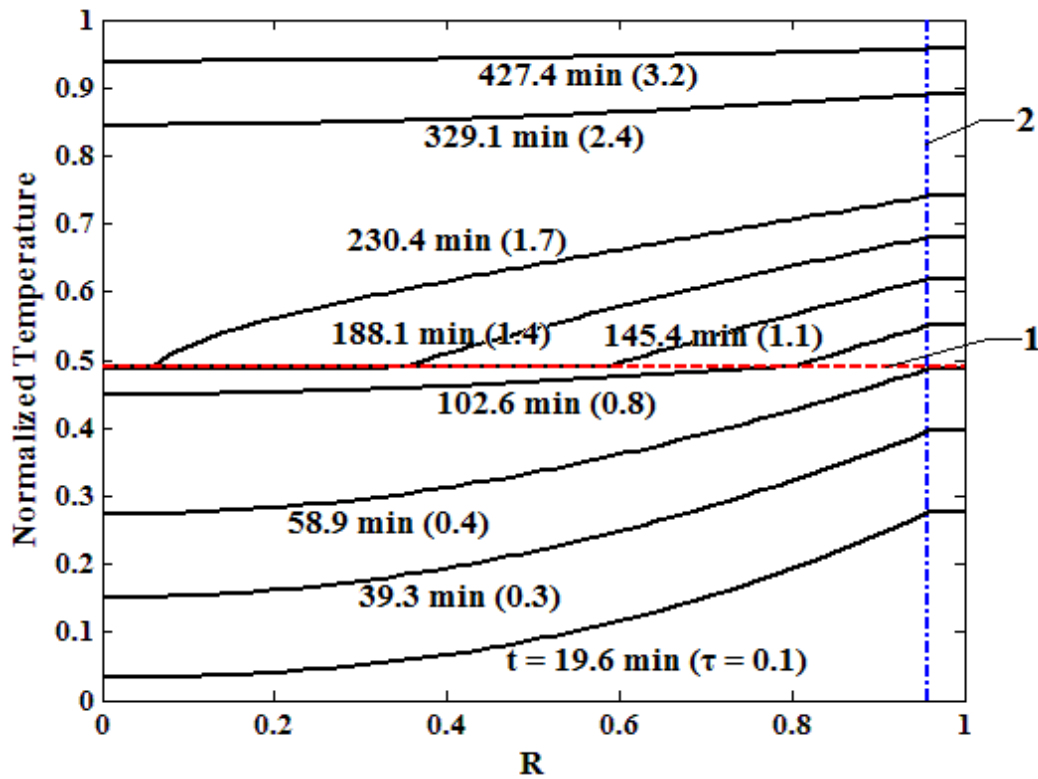
1- Normalized melting point = 0.49
2- Location of PCM/encapsulation shell interface

Figure 3.2. Temperature versus radius at different times for charging process with air as HTF

At the early stage of energy storage/charging process, all of the PCM is in the solid state. Heat diffuses from the surface of capsule to the center of capsule. For air as HTF, after around 60 minutes, the PCM starts to melt. At the beginning of melting process, the interface is located very close to the $NaNO_3$/stainless steel interface. At time, t = 103

43

minutes, the interface moves inward to radial location, $R \cong 0.8$. The temperature in the solid region is near melting point of $NaNO_3$ (308 $^\circ$C; normalized melting point: $\theta_m = (T_m - T_o)/(T_f - T_o) = 0.49$), and the temperature in the molten salt PCM and steel layer rises above melting temperature. A little later (~230 minutes) in the melting process, the interface moves closer to the cylinder center.

Temperature variation with time at different locations in a $NaNO_3$ capsule for air as HTF is shown in Figure 3.3. $R = 0$ represents the center of capsule while $R = 1$ represents the outer surface of capsule. The temperature at outer surface increases and reaches the melting point first. Then, heat flux diffuses inwards to the center of capsule. After about 231 minutes, all the PCM is melted and is in the liquid state. The temperature of PCM increases beyond the melting temperature after the melt-front passes through it.

Figure 3.3. Temperature versus time at different locations for charging process with air as HTF

Figures 3.4 and 3.5 display the temperature profiles in EPCM for 75 mm diameter $NaNO_3$ capsule during discharging process with air as HTF. Figure 3.4 is the temperature distributions in capsule at various times during discharging process. At the beginning of discharging process, the PCM is in liquid state. After about 57.0 minutes, the PCM begins to solidify from the PCM/shell interface, and the freezing-front moves inwards. During the solidification process, the PCM becomes to the solid state as the freezing-front passes through it. And the temperature in solid decreases significantly while the temperature in liquid always maintains slightly above the melting point.

1- Normalized melting point = 0.49
2- Location of PCM/encapsulation shell interface

Figure 3.4. Temperature versus radius at different times for discharging process with air as HTF

Figure 3.5 shows the temperature variations with time at different locations in the capsule. The surface temperature ($R = 1$) first drops to the melting point. After about 258 minutes, all the PCM solidifies to solid state. When the freezing-front passes, solid PCM temperature decreases rapidly to HTF temperature.

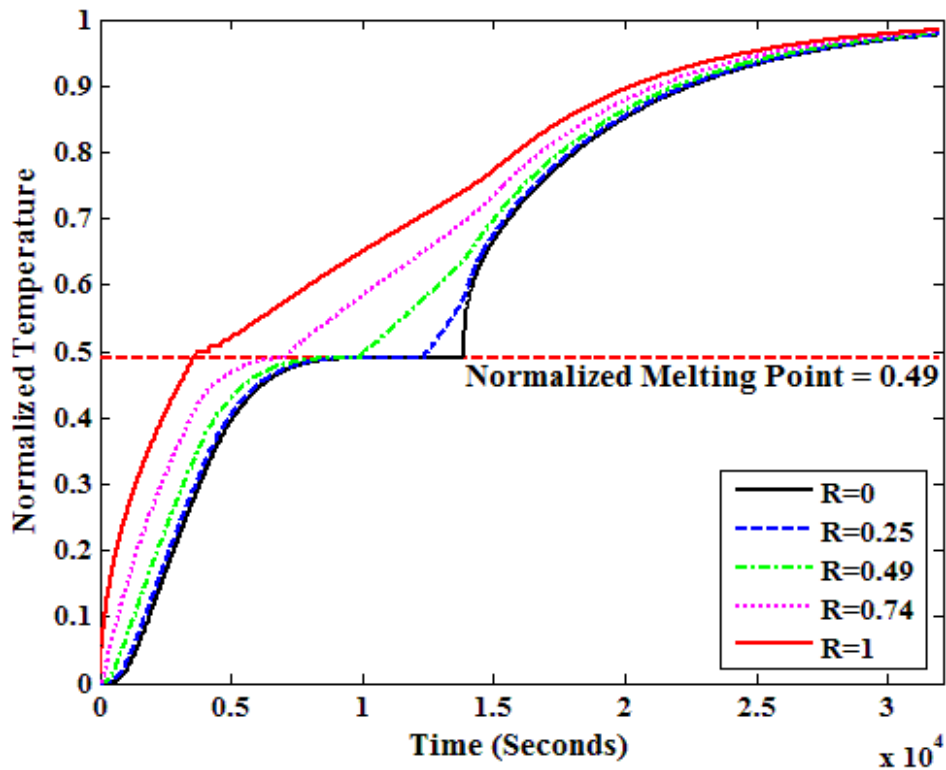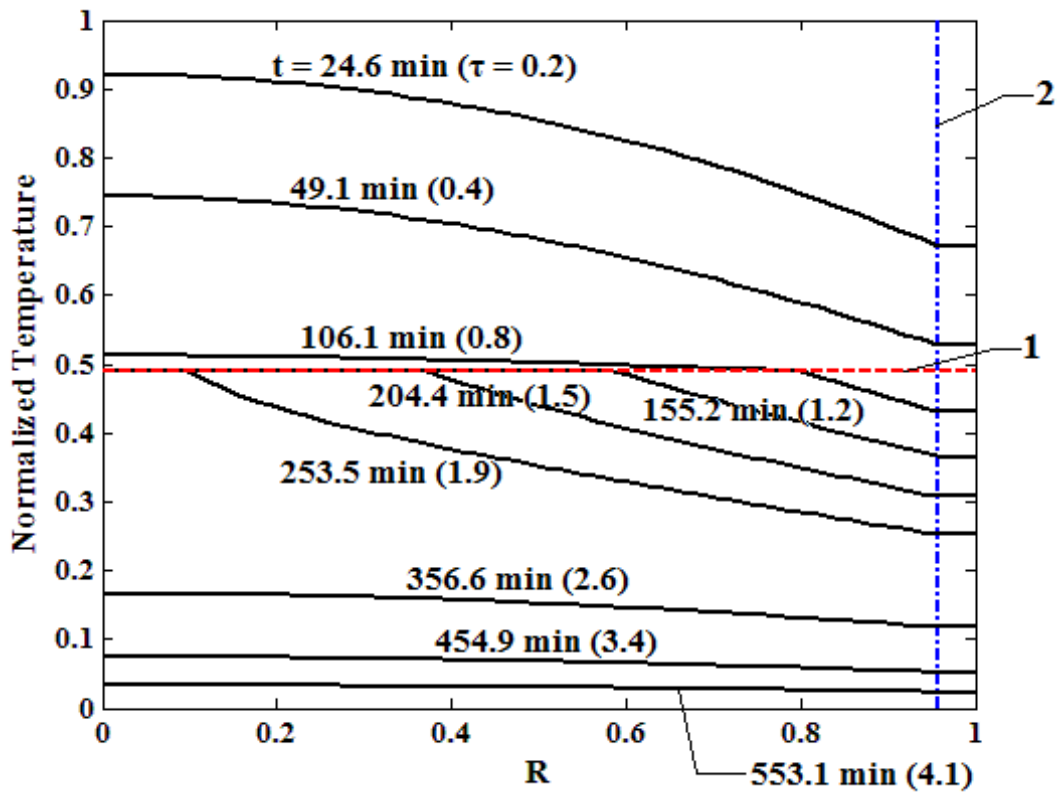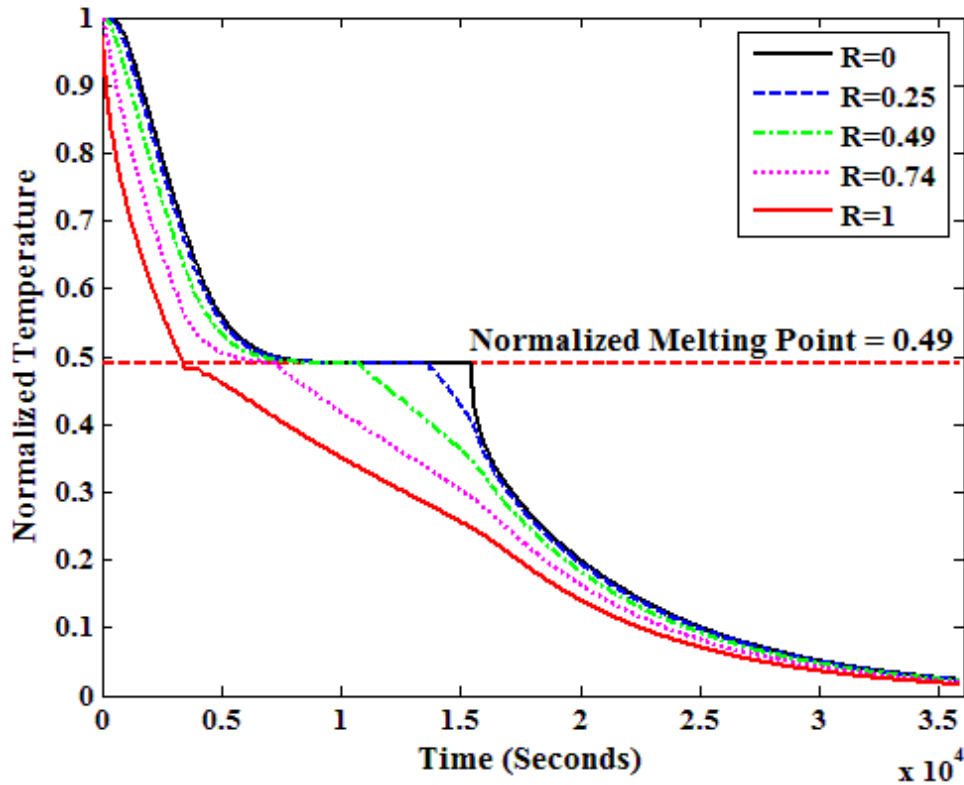**Figure 3.5. Temperature versus time at different locations for discharging process with air as HTF**

Figure 3.6 displays the liquid/solid interface movement in PCM during phase change process for 75 mm diameter $NaNO_3$ capsule with air as HTF. The melting/freezing front is first formed at the encapsulation shell, and then propagates radially inward. During melting process, the liquid/solid interface reaches the origin of the cylinder within 171.0 minutes, as shown in Figure 3.6(a). Figure 3.6(b) represents the liquid/solid interface movement in PCM during solidification process. It takes approximately 200 minutes for

the NaNO$_3$ PCM in a 75 mm diameter capsule to solidify to solid state when using air as HTF.

(a) Melting process

(b) Solidification process
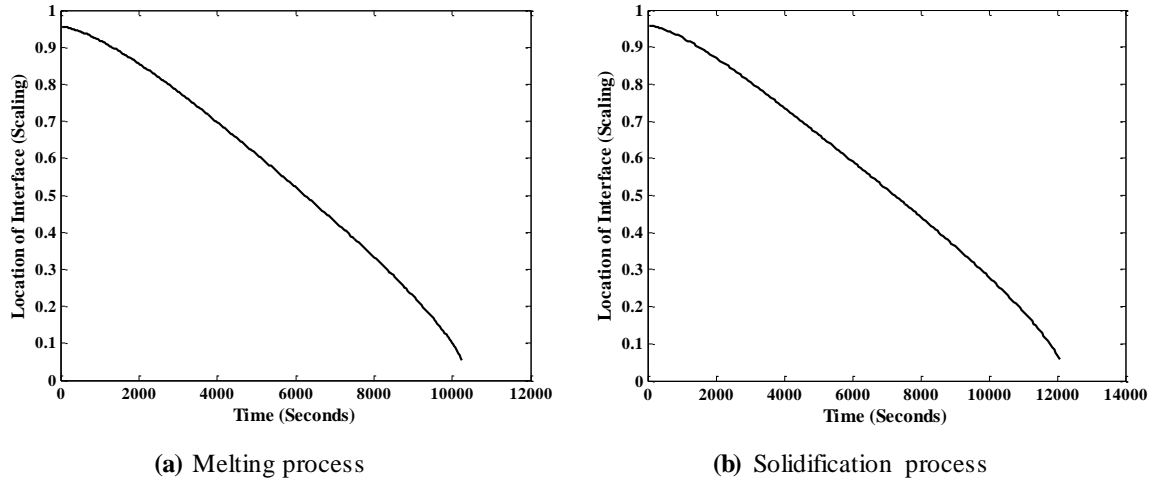
Figure 3.6. Locations of interface between solid state PCM and liquid state PCM during phase change process for air as HTF

In Tables 3.5 and 3.6 are the total heat transfer times for charging process with different types of HTFs, air and liquid Therminol/VP-1 are presented. Based on the numerical simulation results, as expected the heat transfer times are longer for larger sizes of EPCM capsules. Furthermore, the heat transfer times are much shorter when using liquid HTF instead of air. Properties of PCMs including density, heat capacity, thermal conductivity and latent heat would also affect the total heat transfer times and thus various PCMs could have different energy storage times.

Table 3.5. Total heat transfer times for charging process with air.

Diameter	NaNO$_3$	NaCl-MgCl$_2$ Eutectic	MgCl$_2$
10 mm	20.2 min	18.8 min	16.6 min
25 mm	88.9 min	77.8 min	74.0 min
50 mm	275.7 min	236.5 min	229.4 min
75 mm	534.0 min	458.8 min	438.6 min
100 mm	859.8 min	736.3 min	704.0 min

Table 3.6. Total heat transfer times for charging process with liquid Therminol/VP-1.

Diameter	NaNO$_3$	NaCl-MgCl$_2$ Eutectic	MgCl$_2$
10 mm	2.2 min	2.0 min	1.6 min
25 mm	14.9 min	13.5 min	9.2 min
50 mm	60.8 min	54.0 min	34.8 min
75 mm	137.1 min	121.4 min	75.2 min
100 mm	241.6 min	213.6 min	128.0 min

Data in Tables 3.7 and 3.8 illustrate the total heat transfer times for discharging process with different types of HTFs, air and liquid Therminol/VP-1. For MgCl$_2$ EPCM capsules, the discharging times are shorter than the charging times because the HTF temperature chosen for the charging process is close to the melting temperature of MgCl$_2$ (714 $^{\circ}$C) providing a small differential temperature for the heat transfer.

Table 3.7. Total heat transfer times for discharging process with air.

Diameter	NaNO$_3$	NaCl-MgCl$_2$ Eutectic	MgCl$_2$
10 mm	21.4 min	18.5 min	12.6 min
25 mm	97.6 min	77.4 min	47.4 min
50 mm	306.2 min	236.6 min	138.2 min
75 mm	598.8 min	460.0 min	264.6 min
100 mm	965.4 min	742.0 min	417.9 min

Table 3.8. Total heat transfer times for discharging process with liquid Therminol/VP-1.

Diameter	NaNO$_3$	NaCl-MgCl$_2$ Eutectic	MgCl$_2$
10 mm	2.2 min	1.8 min	1.1 min
25 mm	16.2 min	13.1 min	6.7 min
50 mm	68.0 min	54.2 min	26.8 min
75 mm	153.4 min	122.5 min	60.2 min
100 mm	272.2 min	217.8 min	106.5 min

3.4 Conclusions

Based on the one-dimensional heat transfer simulations for the infinitely long cylindrical EPCM capsules, the heat transfer times are longer for larger sizes of capsules as expected. The heat transfer process is much better when using liquid as HTF instead of gas. Moreover, the temperature difference between EPCM capsule and HTF affects the heat transfer process related to the energy input for melting and energy out for

solidifying. A larger temperature difference between EPCM and HTF would shorten the total heat transfer times for phase change of PCM in the capsule. Properties of PCMs, such as density, heat capacity, thermal conductivity, latent heat, etc., can also affect the total energy storage/retrieval times in capsules. Higher heat capacity and higher latent heat can increase the total heat transfer times while higher thermal conductivity could shorten the heat transfer times.

CHAPTER 4

TWO-DIMENSIONAL HEAT TRANSFER ANALYSIS

During charging and discharging processes, the heat transfer process inside EPCM capsule is not symmetric because of the none uniform heat transfer coefficient along the surface of the capsule, the gravity effect, the natural convection in the molten PCM and the presence of void space in the PCM. Therefore, two-dimensional heat transfer simulations would be more suitable to represent the heat transfer process inside the capsule.

Sodium nitrate, $NaNO_3$, is used as phase change material. $NaNO_3$ has relatively high melting point, 308 $^{\circ}$C, and high latent heat of fusion, 162.5 kJ/kg, which makes it a good candidate PCM for a high temperature TES. The wall thickness of the encapsulation shell is 1.5875 mm (1/16 inch). The heat transfer fluid temperature range is between 250 $^{\circ}$C to 500 $^{\circ}$C. The HTF flows from the top of the cylinder to the bottom for a charging process while it flows from the bottom to the top (in opposite direction) for a discharging process.

4.1 Mathematical Modeling and Numerical Solutions

For a 75 mm diameter cylindrical $NaNO_3$ EPCM capsule, the average Rayleigh number, $Ra = g\beta \Delta T R_d^3/(\alpha_{PCM}\upsilon)$, is expected to be around 10^7 in the liquid state $NaNO_3$. Here, g is the magnitude of the gravitational acceleration; β is the thermal expansion coefficient of liquid PCM; ΔT is the representative temperature difference; R_d is the difference between outer radius and inner radius in annulus; υ and α_{PCM} are the kinematic viscosity and the

thermal diffusivity of the liquid PCM, respectively. Since the average Ra is relatively small ($Ra < 10^9$, smaller than the critical Rayleigh number for the onset of the natural convection [19]), the effect of natural convection in the molten $NaNO_3$ PCM on the melting/solidification process is expected to be negligible, but such effect should still be investigated in the next chapter.

Furthermore, there is void space in the real EPCM capsule for the volume change of PCM due to the phase change. Heat transfer analysis including the void space in the EPCM will also be presented in the next chapter.

Following assumptions are adopted for the two-dimensional simulations presented in this chapter.

- PCM is pure substance (no moisture or impurities) so the sub-cooling effects are negligible.
- The capsule and HTF are incompressible.
- Physical properties of PCM are constant for each phase.
- The buoyancy-driven convection in the molten PCM is negligible.
- No volume change due to the phase change of the PCM.

The front-tracking method or the enthalpy method can be employed to simulate the thermal energy storage to EPCM effectively. Front-tracking method determines the location of liquid/solid interface in PCM during melting/solidification process and it is more accurate to simulate the heat transfer in a single EPCM capsule. The results predicted by the front-tracking and the enthalpy methods were compared for a

horizontally placed cylinder in a cross flow [43]. The enthalpy method using ANSYS-FLUENT was conducted by a Ph.D. candidate, Ali F. Elmozughi, in our group. The simulation results predicted by these methods agree well [43].

Numerical simulations using the front tracking method were conducted for a horizontally and a vertically placed cylinder against the flowing heat transfer fluid around the capsule, as shown in Figure 4.1(a), (b).
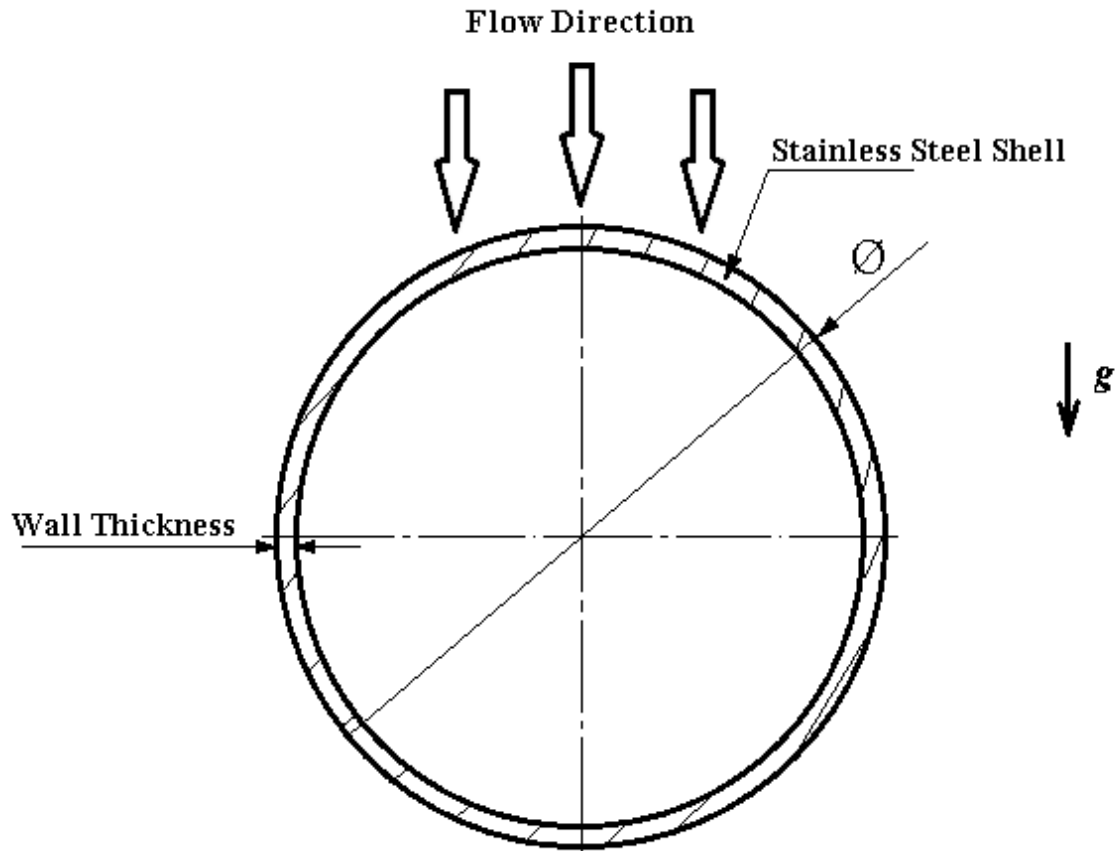
(a) Cross flow arrangement
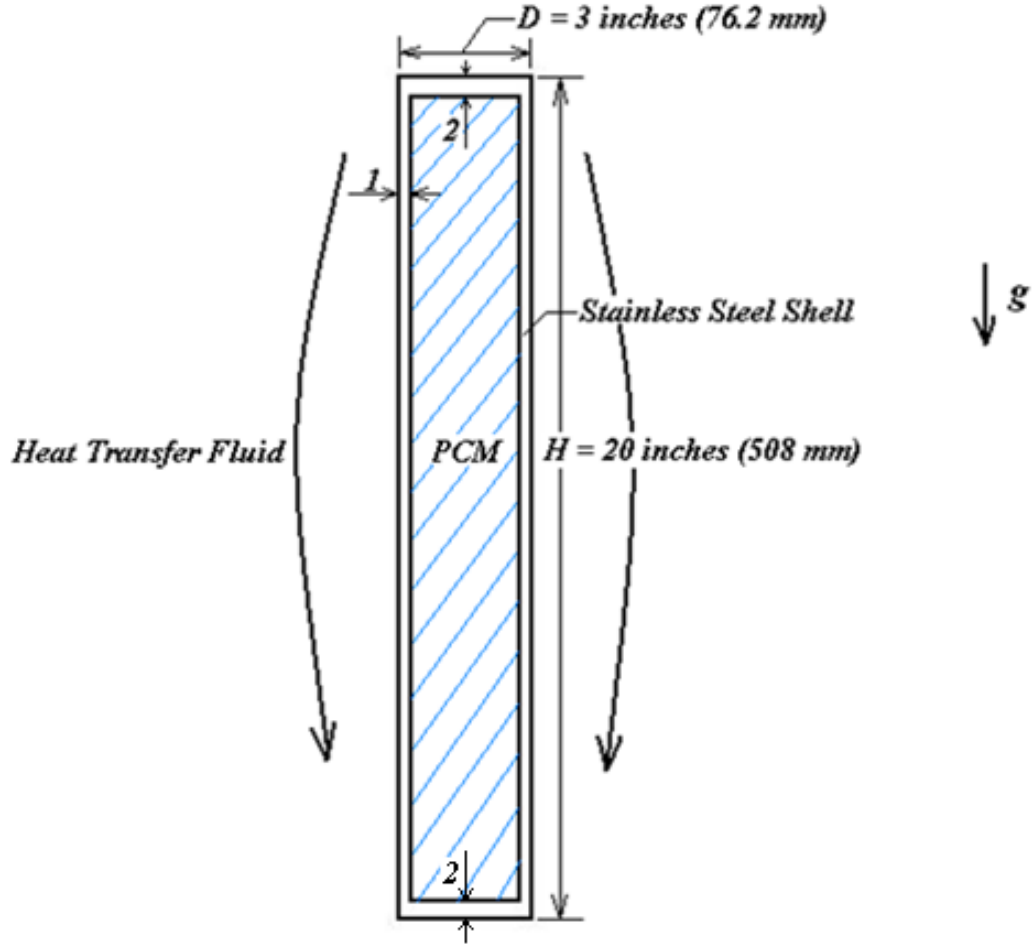
1- Wall Thickness = 1/16 inch (1.5875 mm)
2- Top & Bottom Shell Thickness = 0.4 inch (10.16 mm)

(b) Axial flow arrangement

Figure 4.1. Schematic of the EPCM capsule or tube

The equation governing the transient heat transfer in an EPCM during a thermal storage process is of the form:

$$\rho_j c_j \frac{\partial T_j}{\partial t} = k_j \left[\frac{1}{r} \frac{\partial}{\partial r} \left(r \frac{\partial T_j}{\partial r} \right) + \frac{1}{r^2} \frac{\partial^2 T_j}{\partial \varphi^2} + \frac{\partial^2 T_j}{\partial z^2} \right] \qquad (4.1)$$

where ρ_j is the density; c_j is the specific heat; k_j is thermal conductivity; T_j is the temperature distribution in each layer; r is the radial distance; φ is the angle in angular direction of cylinder; z is the axial coordinate; t is the time. The subscript j equals 1, 2, or 3 for the thin layered shell, the liquid and the solid phases of the PCM, respectively.

The boundary conditions imposed on the temperature field in each layer are

$$-k_1 \frac{\partial T_1}{\partial n} = h(T_1 - T_f) \text{ , at the outer surface} \tag{4.2}$$

$$-k_1 \frac{\partial T_1}{\partial n} = -k_2 \frac{\partial T_2}{\partial n} \text{ , and } T_1 = T_2, \text{ at the interface between the PCM and the shell}$$

$$\tag{4.3}$$

$$-k_2 \frac{\partial T_2}{\partial n} = -k_3 \frac{\partial T_3}{\partial n} + L\rho_2 V_n \text{ , } T_2 = T_3 = T_m, \text{ at the liquid/solid interface in the PCM}$$

$$\tag{4.4}$$

$$T_{centroid} = \frac{1}{N} \Sigma_i^N T_i \text{ , at the centroid of the solid/liquid state of the PCM for a horizontally}$$

placed cylinder $\tag{4.5a}$

$$\frac{\partial T}{\partial r} = 0 \text{ , at } r = 0 \text{ for a vertically placed cylinder} \tag{4.5b}$$

Here h is the local convective heat transfer coefficient; n is the unit normal direction on

the surface; V_n is the speed of the interface movement in the normal direction ($V_n = \frac{\partial s_n}{\partial t}$),

s_n is the displacement of the liquid/solid interface in the direction normal to the interface;

$T_{centroid}$ is the temperature at the centroid of the PCM; T_i is the temperature at nodes

around the centroid and N is the total number of nodal points in the angular direction for

a horizontally placed cylinder. Initially, the temperature is uniform ($T = T_o$) in EPCM.

Equation (4.4) is the energy balance equation applied at the liquid/solid interface of

PCM, which predicts the rate of the liquid/solid interface movement.

For a horizontally placed cylinder inside the thermocline, the fluid temperature T_f is

considered to be constant and the convective heat transfer coefficient, h, varies in the

angular direction around the cylinder and is determined by a local Nusselt number, Nu_φ.

$$h = \frac{Nu_\varphi \cdot k_f}{D} \tag{4.6}$$

Here, D is the outer diameter of EPCM capsule and k_f is the thermal conductivity of the heat transfer fluid. The local Nusselt number was found from references [44,45] based on the Reynolds number of HTF, $Re = \rho_f U D / \mu_f$. For the thermocline including 76.2 mm diameter EPCM capsules and the mass flow rate of air HTF ranging between 0.01 kg/s and 0.05 kg/s, the superficial velocity of air HTF in the thermocline, U, is determined. For liquid Therminol/VP-1 HTF, the superficial velocity of liquid in the thermocline is approximately ten times smaller than that of air. Even though the liquid flow velocity is smaller than the air flow velocity, Reynolds number for liquid is still much larger than that for air because of higher density, higher heat capacity and higher viscosity of liquid. ρ_f and μ_f are the density and viscosity of the HTF, respectively.

For a vertically placed cylinder, the direction of the HTF flow is in the same direction as the gravitational acceleration during a charging process while it is in the opposite direction of the gravity during a discharging process, as depicted in Figure 4.1(b). The heat transfer coefficient, h, is determined by the Nusselt number, Nu. For laminar heat transfer flow, Nusselt number is estimated based on fully developed laminar flow in a circular tube annulus [19]. For turbulent heat transfer flow ($Re > 10,000$), Nusselt number is evaluated with the Dittus-Boelter equation by using the hydraulic diameter, $D_h = D_o - D$, for a concentric tube annulus [19]. Here, D_o is the diameter of the channel. For the charging process, the temperature of the heat transfer fluid is kept constant at the top of the rod and it varies in the axial direction. The thermal energy balance for the heat transfer fluid is used to predict the temperature distribution of HTF, $T_f(z,t)$, as

$$\frac{\dot{m}c_f}{V_a}\frac{\partial T_f}{\partial t} = \dot{m}c_f\frac{\partial T_f}{\partial z} - \pi Dh(T_f - T_s) \tag{4.7}$$

where $\dot{m}$ is the mass flow rate of the heat transfer fluid; c_f is the specific heat of fluid; V_a is the average velocity of the HTF; and T_s (z,t) is the surface temperature of the EPCM capsule.

Finite difference method is employed to discretize equations (4.1)-(4.7). Resulting nonlinear coupled equations are solved using Jacobi iterations. The simulations are conducted by dimensionless variables using radius, axial coordinate and time measured in units of R_1, H_z and R_2^2/α_2, respectively. Here, α_2 is the thermal diffusivity of liquid phase of PCM; R_1 is the outer radius of the capsule; H_z is the height of cylindrical capsule or tube; R_2 is the radius of PCM. Temperature in each layer is normalized by $\theta_j = (T_j - T_o)/(T_f - T_o)$. The non-dimensional governing equation becomes:

$$\frac{\alpha_2 R_{12}^2}{\alpha_j}\cdot\frac{\partial\theta_j}{\partial\tau} = \frac{1}{R}\cdot\frac{\partial\theta_j}{\partial R} + \frac{\partial^2\theta_j}{\partial R^2} + \frac{1}{R^2}\frac{\partial^2\theta_j}{\partial\varphi^2} + \frac{R_1^2}{H_z^2}\frac{\partial^2\theta_j}{\partial Z^2} \tag{4.8}$$

where Z is dimensionless axial coordinate.

Non-dimensional forms of the boundary conditions are:

$$-k_1\frac{\partial\theta_1}{\partial n} = h(\theta_1 - 1) \text{ , at the outer surface of the capsule} \tag{4.9}$$

$$-k_1\frac{\partial\theta_1}{\partial n} = -k_2\frac{\partial\theta_2}{\partial n} \text{ , at the shell/PCM interface} \tag{4.10}$$

$$-k_2\frac{\partial\theta_2}{\partial n} = -k_3\frac{\partial\theta_3}{\partial n} + \frac{L\rho_2\alpha_2 R_1}{R_2^2(T_f-T_o)}\cdot\frac{\partial S_n(\tau)}{\partial\tau} \text{ , at the liquid/solid interface in the PCM}$$

$$\tag{4.11}$$

$\theta_{centroid} = \frac{1}{N}\sum_i \theta_i$, at the centroid of the solid/liquid state of the PCM for a horizontally placed cylinder $\qquad$ (4.12a)

$\frac{\partial \theta}{\partial R} = 0$, at $R = 0$ for a vertically placed cylinder $\qquad$ (4.12b)

where $S_n(\tau)$ is the normalized displacement of the liquid/solid interface in the normal direction. For a charging process, the normalized initial capsule temperature is $\theta_j(R, \varphi, Z, 0) = 0$ while $\theta_j(R, \varphi, Z, 0) = 1$ for a discharging process.

4.2 Two-Dimensional Heat Transfer Analysis without Gravity Effect in Solid PCM

76.2 mm diameter $NaNO_3$ EPCM capsule in a cross flow arrangement is considered. The melting point of $NaNO_3$ is 308 $^{\circ}$C (normalized melting point: 0.232). The heat transfer coefficient around the capsule is determined by the local Nusselt number according to the Reynolds number, as described previously. Figure 4.2 is an example of the distribution of the local Nusselt number around 76.2 mm diameter EPCM capsule in the cross flow arrangement using air as HTF.
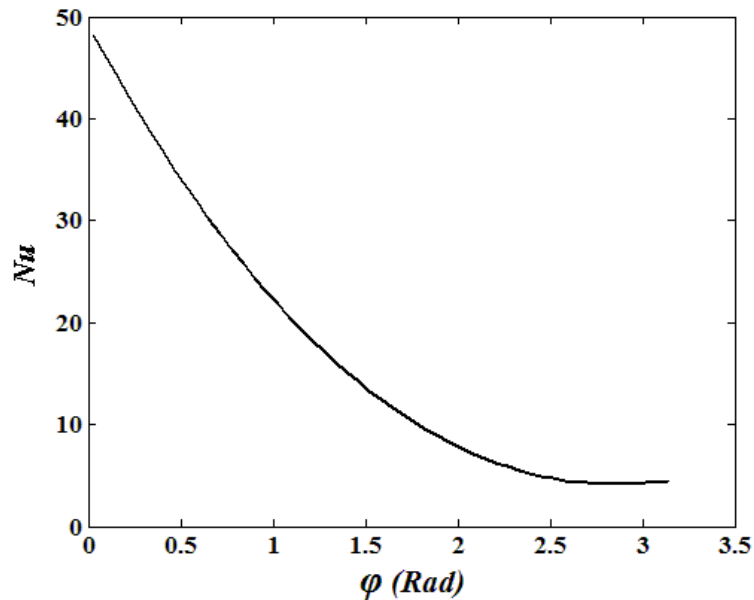

Figure 4.2. The distribution of local Nusselt number around the capsule

The spatial and the temporal convergence of the front-tracking method are established. Table 4.1 illustrates the spatial convergence results with dimensionless time step, $\Delta\tau = 0.00001$. Table 4.2 displays results of the temporal convergence test. It is concluded as a result of these convergence tests that 101×56 (angular×radial) numbers of nodes and the time step of 0.00001 are sufficient to achieve the spatial convergence and the temporal convergence for the front-tracking method employed here.

Table 4.1. Total melting times for a 76.2 mm diameter NaNO$_3$ capsule using liquid Therminol/VP-1 as HTF (spatial convergence).

Number of nodes: (angular × radial)	Melting times (Seconds)
31×106	2939
51×106	2939
101×106	2939
101×56	2941

Table 4.2. Total melting times for a 76.2 mm diameter NaNO$_3$ capsule using liquid Therminol/VP-1 as HTF (temporal convergence).

Number of nodes: (angular × radial)	Dimensionless time step, $\Delta\tau$	Melting times (Seconds)
101×106	0.00001	2939
	0.000005	2939

Figure 4.3(a) shows the location of the propagating liquid/solid interface at various times for 76.2 mm diameter NaNO$_3$ EPCM capsule during a charging process using air as HTF. The front propagates radially inward as the melting process progresses, as displayed in Figure 4.3(a). Figure 4.3(b) illustrates the normalized isotherms during a charging process at 99 minutes from the melting has started. There is significant variation of the temperature in the molten PCM. The temperature near the top of the capsule is greater than the lower part of the capsule, as displayed in the Figure 4.3(b). Such variation is the result of the distribution of the local heat transfer coefficient. The value of heat transfer coefficient is highest at the top of the cylinder as the HTF flows from the top to the

bottom of the capsule. The temperature gradient in liquid PCM is much larger while the temperature in solid PCM remains slightly below the melting point.
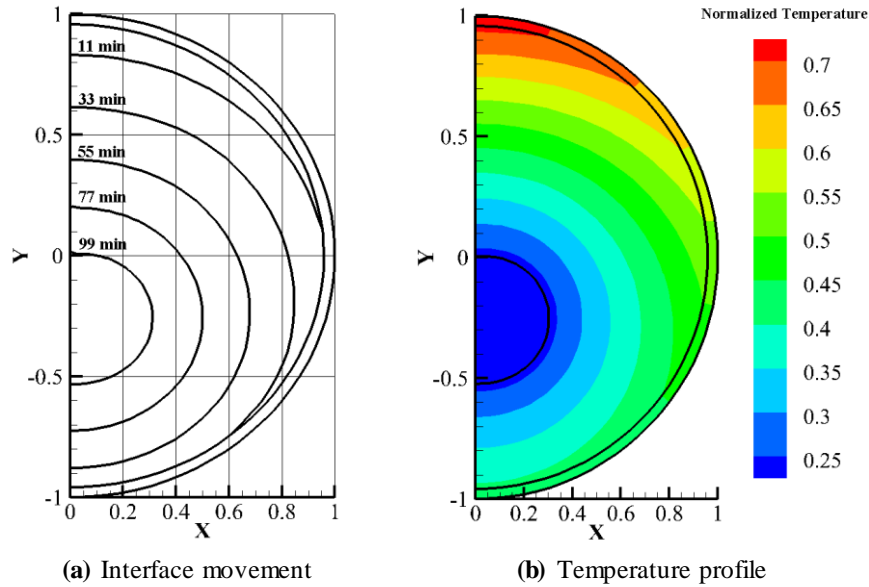

(a) Interface movement   **(b)** Temperature profile

Figure 4.3. a) The location of the liquid/solid interface in PCM, b) Isotherms at 99 minutes into the melting process

Figure 4.4(a) displays the location of the liquid/solid interface in a 76.2 mm diameter $NaNO_3$ capsule during a solidification process using air as HTF. The liquid/solid interface propagates radially inward. Since the cooling heat transfer fluid flows from the bottom to the top, the bottom region of PCM solidifies faster. It is also noted that HTF temperature (250 $^{\circ}$C) is closer to the melting/freezing temperature of $NaNO_3$ (308 $^{\circ}$C). Thus, the solidification process is slower compared to the melting process in the $NaNO_3$ capsule. It takes more than 5 hours to complete the solidification process. Liquid PCM region is denoted as the region inside the liquid/solid interface curve while the solid state PCM is at the outside of the liquid/solid interface. Figure 4.4(b) shows the normalized isotherms 5 hours into the solidification process. At this moment, most of PCM is solidified.
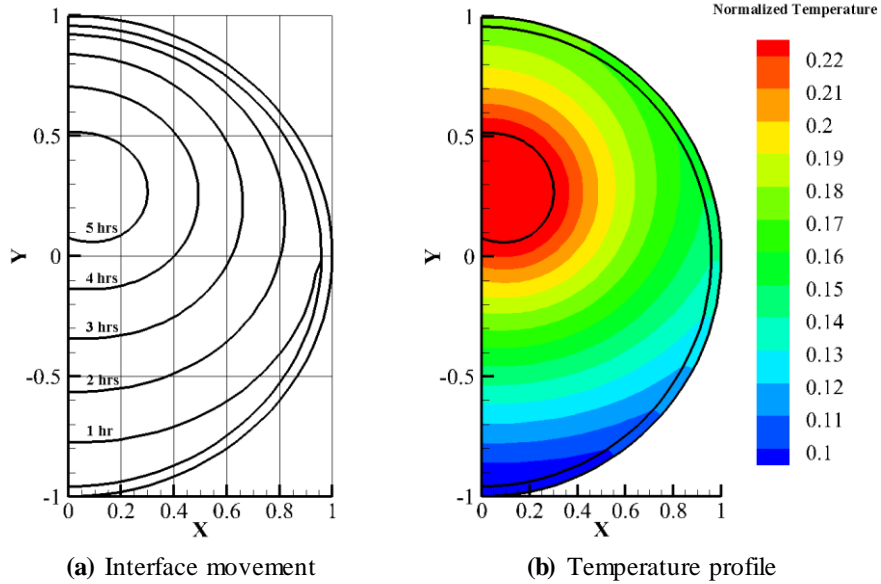
(a) Interface movement (b) Temperature profile

Figure 4.4. a) The location of the liquid/solid interface in PCM, b) Isotherms at 5 hours into the solidification process

Figure 4.5 displays the energy storage/retrieval from a 76.2 mm diameter $NaNO_3$-stainless steel EPCM capsule using air as HTF. From the graphs, it is noticed that the energy storage time is shorter than the energy retrieval time because the melting point of $NaNO_3$ is closer to the lower end of HTF temperature during a discharging process. The smaller temperature different between EPCM and HTF would slow down the heat transfer rate for the capsule.
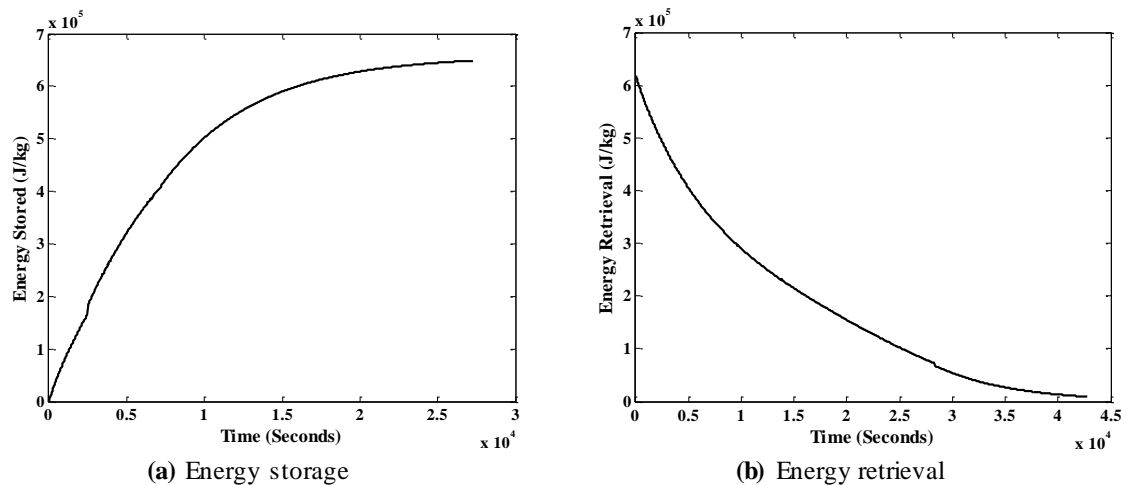

(a) Energy storage (b) Energy retrieval

Figure 4.5. Energy storage/retrieval from EPCM capsule

4.3 Two-Dimensional Heat Transfer Analysis Considering Gravity Effect in Solid PCM

Numerical simulations were conducted for a horizontally placed cylinder in a cross flow arrangement and a vertically placed cylinder in an axial flow arrangement. For these simulations, the heat transfer coefficient is estimated based on the Nusselt number as described previously. Figure 4.6 displays the location of the interface predicted by a front tracking method at various times for a 76.2 mm diameter $NaNO_3$ EPCM capsule during a melting process using air as HTF in a cross flow arrangement. The effect of the gravity in the EPCM capsule is included. Since the density of solid PCM is greater than that of liquid PCM, the solid PCM sinks to the bottom of the capsule during the melting process. Since the rate of the heat transfer is higher near the front stagnation point of cylinder, the solid/liquid interface is first formed near the top region and it propagates inwards as the melting progresses. The solid phase of the PCM shrinks to a small region near the bottom of the capsule. It takes about 98.0 minutes for the melting process to be completed.

Figures 4.7(a), 4.7(b) and 4.7(c) display the isotherms for a 76.2 mm diameter $NaNO_3$ capsule at 30 minutes, 60 minutes and 90 minutes after the melting process has started, respectively. Here, the normalized melting point of $NaNO_3$ is 0.232. Air is used as a HTF for these simulations. The solid black curve inside the capsule represents the location of liquid/solid interface in PCM. It is solid PCM inside the curve while it is liquid PCM outside the curve. The solid $NaNO_3$ begins to melt at 37 minutes after the charging process started. The solid phase of PCM always sinks to the bottom of the capsule due to the gravity effect. The high temperature gradient exists inside the liquid region while the temperature varies slightly in the solid region, as shown in Figure 4.7. At later stage of

the melting process, the temperature inside the solid PCM becomes nearly uniform at just below the melting temperature of the PCM while the temperature variation in the molten PCM becomes greater, as displayed in Figure 4.7(c).
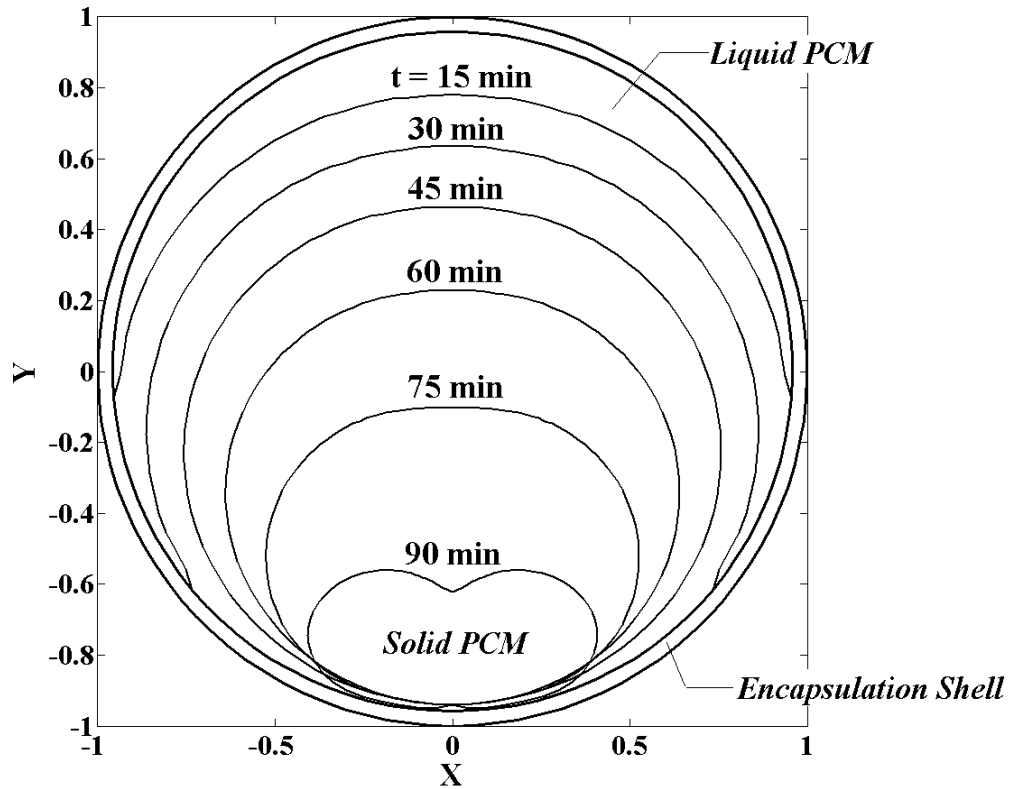

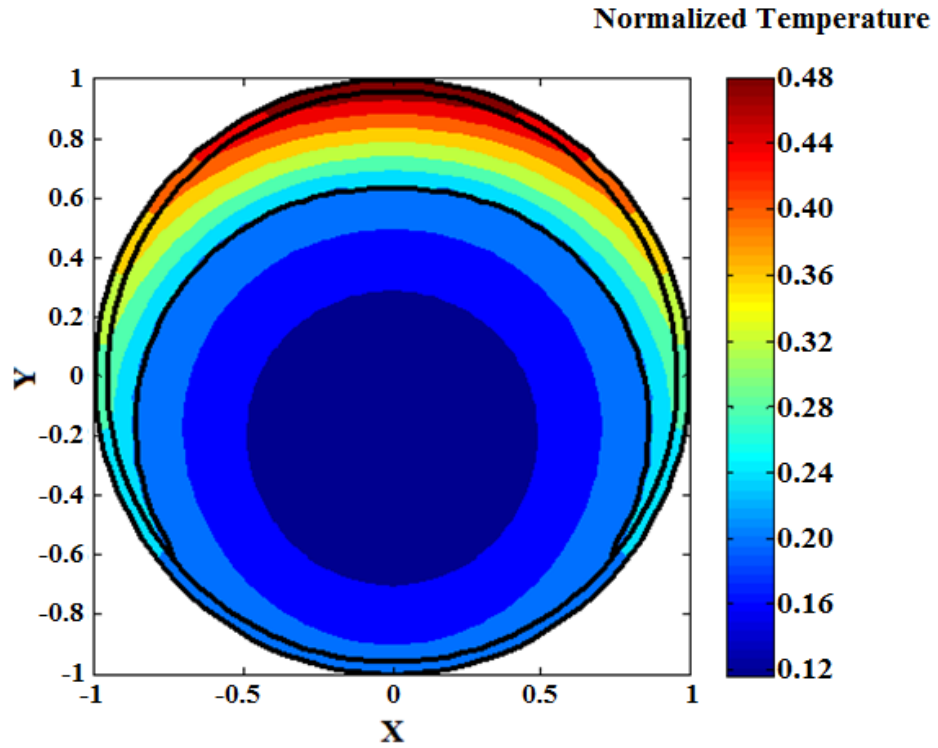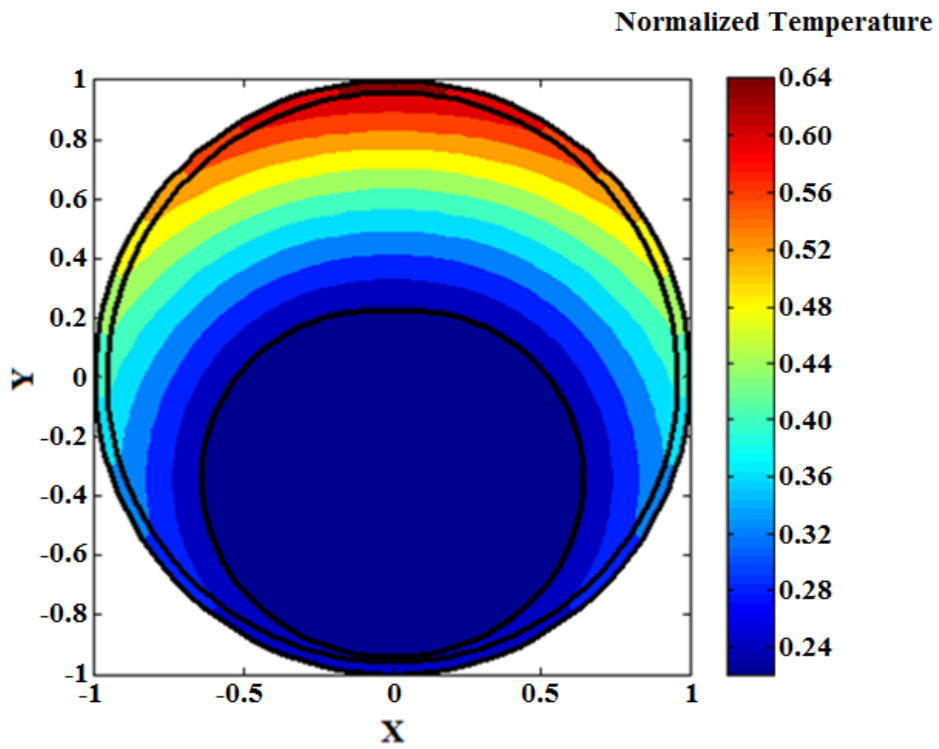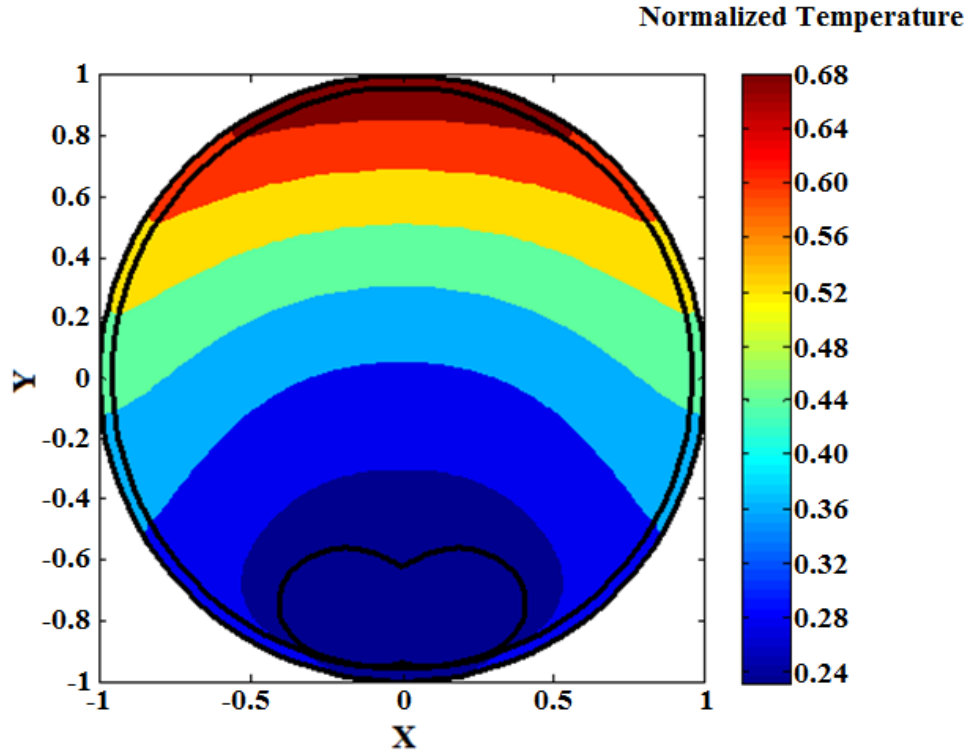
Figure 4.6. Location of the liquid/solid interface during melting process for a cross flow arrangement

(a) At 30 minutes (Dimensionless time or Fourier number of 0.2)

(b) At 60 minutes (Dimensionless time or Fourier number of 0.4)

(c) At 90 minutes (Dimensionless time or Fourier number of 0.7)
Figure 4.7. Isotherms at a) 30 minutes, b) 60 minutes, c) 90 minutes into the melting process for a cross flow arrangement

For a vertically placed EPCM, the diameter of cylinder is 76.2 mm and the height of cylinder is 508 mm. The temperature of HTF is maintained at 500 $^{\circ}$C at the top of the capsule during a charging process. 5,050 nodes (axial $\times$ radial = 101 $\times$ 50) with dimensionless time step, $\Delta\tau$ = 0.00001, are used for the simulations. Figure 4.8 shows the location of the radially symmetric liquid/solid interface at various times during a charging process using air as HTF. Region outside the liquid/solid interface is occupied by the liquid phase of $NaNO_3$ while the region inside the interface is occupied by the solid phase. Since the density of the solid state PCM is higher than that of the liquid state PCM, the solid $NaNO_3$ always sinks to the bottom of the capsule, as displayed in Figure 4.8. It takes about 69.7 minutes for the $NaNO_3$ PCM to melt completely.
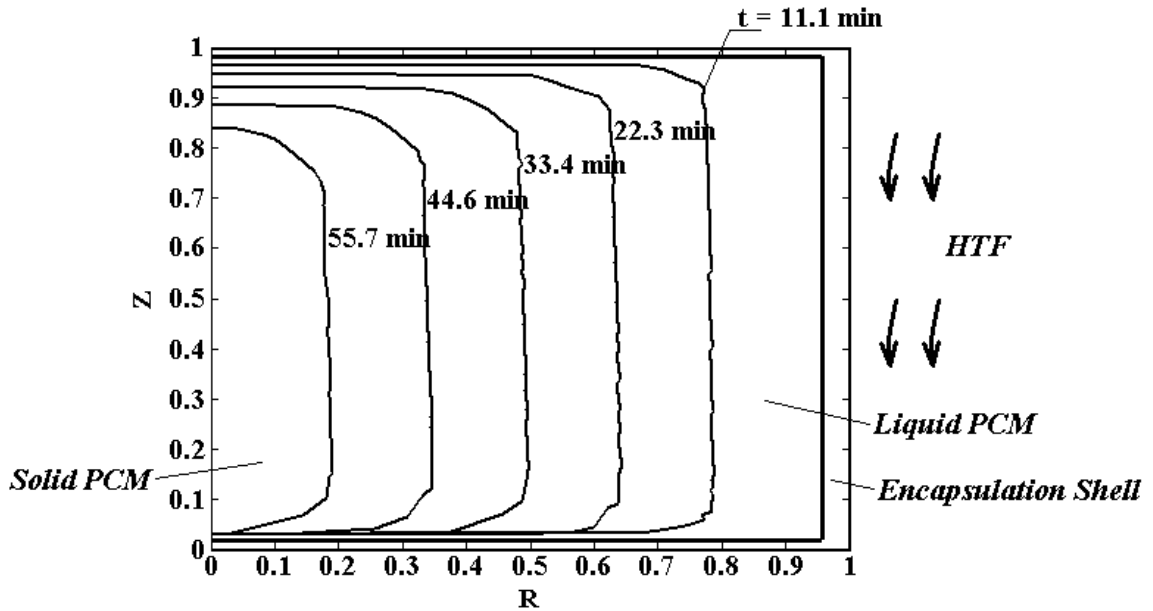
Figure 4.8. Location of the liquid/solid interface in PCM at various times during charging process

Figure 4.9 represents the liquid/solid interface propagation during a discharging process in a vertically placed cylinder in an axial flow arrangement with air as HTF. The region outside the liquid/solid interface is a solid state PCM while it is a liquid PCM inside the interface. Since the HTF flows from the bottom to the top of the cylinder and maintains at 250 $^{\circ}$C at the bottom during a discharging process, the bottom region of PCM solidifies slightly faster than that of the top region.
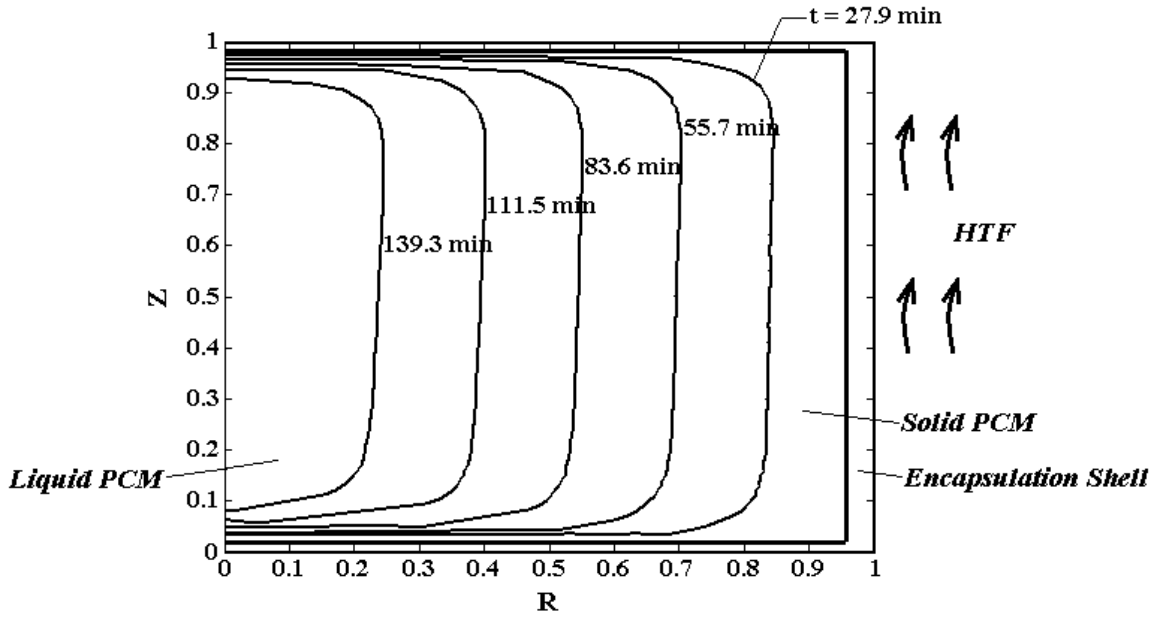
Figure 4.9. Location of the liquid/solid interface in PCM at various times during discharging process

Figure 4.10 displays the temperature profiles in the vertically placed $NaNO_3$ EPCM during a melting process (normalized melting point of $NaNO_3$: 0.232). The yellow curve inside the cylinder is the location of liquid/solid interface in PCM. The region is solid state PCM inside the curve and liquid state PCM outside the curve. The temperature in the liquid state PCM increases rapidly to HTF temperature while the temperature in the solid PCM maintains slightly below the melting point.
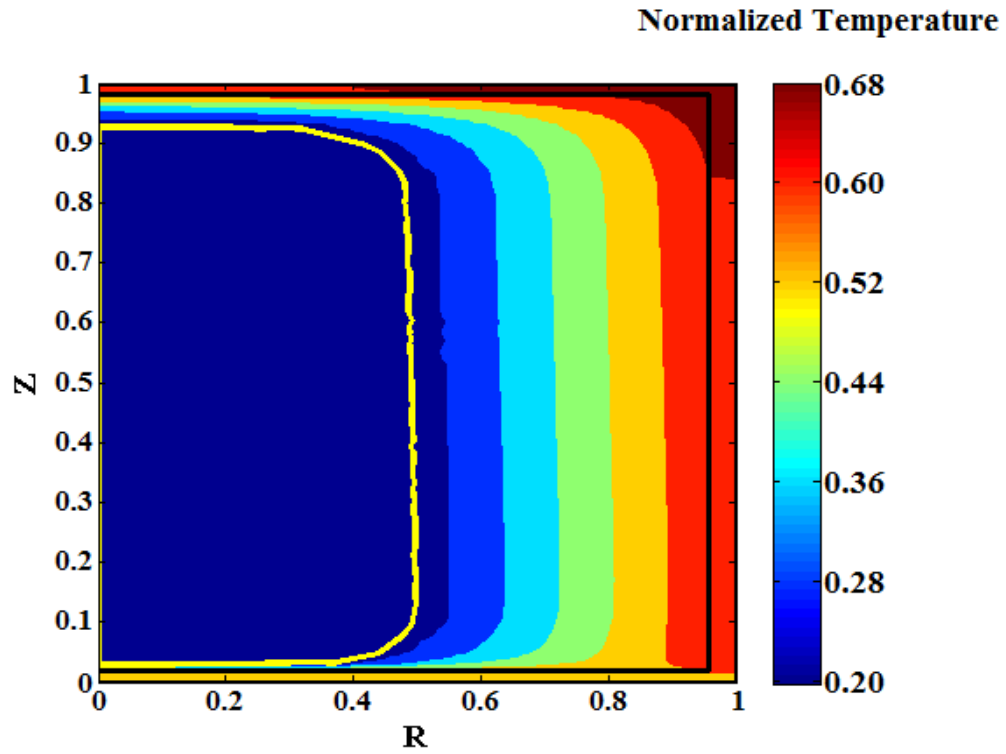
(a) At 33.4 minutes (Dimensionless time or Fourier number of 0.25)
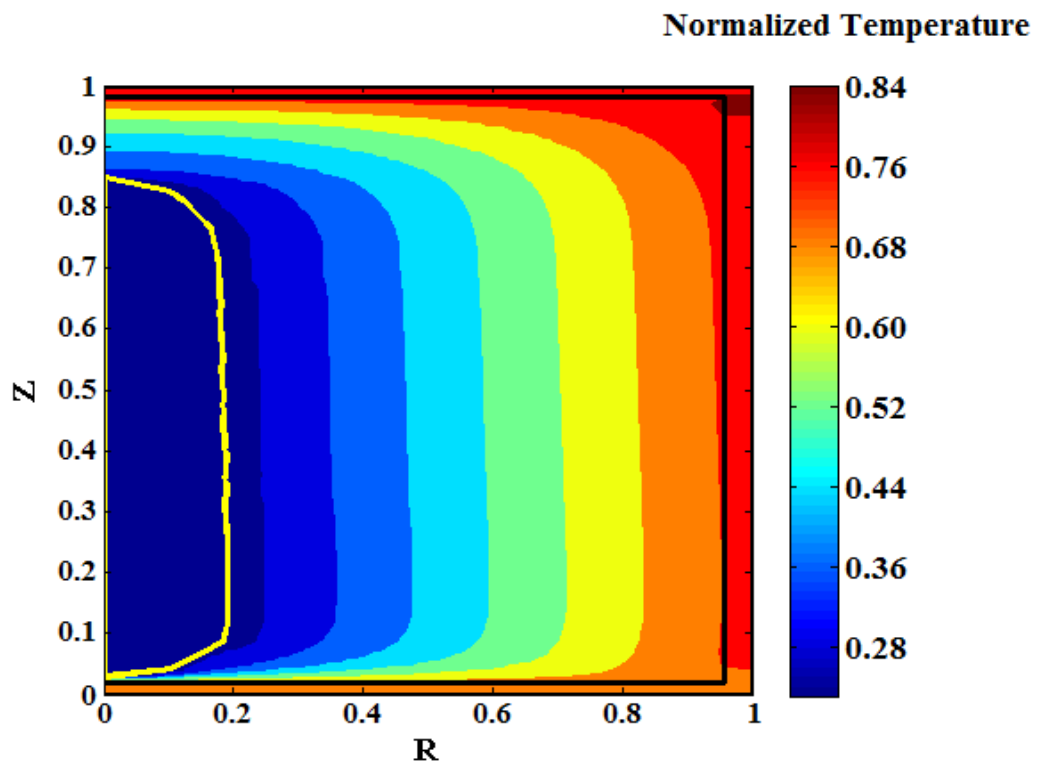
(b) At 55.7 minutes (Dimensionless time or Fourier number of 0.4)

Figure 4.10. Isotherms at a) 33.4 minutes, b) 55.7 minutes into the melting process for an axial flow arrangement

Table 4.3 illustrates the total charging times for three different sizes of $NaNO_3$ capsules in a cross flow arrangement with air and liquid Therminol/VP-1 as HTFs. For air, $Re = 410$ for 25.4 mm diameter capsule, 820 for 50.8 mm capsule and 1,230 for 76.2 mm capsule. For liquid Therminol/VP-1, $Re = 9,917$ for 25.4 mm capsule, 19,835 for 50.8 mm capsule and 29,752 for 76.2 mm capsule. The total heat transfer times are predicted using the front tracking approach by including the gravity effect inside the EPCM (letting the solid state of PCM sink to the bottom of the capsule). The charging times increases as the capsule diameter increases. Since the surface heat transfer dominates the rate of the thermal energy storage/retrieval into/out of the EPCM, the total heat transfer times is much shorter with the liquid heat transfer fluid compare to that of the gas heat transfer fluid. Furthermore, the gravity effect of the solid state PCM can also shorten the total energy storage times in the EPCM capsule. The results clearly show that the thermal energy module in the power generation and other large scale industrial thermal systems has to be designed properly by a careful consideration of the heat transfer from the HTF to the EPCM and the heat transfer inside the EPCM.

Table 4.3. Energy storage times for horizontally placed cylinder.

Diameter of Capsule	Air	Liquid Therminol/VP-1
25.4 mm (1 inch)	87.6 min	23.6 min
50.8 mm (2 inches)	264.0 min	94.2 min
76.2 mm (3 inches)	503.6 min	192.9 min

Table 4.4 displays the charging and the discharging times for a 76.2 mm diameter and 508 mm length of $NaNO_3$ EPCM rod in an axial flow arrangement with air and liquid Therminol/VP-1 as HTFs. The storage times in an axial flow arrangement are shorter than those in a cross flow arrangement. That is due to the fact that the nature of the flow around the tube strongly depends on the arrangement of the capsule against the flow

inside the channel. This is another illustration of the importance of the surface heat transfer during the thermal energy storage into the EPCM. It is also noted that the energy retrieval times are in general longer than the energy storage times since the heat transfer fluid temperature during the energy retrieval times is selected to be closer to the freezing temperature of the PCM. That results in a slower rate of the surface heat transfer for the EPCM.

Table 4.4. Heat transfer times for a vertically placed cylinder.
(for air, $Re = 58$; for liquid Therminol/VP-1, $Re = 17,082$)

	Air	Liquid Therminol/VP-1
Charging Process	202.7 min	107.9 min
Discharging Process	307.8 min	137.8 min

4.4 Conclusions

As expected, heat transfer times are longer for larger sizes of capsules. Using liquid as HTF would significantly shorten the total heat transfer times inside the capsule compared to air. Different HTF flow patterns could also affect the heat transfer process inside the EPCM capsule. From the simulations, the discharging times are longer than the charging times at current cases because the melting point of $NaNO_3$ (308 $^{\circ}$C) is much closer to the lower heat transfer fluid temperature (250 $^{\circ}$C).

Furthermore, the gravity effect could shorten the times for phase change process. Figure 4.11 compares the two situations for 76.2 mm diameter $NaNO_3$ capsule with air as HTF. When the gravity effect is not considered, the total melting times is 116.6 minutes (dimensionless time: $\tau = 0.87$) while the total melting time is only 98.0 minutes (dimensionless time: $\tau = 0.73$) as the gravity effect of solid PCM is considered in the capsule.
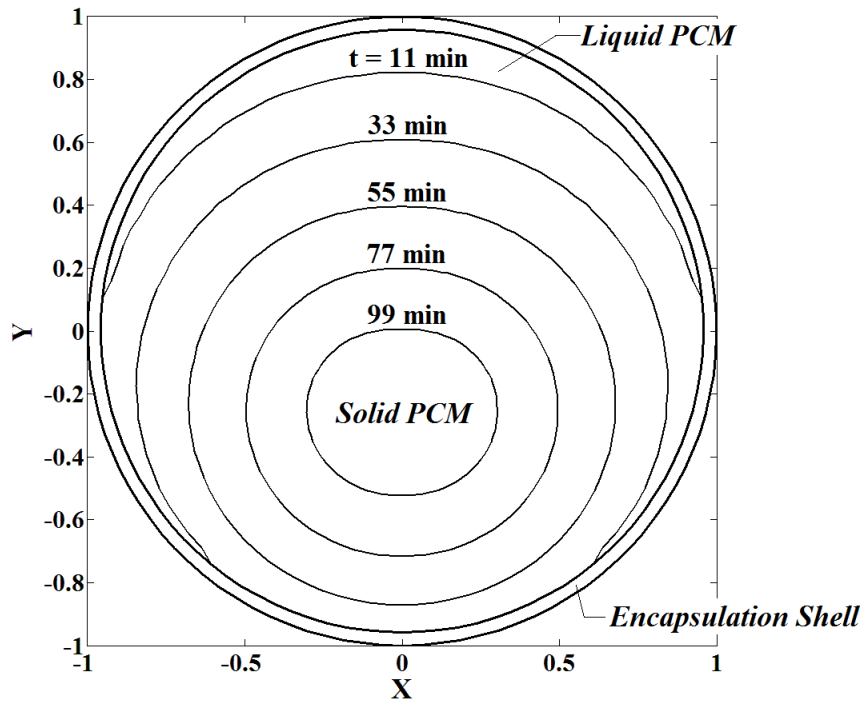
(a) Not considering gravity effect of solid PCM
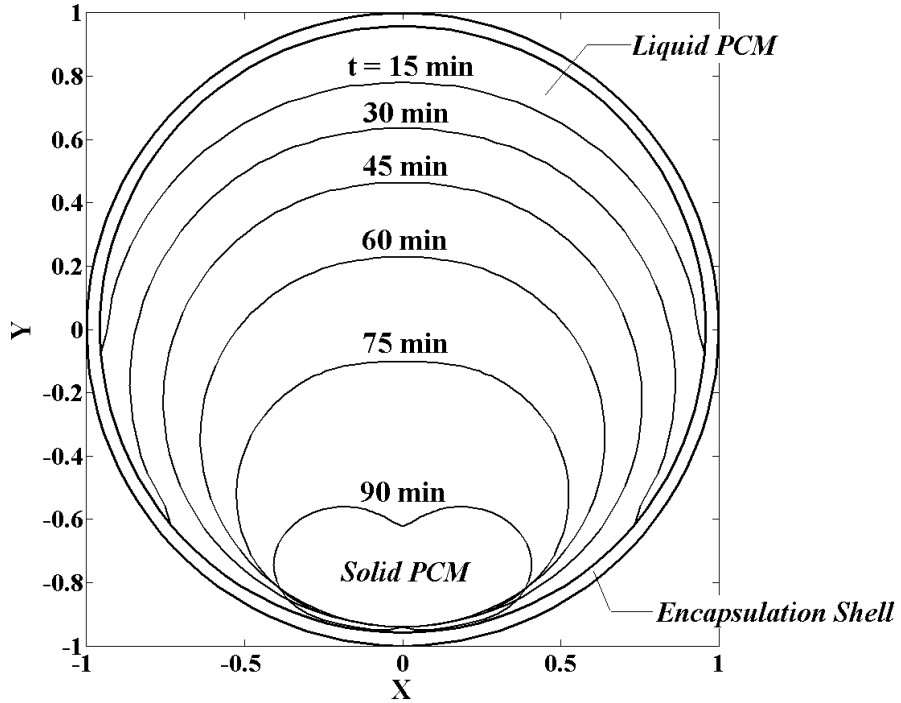
(b) Considering gravity effect of solid PCM

Figure 4.11. Compare the melting process between a) not considering the gravity effect and b) considering gravity effect of solid PCM in capsule

70

CHAPTER 5

BUOYANCY-DRIVEN CONVECTION IN MOLTEN PCM AND VOID SPACE IN EPCM CAPSULE

Presence of temperature gradient in the molten PCM results in a buoyancy-driven convection in the liquid state of PCM. The buoyancy-driven natural convection generated in the liquid phase of PCM would affect the interface growth and the temperature profiles in the PCM. The natural convection is expected to enhance the heat transfer in the phase change material and shortens the energy storage/retrieval times. The effect of the natural convection on the dynamics of the interface and the heat transfer characteristics of the EPCM are illustrated here. It is also studied here the effect of void space in the EPCM to account for the volume change by the phase change. Proper void space should be provided inside the capsule for the volume expansion of material during phase change process. Thus, the model involving volume expansion of PCM during a charging process is also illustrated in this chapter.

Sodium nitrate (the melting temperature of 308 $^{\circ}$C) is considered as the PCM here for the simulations. Stainless steel is selected as encapsulation shell with 1.5875 mm (1/16 inch) thickness. The outer diameter of EPCM capsule is 76.2 mm (3 inches). The heat transfer fluid temperature is 500 $^{\circ}$C for a charging process. And the fluid flows from the top of the capsule to the bottom.

5.1 Buoyancy-Driven Convection in Molten PCM

5.1.1 Mathematical Modeling

The equations governing the velocity and temperature fields are [46]:

Continuity:

$$\frac{\partial \rho}{\partial t} + \nabla(\rho V) = 0 \qquad\qquad (5.1)$$

Momentum:

$$\frac{\partial(\rho V)}{\partial t} + \nabla(\rho V \cdot V) = -\nabla p + \nabla \cdot T_{stress} + f \qquad\qquad (5.2)$$

Energy:

$$\frac{\partial E}{\partial t} + V \cdot \nabla E = -\nabla \cdot q - p(\nabla \cdot V) - (\tau:\nabla V) \qquad\qquad (5.3)$$

where $V = v_r \vec{r} + v_\varphi \vec{\varphi}$ is the melt flow velocity, v_r is the radial velocity component, v_φ is the angular velocity component, $\vec{r}$ is the unit vector in radial direction, $\vec{\varphi}$ is the unit vector in angular direction; ρ is the density in the molten PCM; p is the pressure inside the capsule; T_{stress} is the stress tensor; f is the body force; E is the energy of the liquid PCM per unit volume; q is heat flux; $-(\tau:\nabla V)$ is the irreversible rate of energy increase per unit volume of liquid PCM by viscous dissipation.

The equations (5.1)-(5.3) are simplified using the following assumptions:

- PCM is pure substance (no moisture or impurities) so the sub-cooling effects are negligible.
- The capsule is horizontally placed in a cross flow.
- It is assumed to be a long cylinder. It just considers the heat diffusion in the radial and the angular directions, and no heat diffusion in the axial direction.
- The capsule is incompressible.

- It is assumed that density in solid state PCM is constant, but density in liquid state PCM varies with temperature. The liquid phase density is different from the solid phase density.

- Gravity effect in solid PCM is considered.

- Boussinesq approximation is adopted.

- No volume expansion due to the phase change of the PCM.

Thus, the continuity, the radial and the angular momentum, and the energy equations could be rewritten in equations (5.4), (5.5), (5.6), and (5.7), respectively. These equations describe the velocity and temperature fields in the PCM. The energy equation (5.7) is an extension of the unsteady heat diffusion equation used in the Chapter 4 for the two-dimensional heat transfer. The governing equations (5.1)-(5.3) become:

Continuity:

$$\frac{1}{r}\frac{\partial}{\partial r}(rv_r) + \frac{1}{r}\frac{\partial v_\varphi}{\partial \varphi} = 0 \tag{5.4}$$

Radial Momentum:

$$\frac{\partial v_r}{\partial t} + v_r \frac{\partial v_r}{\partial r} + \frac{v_\varphi}{r}\frac{\partial v_r}{\partial \varphi} - \frac{v_\varphi^2}{r} = -\frac{1}{\rho_R}\frac{\partial p}{\partial r} + \nu\left[\frac{1}{r}\frac{\partial}{\partial r}\left(r\frac{\partial v_r}{\partial r}\right) - \frac{v_r}{r^2} + \frac{1}{r^2}\frac{\partial^2 v_r}{\partial \varphi^2} - \frac{2}{r^2}\frac{\partial v_\varphi}{\partial \varphi}\right] + \frac{\rho}{\rho_R}g_r$$

$$\tag{5.5}$$

Angular Momentum:

$$\frac{\partial v_\varphi}{\partial t} + v_r \frac{\partial v_\varphi}{\partial r} + \frac{v_\varphi}{r}\frac{\partial v_\varphi}{\partial \varphi} + \frac{v_r v_\varphi}{r} = -\frac{1}{\rho_R r}\frac{\partial p}{\partial \varphi} + \nu\left[\frac{1}{r}\frac{\partial}{\partial r}\left(r\frac{\partial v_\varphi}{\partial r}\right) - \frac{v_\varphi}{r^2} + \frac{1}{r^2}\frac{\partial^2 v_\varphi}{\partial \varphi^2} + \frac{2}{r^2}\frac{\partial v_r}{\partial \varphi}\right] + \frac{\rho}{\rho_R}g_\varphi$$

$$\tag{5.6}$$

Energy:

$$\rho_R c\left(\frac{\partial T}{\partial t} + v_r \frac{\partial T}{\partial r} + \frac{v_\varphi}{r}\frac{\partial T}{\partial \varphi}\right) = k\left[\frac{1}{r}\frac{\partial}{\partial r}\left(r\frac{\partial T}{\partial r}\right) + \frac{1}{r^2}\frac{\partial^2 T}{\partial \varphi^2}\right] \tag{5.7}$$

where g_r is the radial accelerate gravity component; g_φ is the angular accelerate gravity component; T is the temperature; ρ is the density of molten PCM; ρ_R is the reference density (the molten PCM density at its melting temperature); c is the specific heat of molten PCM; k is the thermal conductivity of molten PCM; ν is the kinematic viscosity of the molten PCM. The body force in the momentum equations, $\frac{\rho}{\rho_R}g_r$ and $\frac{\rho}{\rho_R}g_\varphi$, is determined using the Boussinesq approximation.

The vorticity-stream formulation is applied with the definition of the stream function ψ,

$$v_r = \frac{1}{r}\frac{\partial \psi}{\partial \varphi} \tag{5.8}$$

$$v_\varphi = -\frac{\partial \psi}{\partial r} \tag{5.9}$$

and the definition of the axial component of the vorticity ζ.

$$\zeta = |\zeta| = |\nabla \times V| = \frac{1}{r}\frac{\partial}{\partial r}\left(rv_\varphi\right) - \frac{1}{r}\frac{\partial v_r}{\partial \varphi} = \frac{\partial v_\varphi}{\partial r} + \frac{v_\varphi}{r} - \frac{1}{r}\frac{\partial v_r}{\partial \varphi} \tag{5.10}$$

Equations (5.5) and (5.6) yield the non-pressure vorticity transport equation:

$$\frac{\partial \zeta}{\partial t} + \frac{1}{r}\frac{\partial \psi}{\partial \varphi}\frac{\partial \zeta}{\partial r} - \frac{1}{r}\frac{\partial \psi}{\partial r}\frac{\partial \zeta}{\partial \varphi} = \nu\left(\frac{\partial^2 \zeta}{\partial r^2} + \frac{1}{r}\frac{\partial \zeta}{\partial r} + \frac{1}{r^2}\frac{\partial^2 \zeta}{\partial \varphi^2}\right) + \frac{1}{r}\frac{\partial}{\partial r}\left(\frac{\rho}{\rho_R}rg_\varphi\right) - \frac{1}{r}\frac{\partial}{\partial \varphi}\left(\frac{\rho}{\rho_R}g_r\right)$$

$$\tag{5.11}$$

Combining equations (5.8), (5.9) and (5.10) yields poisson equation for the stream function ψ:

$$\nabla^2 \psi = -\zeta \tag{5.12}$$

The boundary conditions imposed on the capsule are as follows:

At the centroid of the solid or liquid PCM:

$$T_{centroid} = \frac{1}{N}\Sigma_i^N T_i \tag{5.13}$$

At the liquid/solid interface in PCM:

$$-k_{liq\_PCM}\frac{\partial T_{liq\_PCM}}{\partial n} = -k_{sol\_PCM}\frac{\partial T_{sol\_PCM}}{\partial n} + L\rho_{liq\_PCM}V_n \tag{5.14}$$

$$\rho_{liq\_PCM}(V_{liq} - V_n)\cdot\vec{n} = \rho_{sol\_PCM}(V_{sol} - V_n)\cdot\vec{n} \tag{5.15}$$

$$V\times\vec{n} = 0 \tag{5.16}$$

Here, equation (5.14) denotes the energy balance at the liquid/solid interface, equation (5.15) denotes the conservation of mass at the interface and equation (5.16) denotes the no-slip condition.

Here ρ_{liq_PCM} is the density of liquid phase PCM (ρ_R); ρ_{sol_PCM} is the density of solid phase PCM; V_{liq} is the velocity of liquid phase PCM near the interface, $V_{liq} = v_r\vec{r} + v_\varphi\vec{\varphi}$; V_{sol} is the velocity of solid phase PCM at the interface (assumed to be zero); k_{liq_PCM} is the thermal conductivity of liquid state PCM; k_{sol_PCM} is the thermal conductivity of solid state PCM; T_{liq_PCM} is the temperature of liquid state PCM at the interface; T_{sol_PCM} is the temperature of solid state PCM at the interface; n is the unit normal of the interface; V_n is the propagation speed of the interface in the direction normal to the interface.

Equations (5.15) and (5.16) can also be expressed in terms of the axial component of the vorticity and the stream function.

$$-\zeta = \frac{\partial^2\psi}{\partial r^2} + \frac{1}{r^3}\frac{\partial s}{\partial\varphi}\frac{\partial\psi}{\partial\varphi} + \frac{1}{r^2}\frac{\partial^2\psi}{\partial\varphi^2} \tag{5.17}$$

$$\frac{\partial^2 \psi}{\partial \varphi^2} = \frac{\partial}{\partial \varphi} \left\{ \frac{\left(1 - \frac{\rho_{sol\_PCM}}{\rho_{liq\_PCM}}\right) \cdot \left(V_{nr} - \frac{1}{r}\frac{\partial s}{\partial \varphi}V_{n\varphi}\right)}{\frac{1}{r} + \frac{1}{r^3}\left(\frac{\partial s}{\partial \varphi}\right)^2} \right\} \tag{5.18}$$

where V_{nr} is the radial component of velocity of the liquid/solid interface; $V_{n\varphi}$ is the angular component of the velocity of the liquid/solid interface; and s is the location of the liquid/solid interface in PCM.

At the PCM/shell interface:

$$-k_{shell}\frac{\partial T_{shell}}{\partial n} = -k_{PCM}\frac{\partial T_{PCM}}{\partial n} \tag{5.19}$$

$$v_r = 0, \; v_\varphi = 0 \tag{5.20}$$

Equation (5.19) denotes the energy balance and equation (5.20) denotes the no-slip condition.

Here k_{shell} is the thermal conductivity of the encapsulation shell; k_{PCM} is the thermal conductivity of PCM; n is the unit normal direction of the PCM/shell interface; T_{shell} is the temperature of the shell; T_{PCM} is the temperature of PCM.

Writing equation (5.20) in terms of the stream function and the vorticity yields:

$$\psi = 0 \; , \frac{\partial \psi}{\partial r} = 0 \tag{5.21}$$

$$-\zeta = \frac{\partial^2 \psi}{\partial r^2} \tag{5.22}$$

At the outer surface of the capsule, the energy balance equation can be described as follow:

$$-k_{shell} \frac{\partial T_{shell}}{\partial n} = h(T_{shell} - T_f) \tag{5.23}$$

where T_f is the temperature of HTF; n is the unit normal direction of the outer surface of the capsule; h is the average heat transfer coefficient around the cylinder in a cross flow arrangement. h is determined by the Nusselt number as expressed in equation (3.6).

Governing equations and the boundary conditions are non-dimensionalized using:

$$\theta = \frac{T - T_o}{T_f - T_o}, R = \frac{r}{R_1}, \tau = \frac{\alpha_{PCM}}{R_2^2} t, Y_R = \frac{R_2}{\alpha_{PCM}} v_r, Y_\varphi = \frac{R_2}{\alpha_{PCM}} v_\varphi, \Psi = \frac{\psi}{\psi_o}, Z = \frac{\zeta}{\zeta_o}$$

where θ is the normalized temperature; T_o is the initial temperature of capsule; R is the dimensionless radius; R_1 is the outer radius of the capsule; R_2 is the inner radius of the shell; τ is the dimensionless time; α_{PCM} is the thermal diffusivity of liquid phase PCM; Y_R is normalized radial velocity; Y_φ is normalized angular velocity; Ψ is normalized stream function; ψ_o is the reference stream function; Z is normalized stream vorticity; ζ_o is the reference vorticity.

The dimensionless form of vorticity transport equations become:

$$R_{12} \cdot \frac{\partial Z}{\partial \tau} + \frac{\psi_o}{R_{12}\alpha_{PCM}R} \frac{\partial \Psi}{\partial \varphi} \cdot \frac{\partial Z}{\partial R} - \frac{\psi_o}{R_{12}\alpha_{PCM}R} \frac{\partial \Psi}{\partial R} \frac{\partial Z}{\partial \varphi}$$

$$= \frac{\nu}{\alpha_{PCM}R_{12}} \left[\frac{\partial^2 Z}{\partial R^2} + \frac{1}{R} \frac{\partial Z}{\partial R} + \frac{1}{R^2} \frac{\partial^2 Z}{\partial \varphi^2} \right] + \frac{R_2}{\rho_R \alpha_{PCM} \zeta_o R} \left[R g_\varphi \cdot \frac{\partial \rho}{\partial R} - g_r \cdot \frac{\partial \rho}{\partial \varphi} \right]$$

$$\tag{5.24}$$

$$\nabla^2 \Psi = -\frac{\zeta_o R_1^2}{\psi_o} Z \tag{5.25}$$

The scaled velocity components can be expressed in terms of the stream functions as follows:

$$Y_R = \frac{\psi_o}{R_{12}\,\alpha_{PCM}\,R}\frac{\partial\Psi}{\partial\varphi} \tag{5.26}$$

$$Y_\varphi = -\frac{\psi_o}{R_{12}\,\alpha_{PCM}}\frac{\partial\Psi}{\partial R} \tag{5.27}$$

The energy equation yields:

$$\rho_R c\left(R_{12}\frac{\partial\theta}{\partial\tau} + Y_R\frac{\partial\theta}{\partial R} + \frac{Y_\varphi}{R}\frac{\partial\theta}{\partial\varphi}\right) = \frac{k}{\alpha_{PCM}R_{12}}\left[\frac{1}{R}\frac{\partial}{\partial R}\left(R\frac{\partial\theta}{\partial R}\right) + \frac{1}{R^2}\frac{\partial^2\theta}{\partial\varphi^2}\right] \tag{5.28}$$

Boundary conditions imposed on the velocity and the temperature fields are as follows:

At the centroid of the solid or liquid PCM:

$$\theta_{centroid} = \frac{1}{N}\sum_i \theta_i \tag{5.29}$$

where $\theta_{centroid}$ is the temperature at the centroid of PCM; θ_i is the temperature around the centroid.

Boundary conditions at the liquid/solid interface become:

$$-k_{liq\_PCM}\frac{\partial\theta_{liq\_PCM}}{\partial n} = -k_{sol\_PCM}\frac{\partial\theta_{sol\_PCM}}{\partial n} + \frac{L\rho_{liq\_PCM}\alpha_{PCM}R_1}{R_2^2(T_f - T_o)}V_N \tag{5.30}$$

$$-Z = \frac{\psi_o}{R_1^2\zeta_o}\left(\frac{\partial^2\Psi}{\partial R^2} + \frac{1}{R^3}\frac{\partial S}{\partial\varphi}\frac{\partial\Psi}{\partial\varphi} + \frac{1}{R^2}\frac{\partial^2\Psi}{\partial\varphi^2}\right) \tag{5.31}$$

$$\frac{\partial^2\Psi}{\partial\varphi^2} = \frac{\alpha_{PCM}R_{12}^2}{\psi_o}\frac{\partial}{\partial\varphi}\left\{\frac{\left(1 - \frac{\rho_{sol\_PCM}}{\rho_{liq\_PCM}}\right)\cdot\left(V_{NR} - \frac{\partial S}{R\partial\varphi}V_{N\varphi}\right)}{\frac{1}{R} + \frac{1}{R^3}\left(\frac{\partial S}{\partial\varphi}\right)^2}\right\} \tag{5.32}$$

where V_N is normalized velocity of liquid/solid interface movement in the direction normal to the interface; V_{NR} is the normalized radial component of liquid/solid interface velocity; $V_{N\varphi}$ is the normalized angular component of liquid/solid interface velocity; and S is the normalized displacement of the liquid/solid interface.

At the PCM/shell interface, the energy balance equation becomes:

$$-k_{shell} \frac{\partial \theta_{shell}}{\partial n} = -k_{PCM} \frac{\partial \theta_{PCM}}{\partial n} \quad (5.33)$$

where θ_{shell} is the normalized temperature of encapsulation shell; θ_{PCM} is the normalized temperature of PCM. The no-slip and no-penetration conditions yield:

$$\Psi = 0 \,, \frac{\partial \Psi}{\partial R} = 0 \quad (5.34)$$

$$-Z = \frac{\psi_o}{R_1^2 \zeta_o} \frac{\partial^2 \Psi}{\partial R^2} \quad (5.35)$$

The boundary condition at the outer surface of the capsule becomes:

$$-k_{shell} \frac{\partial \theta_{shell}}{\partial n} = h(\theta_{shell} - 1) \quad (5.36)$$

Jacobi iteration method is applied to solve the energy equation and the vorticity transport equations. Coupled equations (5.24), (5.25) and (5.28) with boundary conditions (5.29)-(5.36) are solved simultaneously at every time steps to determine the temperature and velocity fields and the location of the interface.

5.1.2 Results and Discussion

Two types of HTFs are considered in the simulations, air and liquid Therminol/VP-1. 101 nodes in angular direction and 106 nodes in radial direction are used with the dimensionless time step of 0.00001. The normalized melting temperature of $NaNO_3$ is 0.232.

Figure 5.1 displays the location of propagating liquid/solid interface at various times for 76.2 mm diameter $NaNO_3$ EPCM capsule with air as HTF during a melting process. The buoyancy-driven convection is considered in the molten $NaNO_3$. The natural convection impacts the interface dynamics. The total melting time is approximately 76.1 minutes which is slightly shorter than that when the natural convection is neglected. Since the average Rayleigh number in the molten $NaNO_3$ during melting process is in the magnitude of 10^7 for 76.2 mm diameter $NaNO_3$-stainless steel EPCM capsule ($Ra < 10^9$, smaller than the critical Ra), the effect of natural convection on the storage time is likely to be weak. Nevertheless, the convection in molten PCM still affects the dynamics of the liquid/solid interface. The solid phase of PCM always sinks to the bottom of the capsule since the density of solid state PCM is higher than that of liquid state PCM, as displayed in Figure 5.1. The liquid/solid interface first forms at the PCM/shell interface as the temperature exceeds the melting temperature of $NaNO_3$. The sharp interface separating liquid salt from solid salt propagates inwards.
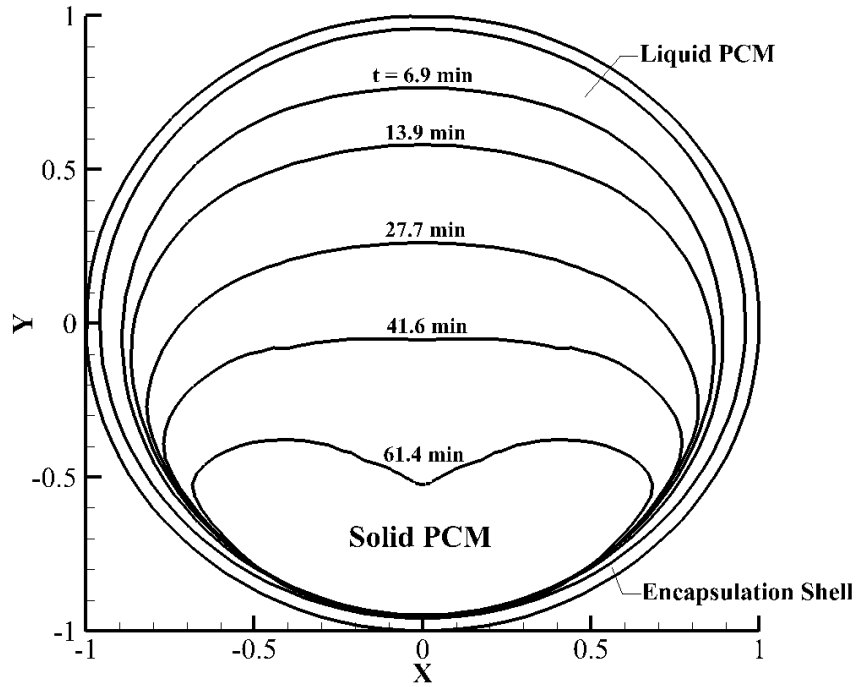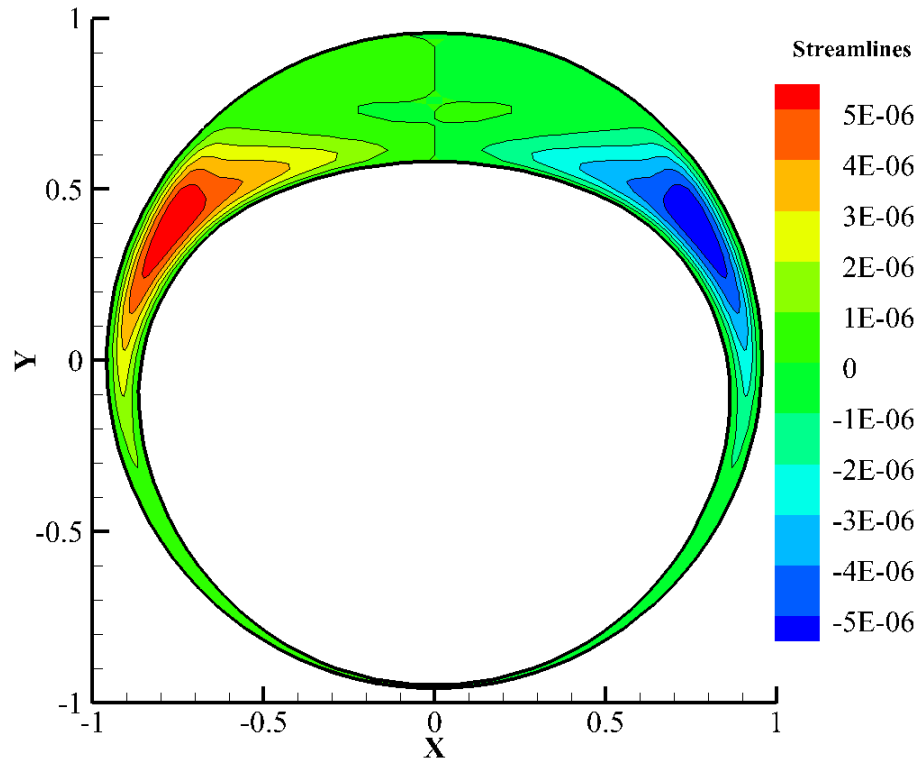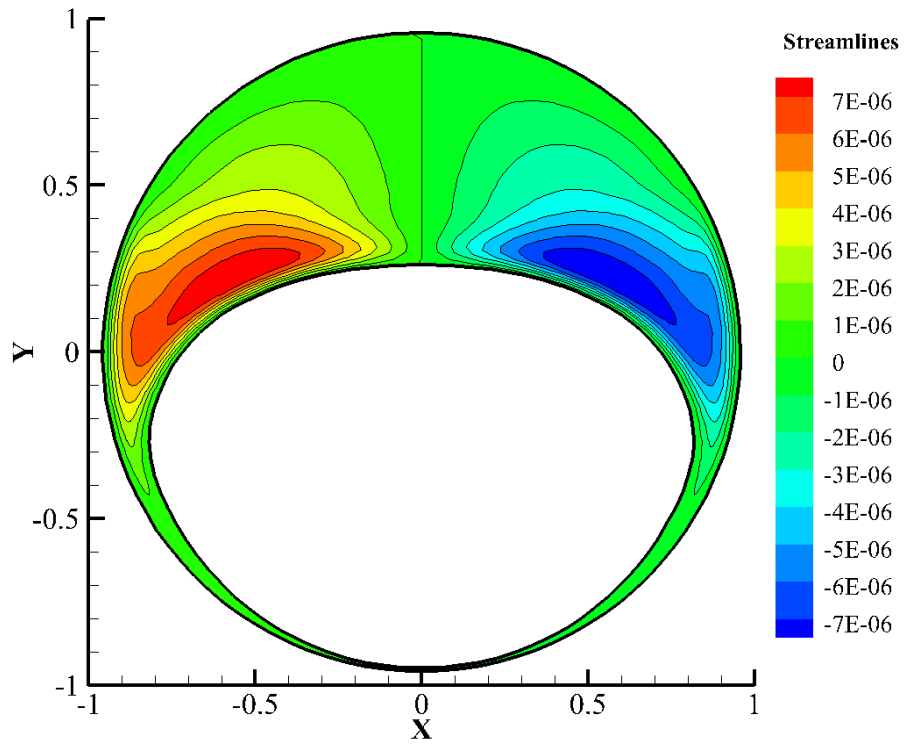
Figure 5.1. Liquid/solid interface movement during melting process using air as HTF
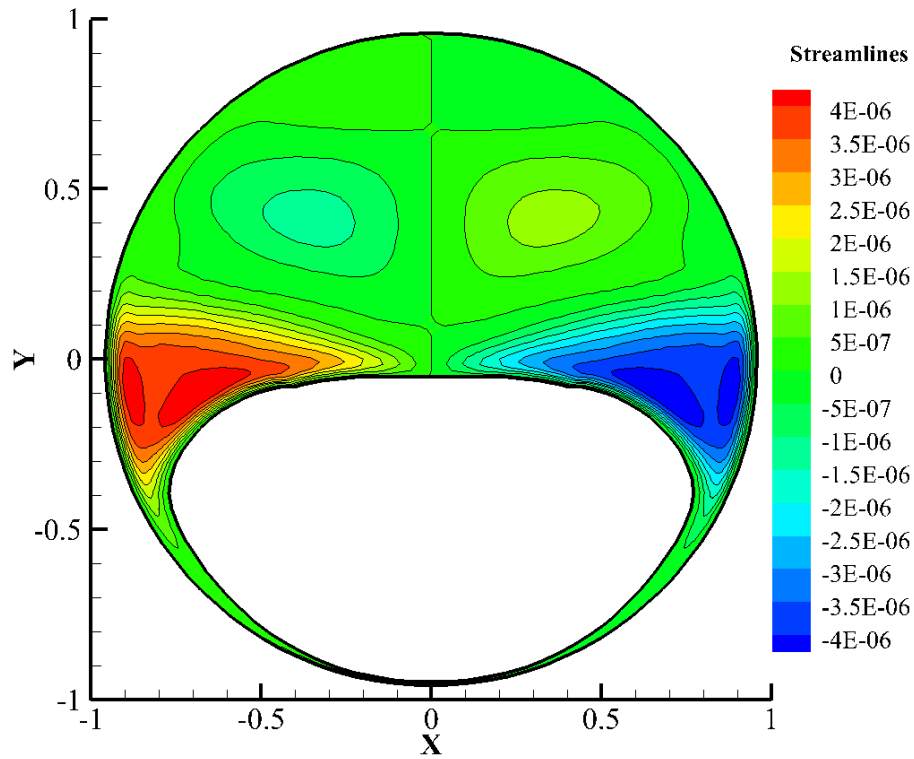
Figure 5.2 represents the streamlines in molten $NaNO_3$ during a melting process with air as HTF at various times. As melting process progresses, the temperature difference in liquid phase PCM increases, which increases the buoyancy-driven convection in the molten PCM, as shown in Figure 5.2. A pair of two counter rotating vortices is seen at the top region of molten salt at early stage of melting as illustrated in Figures 5.2(a) and 5.2(b). The convection intensifies as the melting progresses and another pair of vortices is formed, as seen in Figure 5.2(c). A pair of vortices remains close to the interface and a weaker pair of vortices is formed in the top region of molten PCM.

(a) At 13.9 minutes ($\tau = 0.1$)

(b) At 27.7 minutes ($\tau = 0.2$)

(c) At 41.6 minutes ($\tau = 0.3$)

Figure 5.2. Streamlines in molten NaNO$_3$ during melting process with air as HTF

Figure 5.3 depicts normalized isotherms in NaNO$_3$ capsule at various times during a melting process using air as HTF. The yellow curve indicates the liquid/solid interface in PCM. It is the solid phase PCM inside the yellow curve and it is the liquid phase PCM outside the yellow curve. Temperature in liquid phase PCM rises rapidly to HTF temperature while temperature in solid part remains slightly below melting temperature of NaNO$_3$ during a charging process. Buoyancy-driven convection clearly affects the temperature profiles in EPCM capsule. The melting is faster at the top area due to enhanced heat transfer by the convection.
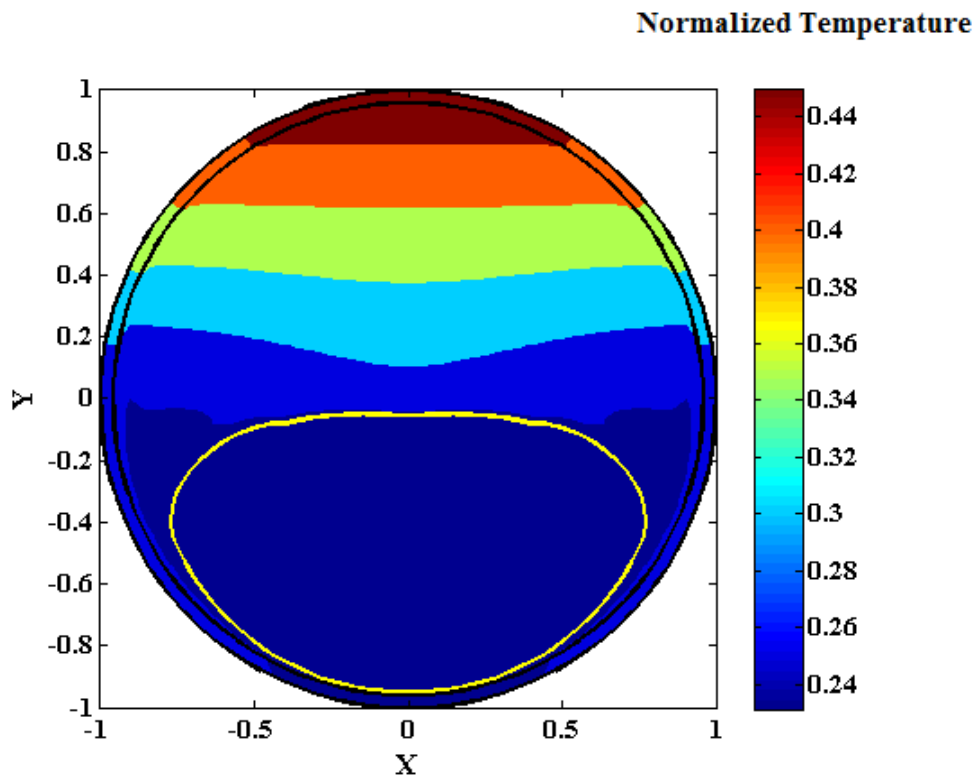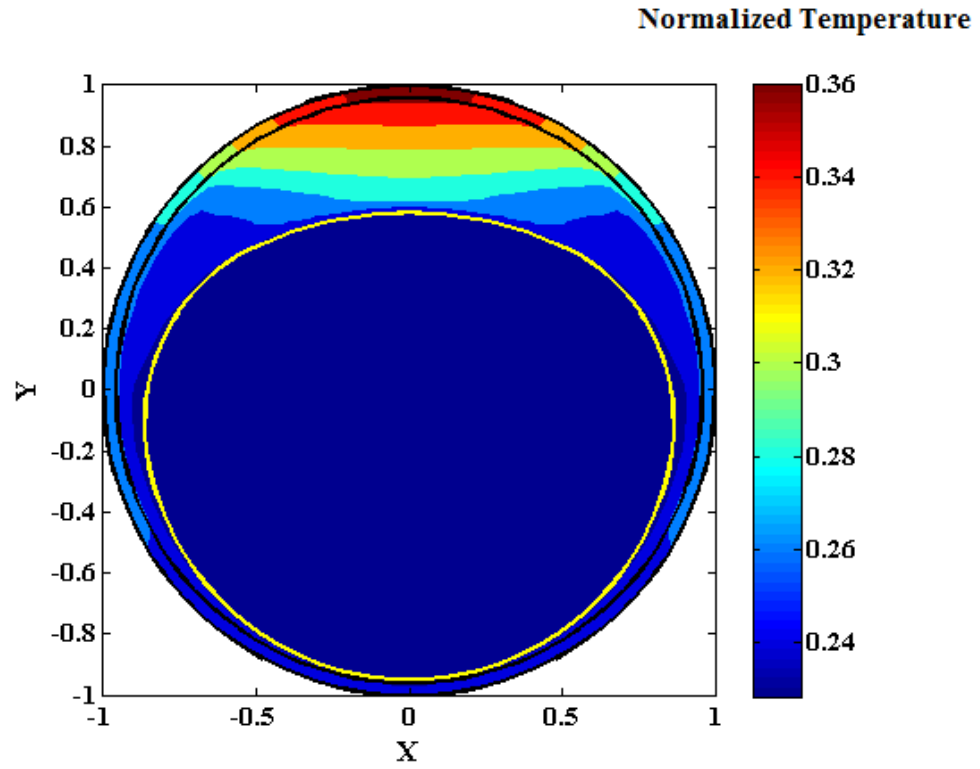
(a) At 13.9 minutes ($\tau = 0.1$)

(b) At 41.6 minutes ($\tau = 0.3$)

Figure 5.3. Temperature profiles in NaNO₃ EPCM capsule during melting process with air as HTF

Figure 5.4 shows the location of the liquid/solid interface in 76.2 mm diameter NaNO$_3$ EPCM capsule during a melting process with liquid Therminol/VP-1 as HTF. Because of the higher density and the higher heat capacity of liquid HTF, the melting is much faster compared to that using air as HTF. The liquid/solid interface in PCM is formed near PCM/shell interface and moves inwards. Due to the gravity effect, the solid state PCM sinks at the bottom of the capsule.
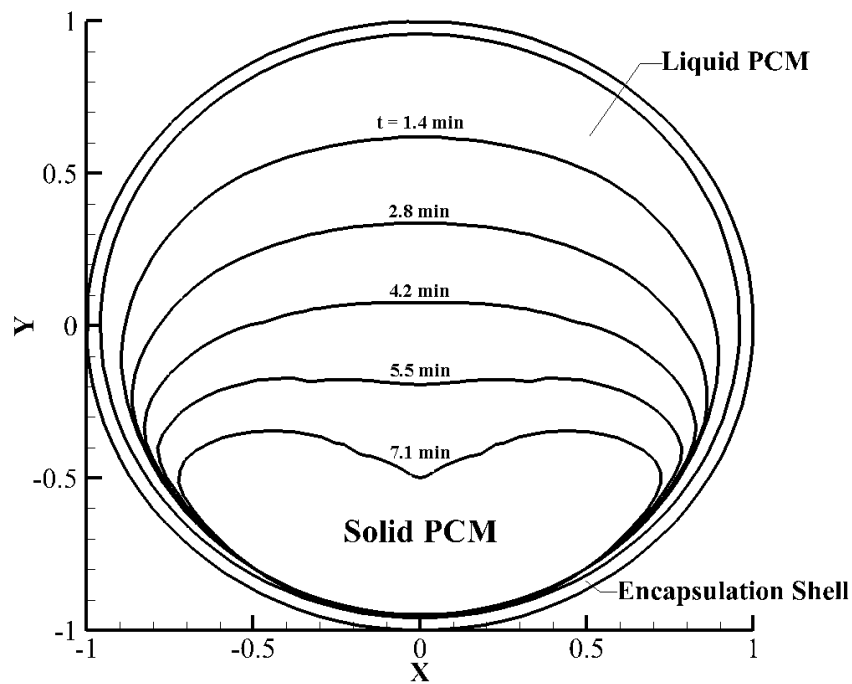

Figure 5.4. Liquid/solid interface movement during melting process using liquid Therminol/VP-1 as HTF

Figure 5.5 is the streamlines in the molten PCM at various times using liquid Therminol/VP-1 as HTF. The buoyancy-driven convection is more intense when liquid Therminol/VP-1 is HTF compared to that when air is HTF. Figure 5.6 illustrates the temperature profiles in NaNO$_3$ capsule at various times using liquid as HTF. The convection in the molten NaNO$_3$ affects the temperature distributions inside the capsule.

The larger convection at the top would increase the melting rate at the top region of the solid PCM. High temperature gradient is present in the liquid PCM while the temperature always remains slightly below the melting temperature of PCM in the solid state.
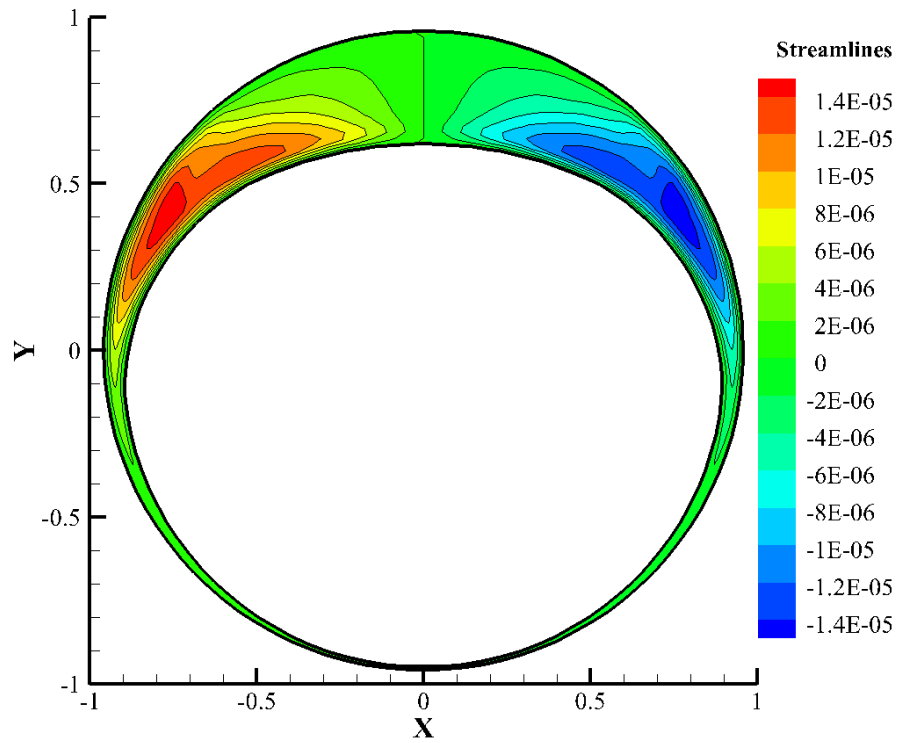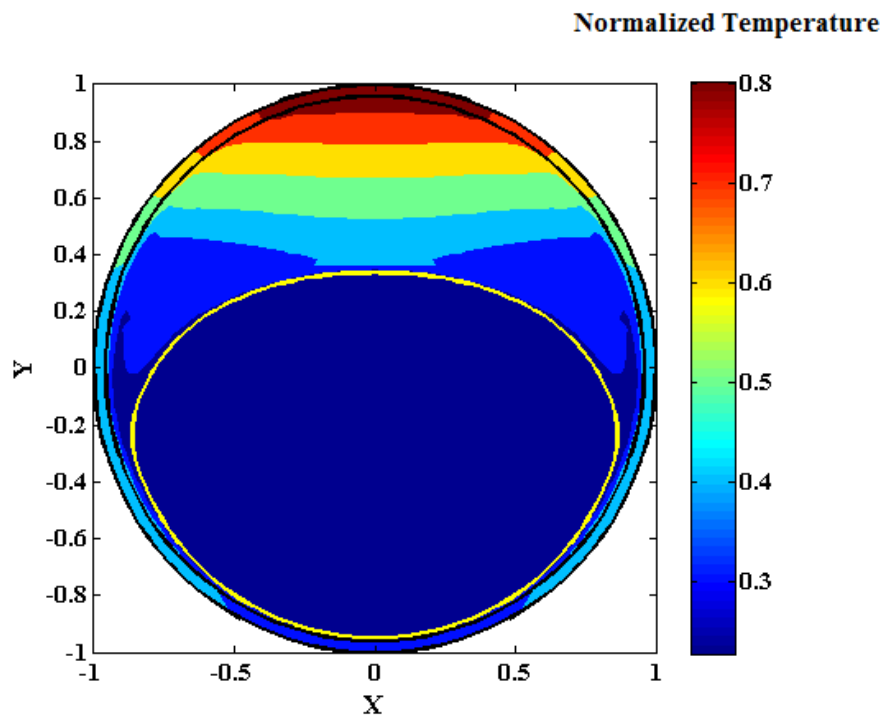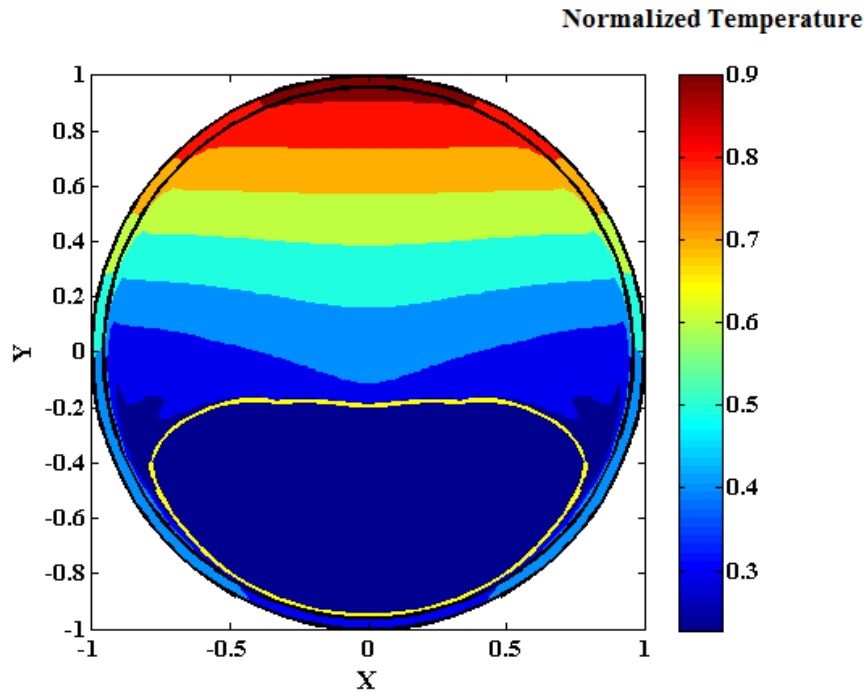

(a) At 1.4 minutes ($\tau = 0.01$)
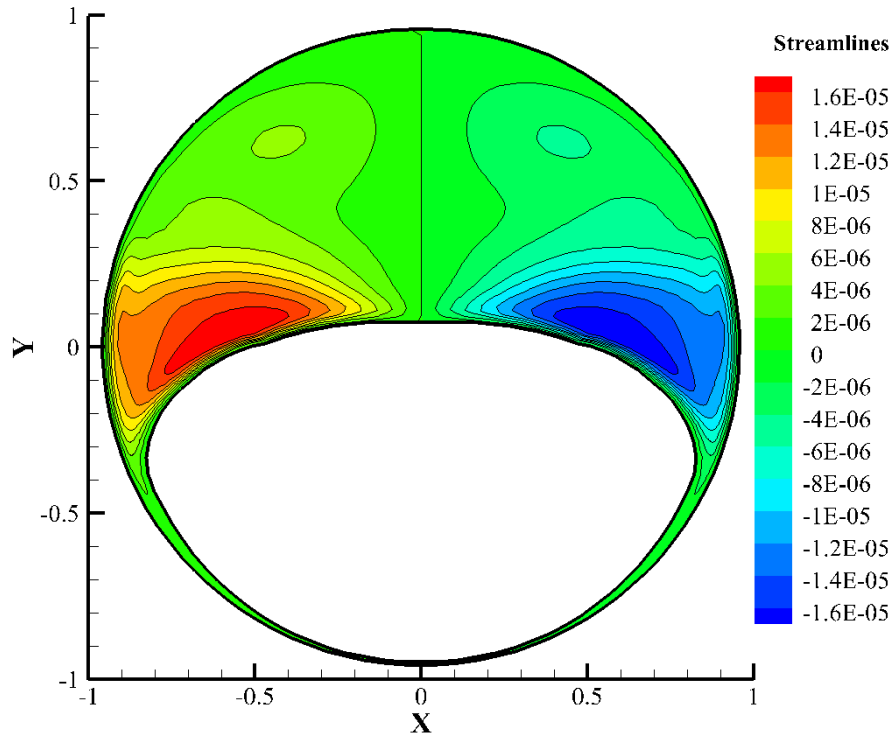
(b) At 4.2 minutes ($\tau = 0.03$)

Figure 5.5. Streamlines in molten NaNO$_3$ during melting process with liquid Therminol/VP-1 as HTF

(a) At 2.8 minutes ($\tau = 0.02$)

(b) At 5.5 minutes ($\tau = 0.04$)

Figure 5.6. Temperature profiles in NaNO$_3$ EPCM capsule during melting process with liquid Therminol/VP-1 as HTF

Table 5.1 illustrates the melting times for NaNO$_3$ capsule with different HTFs. It compares the melting times with buoyancy-driven convection in the molten PCM to those without the natural convection in PCM. Since the average Rayleigh number in the current case is lower than the critical Rayleigh number as described previously, the natural convection inside liquid PCM creates slow laminar flow. Hence, it slightly shortens the energy storage times. Moreover, using liquid as HTF would increase the energy storage rate compared to that using air as HTF. The temperature difference in the molten PCM is higher and that would enhance the natural convection in the liquid PCM. Thus, the energy storage and retrieval times are expected to be much shorter when liquid HTF is used.

Table 5.1. Melting times for 76.2 mm diameter NaNO$_3$ EPCM capsule with different types of HTFs.

	Air	Liquid Therminol/VP-1
Buoyancy-driven convection in molten PCM + Gravity effect of solid PCM	76.1 min	9.1 min
No buoyancy-driven convection in molten PCM (considering gravity effect of solid PCM)	79.4 min	14.9 min

5.2 The Effect of Void

Figure 5.7 is the schematic of the EPCM cylinder in a cross flow arrangement considering the 20% void space at the top of the capsule. The local Nusselt number around the capsule varies in the angular direction as described in Figure 4.2 in Chapter 4. Based on the volume expansion of NaNO$_3$ due to phase change [16], 20% of the capsule is kept as a void. The void space is occupied by the air. The buoyancy-driven convection in the molten PCM is neglected for these simulations.
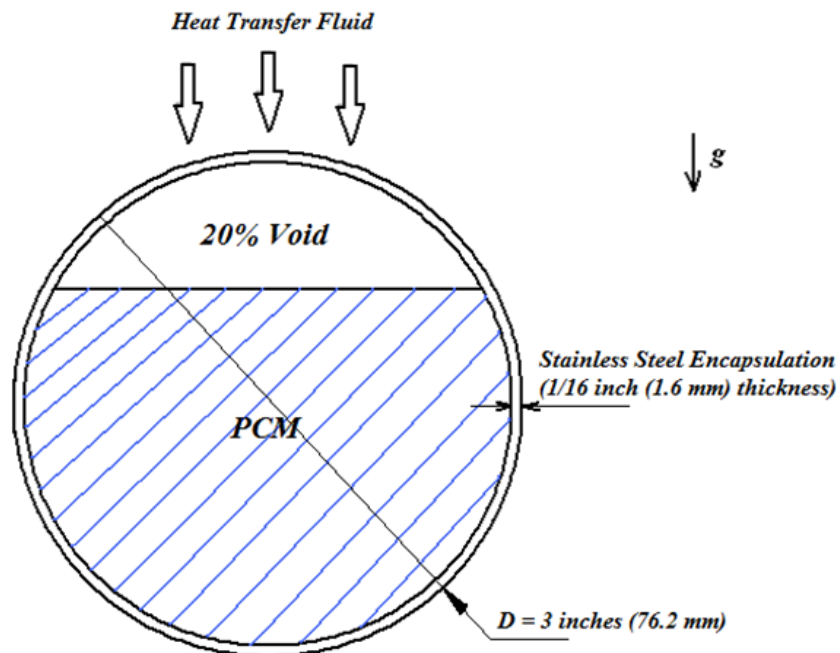

Figure 5.7. Schematic of the EPCM capsule geometry with void space

The energy balance at shell/void interface and at the void/PCM interface should be added to the governing equation and boundary conditions described in the Chapter 4. The thermal boundary condition at the shell/void interface is:

$$-k_{shell}\frac{\partial T_{shell}}{\partial n} = -k_{void\_air}\frac{\partial T_{void\_air}}{\partial n} \qquad (5.37)$$

At the void/PCM interface:

$$-k_{void\_air}\frac{\partial T_{void\_air}}{\partial n} = -k_{PCM}\frac{\partial T_{PCM}}{\partial n} \qquad (5.38)$$

where k_{void_air} is thermal conductivity of air in the void; T_{void_air} is temperature of air.

Figure 5.8 illustrates the temperature distribution in 76.2 mm diameter $NaNO_3$ EPCM capsule before melting process starts. It is at 3.3 minutes from the beginning of a charging process. The white horizontal line inside the capsule, as shown in Figure 5.8, is the original location of the interface between void space and PCM. Since the highest heat transfer coefficient occurs at the front stagnation point, the temperature at the top area of EPCM increases faster.
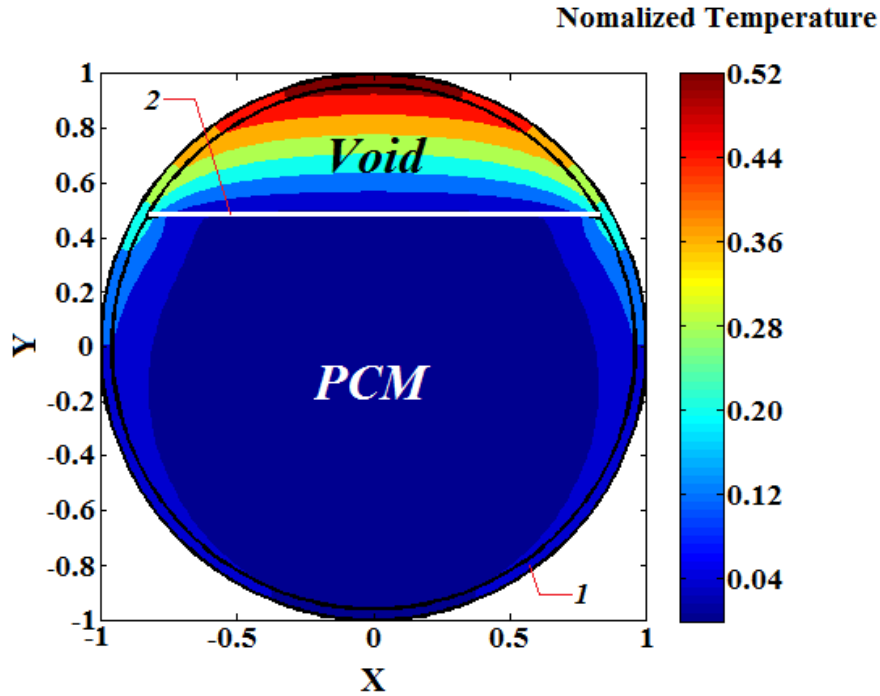
1- Encapsulation shell
2- Location of void/PCM interface

**Figure 5.8. Temperature profile in NaNO$_3$ EPCM before melting process at 3.3 minutes (τ = 0.024) into the charging process (air is used as HTF)**

Figure 5.9 displays the location of the liquid/solid interface and temperature distributions in NaNO$_3$ EPCM capsule at various times during the melting process. Figure 5.9(a) represents the temperature profile at 16.7 minutes into the melting process. The red curve inside the capsule is the liquid/solid interface in PCM while the red horizontal line is the location of the void/PCM interface. Region inside the red curve is solid state PCM and region outside the red curve is liquid state PCM. The horizontal black dash line inside the capsule represents the original location of void/PCM interface. At the early stage of the melting process, the solid PCM starts melting at the corner (shell/PCM/void) area. As the melting progresses, the liquid/solid interface moves down to the bottom of the capsule along the shell/PCM interface. Meanwhile, the void/PCM interface moves up because of the volume expansion of molten PCM. It is assumed that the void/PCM interface remains

flat by neglecting the effects of surface tension. 33.2 minutes into the melting, a closed interface is formed in PCM, as shown in Figure 5.9(b). As melting progresses further, the interface propagates radially inwards while the void/PCM interface moves up further since more PCM melts. 89 minutes into the melting process, nearly entire PCM turns into the liquid phase, as displayed in Figure 5.9(d). The heat transfer inside the EPCM is slightly slower as the air filling the void space is serving as an insulator.

1- Encapsulation shell
2- Liquid PCM
3- Location of void/PCM interface
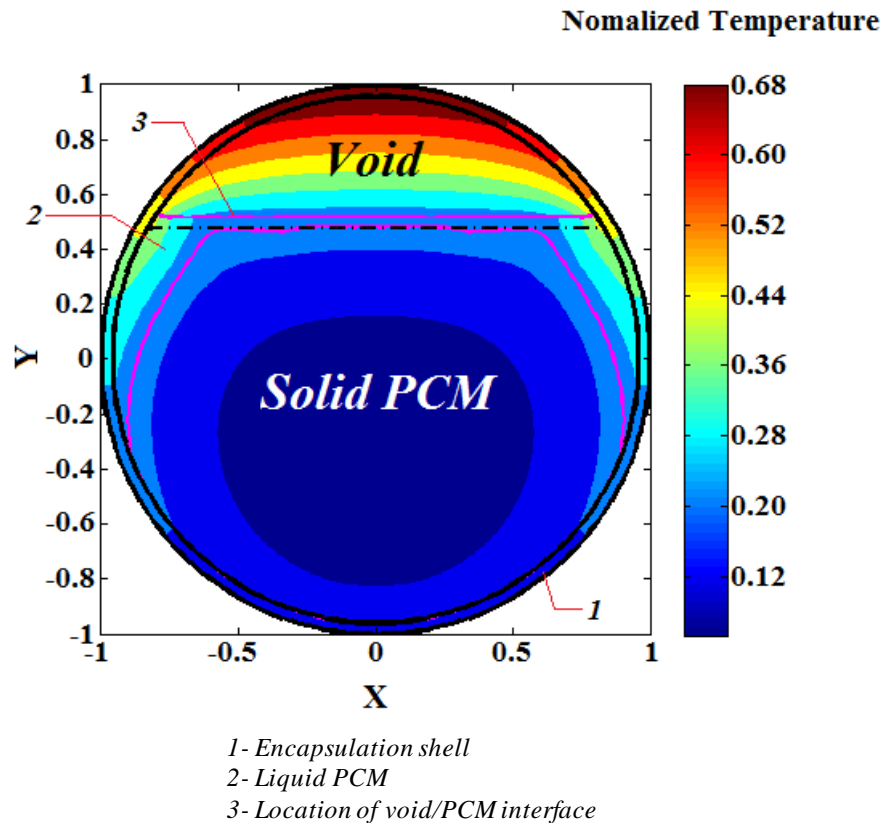
(a) Location of the interface and the temperature distribution in EPCM 16.7 minutes into the melting process

1- Encapsulation shell
2- Liquid PCM
3- Location of void/PCM interface
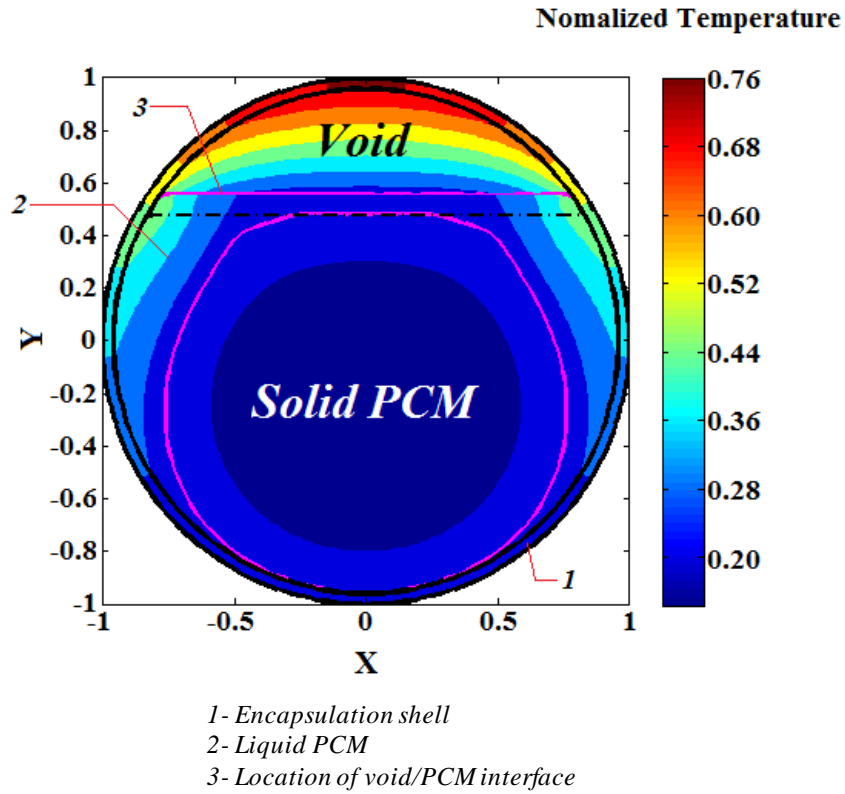
(b) Location of the interface and the temperature distribution in EPCM 33.2 minutes into the melting process

1- Encapsulation shell
2- Location of void/PCM interface
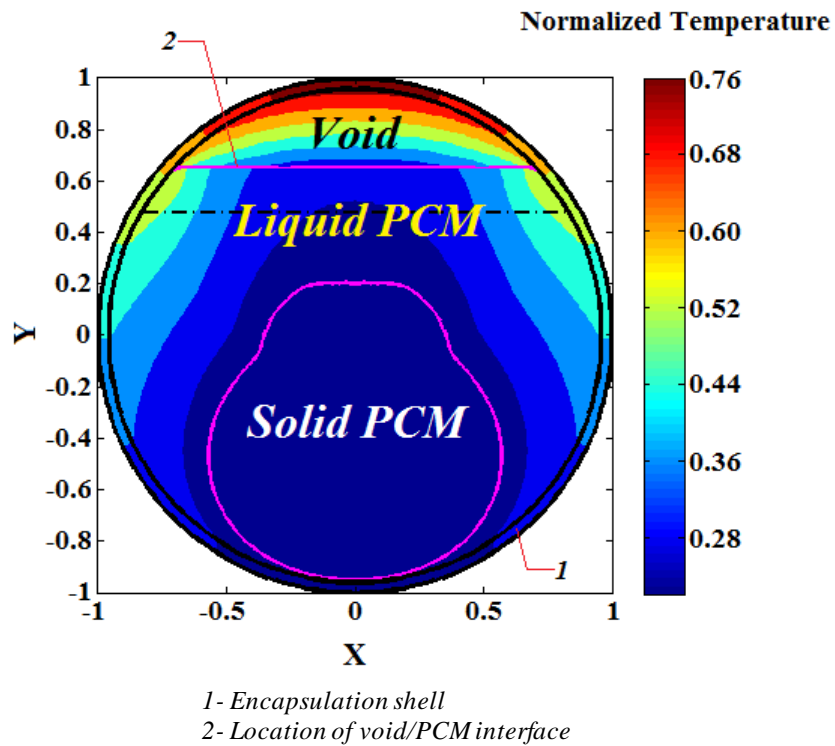
(c) Location of the interface and the temperature distribution in EPCM 61.1 minutes into the melting process

93

Normalized Temperature

1- *Encapsulation shell*
2- *Solid PCM*
3- *Location of void/PCM interface*

(d) Location of the interface and the temperature distribution in EPCM 88.9 minutes into the melting process
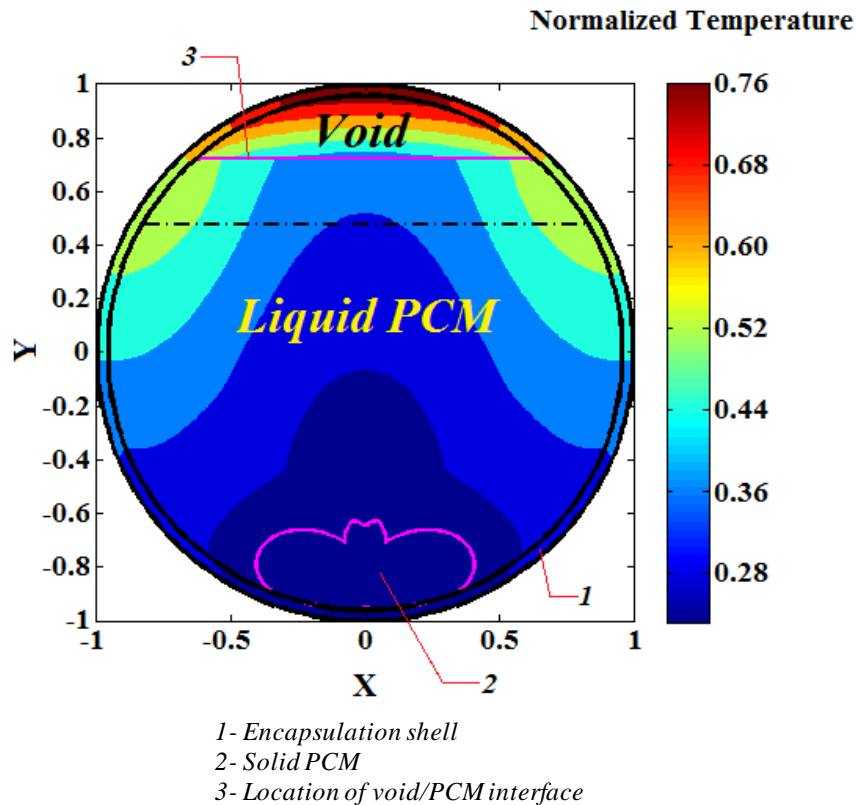
Figure 5.9. Location of the interface and the isotherms in NaNO₃ EPCM (air is served as HTF)

5.3 Conclusions

The buoyancy-driven convection in the molten PCM influences the dynamics of the liquid/solid interface and the temperature profiles in the capsule. It shortens the energy storage time slightly. The energy storage time in the thermal management system considered here is not influenced greatly by the buoyancy-driven convection since the flow in the melt resulted from natural convection is very slow. The void space inside the capsule designed to compensate the volume expansion by the phase change in the PCM, which influences the energy storage time in the capsule.

Table 5.2 summarizes the melting times for NaNO$_3$ EPCM capsule for various conditions. The natural convection in molten PCM slightly improves the heat transfer process inside the capsule. Rayleigh number, $Ra = g\beta\Delta T R_d^3/(\alpha_{PCM}\upsilon)$, indicates the magnitude of the buoyancy and viscous forces in the fluid. The larger the Rayleigh number, the stronger the natural convection becomes. When the liquid is used as HTF, the Rayleigh number can be slightly higher due to higher temperature difference in the melt flow, which might enhance heat transfer in the capsule. The void space slows down the heat transfer process inside the capsule slightly, as indicated by Table 5.2. The melting time for the void space inside the capsule case in Table 5.2 is simulated using average convective heat transfer coefficient around the capsule determined by the Nusselt number expressed in equation (3.6).

Table 5.2. Melting times for 76.2 mm diameter NaNO$_3$ EPCM capsule with air as HTF.

	Melting Times (Minutes)
Gravity effect of solid PCM	79.4
Buoyancy-driven convection in molten PCM + Gravity effect of solid PCM	76.1
20% void space in capsule + Gravity effect of solid PCM	65.6

CHAPTER 6
CONCLUSIONS

The present work includes immersion calorimeter experiments and heat transfer simulations for EPCM capsules for thermal energy storage system. The aim has been to study single EPCM for their usage in TES systems.

Based on immersion calorimetry experimental development and investigation, it is concluded that:

1. Based on immersion calorimeter measurements, salt based EPCMs are shown to be capable of being used as PCM for TES. There was no measurable deterioration of storage capability in salt PCM based EPCM capsules after multiple thermal cycles nor after long-term exposure at high temperatures. Nevertheless, corrosion tests are needed for salt based EPCM capsules before applying them to CSP plants.

2. Metal phase change materials, such as zinc and aluminum, encapsulated by other metal materials (such as stainless steel, nickel, etc.) are not quite suitable to for TES based on the calorimeter tests; this may be due to undesired intermetallic compound formed between PCM and encapsulation shell. One way to avoid this problem is to use less reactive materials as encapsulation shell, such as ceramic, quartz, etc., but further studies are needed.

Heat transfer simulations were conducted for EPCM capsules. Various heat transfer and material combination for EPCM were compared, as illustrated in Table 6.1, to better

appreciate the heat transfer processes inside the capsule to help design EPCM based thermoclines. The conclusions from the heat transfer analysis are summarized as follows:

1. Larger sizes of capsules would have longer heat transfer times.

2. The heat transfer process is significantly improved by using liquid as HTF instead of a gas because of higher density and heat capacity of liquids.

3. Larger temperature differences between HTF and EPCM would increase the energy storage/retrieval rate in the capsule during phase change process.

4. During energy storage and melting of the PCM, the effect gravity and the higher density of solid PCM in the EPCM capsule would shorten energy storage times.

5. Buoyancy-driven convection in molten PCM could impact the liquid/solid interface movement in PCM, the temperature profiles in the EPCM capsule, and shorten the energy storage times. However, for the conditions considered here, the average Rayleigh number is relatively small and thus the convection effects are likely to be not significant.

6. Using liquid as HTF could slightly enhance the natural convection in molten PCM compared to when air is used as HTF.

7. There must be sufficient void space inside the EPCM capsule for volumetric expansion of PCM due to phase change and temperature increases. The void space could act as an insulator and could slightly slow down the heat transfer rate inside the capsule (comparing the melting times per unit mass of PCM between considering the void space in the capsule case and no void space case).

Table 6.1. Melting times for 76.2 mm diameter NaNO$_3$ EPCM capsule with air as HTF.

	Melting Times (Minutes)	Melting times per unit mass of PCM (Minutes/kg)
No gravity effect of solid PCM; No natural convection in molten PCM; No void space in capsule	114.8	12.1
Gravity effect of solid PCM	79.4	8.4
Buoyancy-driven convection in Molten PCM + Gravity effect of solid PCM	76.1	8.0
20% void space in capsule + Gravity effect of solid PCM	65.6	8.6

Studies of the heat transfer performance in EPCM capsule conducted here can help to improve the understanding of TES process and the total energy storage/retrieval times with EPCMs and help with thermocline design.

REFERENCES

1. Annual Energy Outlook 2012, Early Release Reference Case, U.S. Energy Information Administration, January 23, 2012, Washington, DC.

2. Survey of thermal storage for parabolic trough power plants, Pilkington Solar International GmbH, Cologne, Germany, National Renewable Energy Laboratory, NREL/SR-550-27925, September 2000.

3. H. Michels, R. Pitz-Paal, Cascaded latent heat storage for parabolic trough solar power plants, Solar Energy 81 (2007) 829–837.

4. M. Kenisarin, K. Mahkamov, Solar energy storage using phase change materials, Renewable and Sustainable Energy Reviews 11 (2007) 1913-1965.

5. M.M. Farid, A.M. Khudhair, S.A.K. Razack, S. Al-Hallaj, A review on phase change energy storage: materials and applications, Energy Conversion and Management 45 (2004) 1597-1615.

6. A. Abhat, Low temperature latent heat thermal energy storage: heat storage materials, Solar Energy 30 (1983) 313-332.

7. H. Mehling, L.F. Cabeza, Phase change materials and their basic properties, Thermal Energy Storage for Sustainable Energy Consumption (2007) 257-277.

8. T. Wada, R. Yamamoto, Studies on salt hydrate for latent heat storage. I. crystal nucleation of sodium acetate trihydrate catalyzed by tetrasodium pyrophosphate decahydrate, The Chemical Society of Japan 55 (1982) 3603-3606.

9. J. Li, G. Zhang, J. Wang, Investigation of a eutectic mixture of sodium acetate trihydrate and urea as latent heat storage, Solar Energy 47 (1991) 443-445.

10. R. Naumann, H.H. Emons, Results of thermal analysis for investigation of salt hydrates as latent heat-storage materials, Journal of Thermal Analysis 35 (1989) 1009-1031.

11. G.A. Lane, Solar heat storage: latent heat material, In: Background and Scientific Principles, vol. I, CRC Press, Florida, 1983.

12. G.A. Lane, Solar heat storage: latent heat material, In: Technology, vol. II, CRC Press, Florida, 1986.

13. B. Zalba, J.M. Marin, L.F. Cabeza, H. Mehling, Review on thermal energy storage with phase change: materials, heat transfer analysis and applications, Applied Thermal Engineering 23 (2003) 251-283.

14. T. Bauer, D. Laing, R. Tamme, Characterization of sodium nitrate as phase change material, International Journal of Thermophysics 33 (2012) 91-104.

15. D. Heine, F. Heess, D. Steiner, Untersuchung von mittel- und hochtemperatur-latentwärmespeicher-materialien. Bundesministerium fuer Forschung und Technologie, Bonn (Germany, F.R.), 1981, 110 pages.

16. G.J. Janz, C.B. Allen, N.P. Bansal, R.M. Murphy, R.P.T. Tomkins, Physical properties data compilations relevant to energy storage. II. molten salts: data on single and multi-component salt systems, U.S. Department of Commerce, National Bureau of Standards, 1979, Washington, D.C.

17. T. Jriri, J. Rogez, C. Bergman, J.C. Mathieu, Thermodynamic study of the condensed phases of $NaNO_3$, KNO_3 and $CsNO_3$ and their transitions, Thermochimica Acta 266 (1995) 147-161.

18. Y. Takahashi, R. Sakamoto, M. Kamimoto, Heat capacities and latent heats of $LiNO_3$, $NaNO_3$, and KNO_3. International Journal of Thermophysics 9 (1988) 1081-1090.

19. F.P. Incropera, D.P. DeWitt, Fundamentals of Heat and Mass Transfer, fifth ed., John Wiley & Sons, Inc., New York, 2002.

20. J.H. Awbery, E. Griffiths, The latent heat of fusion of some metals, Proceedings of the Physical Society of London 38 (1925) 378-398.

21. F. Grønvold, S. Stølen, Heat capacity of solid zinc from 298.15 to 692.68 K and of liquid zinc from 692.68 to 940 K: thermodynamic function values, Thermochimica Acta 395 (2003) 127-131.

22. http://www.crct.polymtl.ca/fact/documentation/FTsalt/FTsalt_Figs.htm

23. R.A. McDonald, Enthalpy, heat capacity, and heat of fusion of aluminum from 366 to 1647 K, Journal of Chemical and Engineering Data 12 (1967) 115-118.

24. Johnson C.H. Chen et al., Encapsulated Phase Change Thermal Energy Storage Materials, United States Patent, 1985.

25. D.P. Colvin, Enhanced thermal management using encapsulated phase change materials an overview, Advances in Heat and Mass Transfer in Biotechnology, HTD-Vol. 363, BED-Vol. 44, (1999) 199-206.

26. E. Gunther, H. Mehling, S. Hiebler, Modeling of subcooling and solidification of phase change materials, Modelling Simul. Mater. Sci. Eng. 15 (2007) 879-892.

27. J.J. Blaney, S. Neti, W.M. Misiolek, A. Oztekin, Stresses in containment capsule for encapsulated phase change materials, Applied Thermal Engineering (2012) (in print).

28. J.J. Blaney, Stresses in Containment Vessels for Encapsulated Phase Change Materials, Thesis, Mechanical Engineering and Mechanics Department, Lehigh University, 2010.

29. C.Y. Li, S.V. Garimella, J.E. Simpson, Fixed-grid front-tracking algorithm for solidification problems, part I: method and validation, Numerical Heat Transfer, Part B: Fundamentals 43 (2) (2003) 117–141.

30. C.Y. Li, S.V. Garimella, J.E. Simpson, Fixed-grid front-tracking algorithm for solidification problems, part II: directional solidification with melt convection, Numerical Heat Transfer, Part B: Fundamentals 43 (2) (2003) 143–166.

31. S.H. Davis, Hydrodynamic interactions in directional solidification, J. Fluid Mech. 212 (1990) 241-262.

32. S.R. Coriell, G.B. McFadden, R.F. Sekerka, Cellular growth during directional solidification, Ann. Rev. Mater. Sci. 15 (1985) 119-145.

33. M.E. Glicksman, S.R. Coriell, G.B. McFadden, Interaction of flows with the crystal-melt interface, Ann. Rev. Fluid Mech. 18 (1986) 307-335.

34. S.R. Coriell, G.B. McFadden, R.F. Boisvert, M.E. Glicksman, Q.T. Fang, Coupled convective instabilities at crystal-melt interfaces, Journal of Crystal Growth 66 (3) (1984) 514-524.

35. B.T. Murray, S.R. Coriell, G.B. McFadden, A.A. Wheeler, B.V. Saunders, Gravitational modulation of thermosolutal convection during directional solidification, Journal of Crystal Growth 129 (1) (1993) 70-80.

36. Q.T. Fang, M.E. Glicksman, S.R. Coriell, G.B. McFadden, R.F. Boisvert, Convective influence on the stability of a cylindrical solid-liquid interface, J. Fluid Mech. 151 (1985) 121-140.

37. Y. Zheng, W. Zhao, J.C. Sabol, K. Tuzla, S. Neti, A. Oztekin, J.C. Chen, Encapsulated phase change materials for energy storage – characterization by calorimetry, Solar Energy (2012) (accepted for publication).

38. S. Neti, Novel Thermal Storage Technologies for Concentrating Solar Power Generation, Lehigh University, CSP Program Award Review Meeting, U.S. DOE Award DE-FC36-08GO18150, 2011.

39. G.J. Janz, Thermodynamic and transport properties for molten salts: correlation equations for critically evaluated density, surface tension, electrical conductance, and

viscosity data, Journal of Physical and Chemical Reference Data 17 (suppl. 2) (1988) pp. 70, 79.

40. D.F. Williams, Additional physical property measurements and assessment of salt compositions proposed for the intermediate heat transfer loop, ORNL/GEN4/LTR-06-033.

41. D.F. Williams, Assessment of candidate molten salt coolants for the NGNP/NHI heat-transfer Loop, Nuclear Science and Technology Division, Oak Ridge National Laboratory, Oak Ridge, Tennessee, ORNL/TM-2006/69, 2006.

42. Therminol VP-1, Dowtherm A, Heat Transfer Fluids by SOLUTIA.

43. W. Zhao, A.F. Elmozughi, A. Oztekin, S. Neti, Heat transfer simulations for encapsulated phase change material for thermal energy storage, International Journal of Heat and Mass Transfer (submitted to the publication).

44. M. Ashjaee, S. Amiri, K. Habibi, Slot jet impingement heat transfer from an isothermal circular cylinder, Thermal Issues in Emerging Technologies, ThETA 2, Cairo, Egypt (2008) 399-404.

45. E. Buyruk, Heat transfer and flow structures around circular cylinders in cross-flow, Turkish Journal of Engineering and Environmental Sciences 23 (1999) 299-315.

46. R.B. Bird, W.E. Stewart, E.N. Lightfoot, Transport Phenomena, first ed., John Wiley & Sons, Inc., New York, 1960.

Vita

Weihuan Zhao was born on January 12, 1985 in Shanghai, China, daughter of Niansi Zhao and Qingxin Ding. After finishing high school in 2003, she entered Shanghai Jiao Tong University and studied in the field of mechanical engineering in China. She completed the Bachelor of Science in Mechanical Engineering in 2007, with a minor in computer engineering. After completing the B.S., she entered Lehigh University in 2007 and completed Master of Science degree in Mechanical Engineering in 2009. She is currently a doctoral candidate at Lehigh University studying the thermal energy storage.